Hydraulic fracture propagation model for porous media

MSc Thesis

Emil Gallyamov

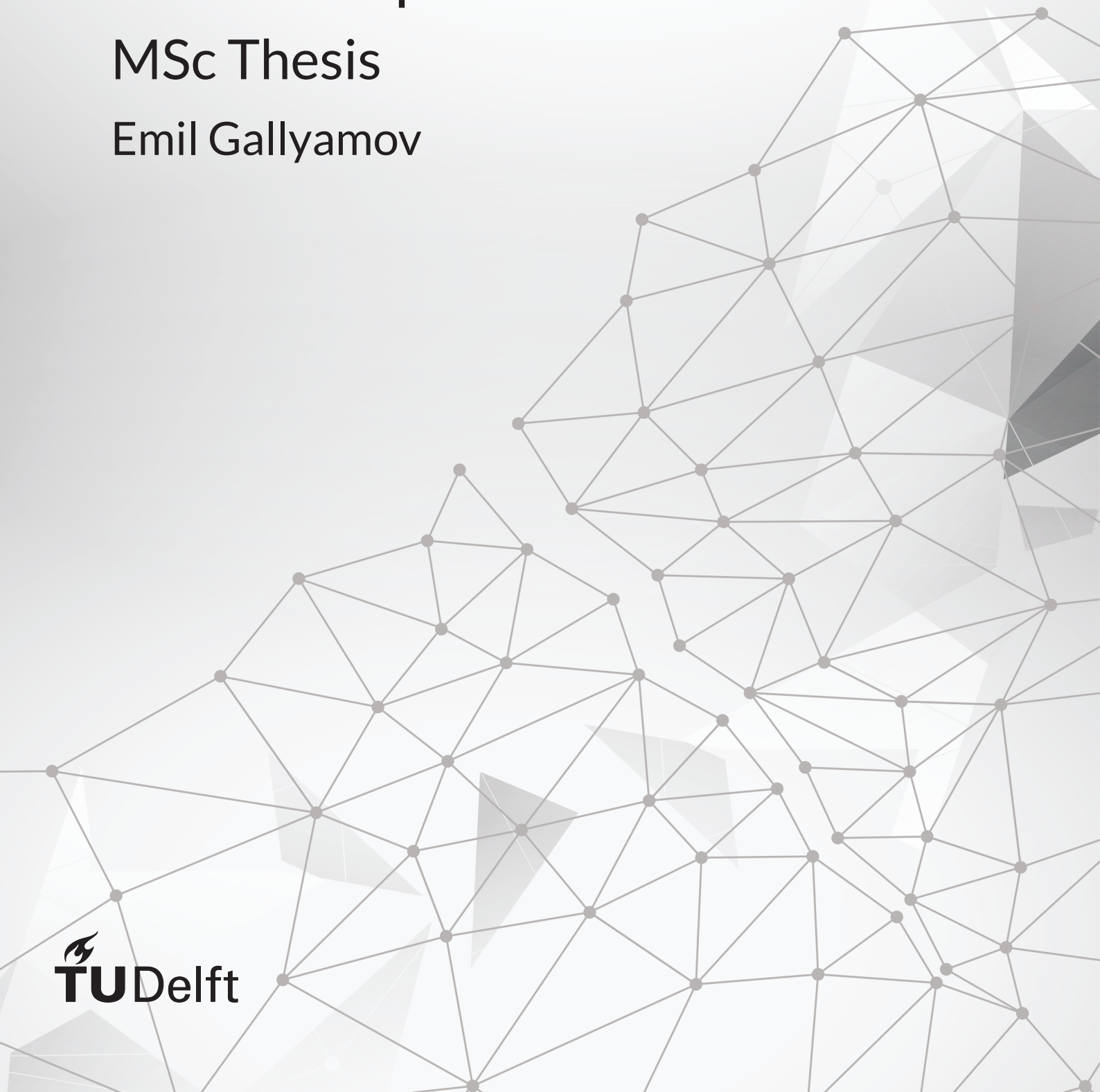

TU Delft

Hydraulic fracture propagation model for porous media

MSc Thesis

by

Emil Gallyamov

in partial fulfillment of the requirements for the degree of

Master of Science
in Civil Engineering,
Geo-Engineering specialization,

at the Delft University of Technology,
to be defended publicly on Tuesday August 29, 2017 at 16:00 PM.

Student number:	4508939	
Project duration:	Novermber, 2016 – August, 2017	
Thesis committee:	Prof. Dr. Ir. L. J. Sluys,	TU Delft, chairman
	Dr. D. Voskov,	TU Delft, supervisor
	Dr. T. Garipov,	Stanford University
	Dr. P. J. Van den Hoek,	TU Delft

TU Delft

Acknowledgments

I would like to express my gratitude to the graduation committee. Thanks to my supervisor, Dr. Denis Voskov for proposing the research topic and providing guidance and support. I am grateful to Dr. Paul van den Hoek for setting up the semi-analytical model and helping with validation of the results. I am also grateful to Dr. Phil Vardon and Prof. Bert Sluys for their constructive comments on my thesis and presentation. A very special gratitude goes to my advisor Dr. Timur Garipov. Thank you for all the work done together, brainstorming and debugging sessions, shared theoretical and practical experience. You managed to nurture a deep interest in the field of fracture mechanics which determined my following step in life.

I would also like to thank my lecturers Dr. Dominique Ngan-Tillard and Prof. Timo Heimovaara for their fascinating classes and interest aroused in the fields of geology and numerical modeling. Additional thanks to Dr. Ngan-Tillard who helped me with all the administrative work.

The financial support of the Xodus Group is gratefully acknowledged. I am also thankful to the Department of Geoscience & Engineering at TU Delft for financing my participation in conferences and providing the workplace. The assistance of Lydia Broekhuijsen, Margot Bosselaar, and Marja Roep-Van der Klis has been invaluable.

Finally, I would like to thank each of my family and friends for your enduring encouragement. Extra credits go to Vadim Gallyamov for designing the cover.

Emil Gallyamov
Delft, August 2017

Abstract

In recent years, humanity became strongly dependent on the deep subsurface. It can be used as the energy source as well as the storage facility. At some stage, both listed applications require injection of fluid or gas into the subsurface porous media. Under certain conditions, it may provoke growth of hydraulic fractures. The appearance of fractures significantly changes properties of the permeable media which, in its turn, affects the operational performance of the subsurface reservoir. Apart from that, hydraulic fracturing may also cause a nuisance to the human environment in the form of earthquakes. Ability to predict growth of hydraulic fractures and their geometry becomes crucial. For this purposes, numerical models are extensively used.

In this work, a fully coupled hydro-mechanical model for hydraulic fracturing of porous media was proposed. Based on this model, an explicit computational framework was developed in C++ programming language allowing efficient modeling of a single fracture propagating. Proposed algorithm consists of the Discrete Fracture Model for multi-phase flow and contact-enriched Finite Element Model for geomechanics. Irwin's failure criterion from Linear Elastic Fracture Mechanics concepts was adapted. Stress Intensity Factors are evaluated employing displacement extrapolation technique.

The proposed model was extensively tested in various set-ups including single- and multi-phase flow in isothermal and thermal conditions. Both straight and turning fractures were modeled. Effects of the mesh geometry, material properties, and stress field anisotropy were analyzed in a series of tests. Obtained results were validated with the semi-analytical solutions. Proposed numerical scheme demonstrated its applicability to a wide range of tasks and showed a great potential for its extension to a larger group of applications.

Contents

List of Figures ix

List of Tables xiii

1 Introduction 1
- 1.1 Problem Statement . . . 4
- 1.2 Code Development Goals . . . 4
- 1.3 Report Structure . . . 4

2 Theory and Numerical Schemes 7
- 2.1 Governing Equations . . . 7
  - 2.1.1 Fluid Flow . . . 7
  - 2.1.2 Poro-Elasticity . . . 7
  - 2.1.3 Thermo-Elasticity . . . 9
- 2.2 Fracture Mechanics . . . 10
  - 2.2.1 Stresses in the Near-Tip Zone . . . 11
  - 2.2.2 Stress Intensity Factors . . . 11
  - 2.2.3 Griffith Energy Criterion . . . 12
  - 2.2.4 Strain Energy Release Rate . . . 14
  - 2.2.5 Strain Energy Density Criterion . . . 15
  - 2.2.6 Irwin's Correction for Plastic Zone . . . 15
  - 2.2.7 Cohesive Zone Theory . . . 17
  - 2.2.8 J-Integral . . . 18
  - 2.2.9 Fracture Orientation . . . 19
  - 2.2.10 Adopted Concepts of Fracture Mechanics . . . 21
- 2.3 Numerical Modeling Techniques . . . 21
  - 2.3.1 Finite Element Method . . . 21
  - 2.3.2 Finite Element Method with Contact Plane . . . 22
  - 2.3.3 Quarter-Point Element . . . 23
  - 2.3.4 Enriched Element . . . 24
  - 2.3.5 Extended Finite Element Method . . . 25
  - 2.3.6 Stress Intensity Factor in Finite Element Method Approach . . . 26
  - 2.3.7 Adopted Numerical Approach . . . 27

3 Modeling Methodology 29
- 3.1 Discretized Governing Equations . . . 29
  - 3.1.1 Flow Equation . . . 29
  - 3.1.2 Heat Equation . . . 29
  - 3.1.3 Poro-Elasitic Equation . . . 30
- 3.2 Domain Discretization . . . 31
- 3.3 Fracture Opening Algorithm . . . 32
- 3.4 Model Geometry, Boundary and Initial Conditions . . . 33
- 3.5 Semi-Analytical Solution . . . 35

4 Model Validation and Testing **39**
4.1 Single-phase Fluid Injection . . . 39
4.1.1 Stationary Fracture . . . 39
4.1.2 Propagating Fracture . . . 41
4.2 Multi-Phase Fluid Injection . . . 44
4.2.1 Stationary Fracture under the Conditions of Favorable Displacement (Case 1) . . . 46
4.2.2 Stationary Fracture under the Conditions of Unfavorable Displacement (Case 2) . . . 46
4.2.3 Propagating Fracture under the Conditions of Favorable Displacement (Case 1) . . . 48
4.2.4 Propagating Fracture under the Conditions of Unfavorable Displacement (Case 2) . . . 50
4.3 Injection of Cold Single-Phase Fluid into Hot Reservoir with the Growing Fracture . . . 52
4.3.1 Material Contraction Along the Fracture . . . 54
4.4 Study of Model Sensitivity to Parameters . . . 54
4.4.1 Mesh Refinement Study . . . 54
4.4.2 Time Step Size Effect . . . 57
4.4.3 "Virtual" Fracture Segments Aperture Effect . . . 59
4.4.4 Initial Fracture Length Effect . . . 60
4.4.5 Effect of the Total Compressibility C_t . . . 60
4.4.6 Effect of the Fracture Toughness Value K_{Ic} . . . 63
4.4.7 Effect of the Fracture Path Tortuosity . . . 63
4.4.8 Effect of the Stress Anisotropy Level on Turning Fracture . . . 65

5 Application **69**
5.1 Model description . . . 69
5.2 Results . . . 70
5.3 Summary . . . 74

6 Conclusions and Recommendations **81**
6.1 Modifications to Classical DFM and FEM with Contacts . . . 81
6.2 Future Work . . . 83

Bibliography **85**

List of Figures

2.1 Flooded and cooled zones around the injection well and growing hydraulic fracture 9
2.2 Modes of the fracture opening . . . 11
2.3 Fracture geometry for analytical solution of stresses around the crack-tip . . . 12
2.4 Stress fields around a fracture tip for different combinations of K_{I} and K_{II} . . . 13
2.5 Strain energy density around a fracture tip for different combinations of K_I and K_{II} 16
2.6 Irwin's equivalent crack and plastic zone size . . . 16
2.7 Visualization of the cohesive forces theory. . . . 18
2.8 Way of calculating the J-integral in a general domain . . . 19
2.9 Wellbore images of Yufutsu field well in Japan . . . 20
2.10 Colored fracture in lab specimens sawed in halves . . . 20
2.11 2D illustration of the node duplication upon fracture segment opening . . . 22
2.12 Crack growth modeled using re-meshing . . . 22
2.13 Illustration of a contact and its integration into FE model . . . 23
2.14 Illustration of a quarter-point element . . . 24
2.15 SIF as a function of crack length (Source: Benzley, 1974 [10]) . . . 25
2.16 Illustration of XFEM method . . . 26
2.17 Illustration of the displacement extrapolation method . . . 28

3.1 2D illustration of two point flux approximation . . . 30
3.2 Illustration of a grid structure . . . 33
3.3 Algorithm of fracture propagation . . . 34
3.4 Model dimensions, boundary conditions and employed grid . . . 35

4.1 Simulation results of a non-propagating fracture . . . 40
4.2 Comparison of the pressure dynamics inside the stationary fracture with the analytic solution . . . 42
4.3 Correspondence between the injection rate Q and the dimensionless parameter q_D . . . 42
4.4 Map of the fracture activity and pressure field before the fracture started to grow. 43
4.5 Map of the fracture activity and pressure field at the end of the fracture growth . 43
4.6 Development of the fracture length and the pressure in case of the single-phase fluid injection . . . 44
4.7 Relative permeability curves and saturation profile for case 1 . . . 46
4.8 Relative permeability curves and saturation profile for case 2 . . . 47
4.9 Pressure growth inside the stationary fracture in the multi-phase flow conditions for the case 1 . . . 47
4.10 Water saturation profiles for favorable and unfavorable displacement types . . . 48
4.11 Pressure development inside the stationary fracture in the multi-phase flow conditions for the case 2 . . . 49
4.12 Comparison between numeric and analytic solutions for L_D in conditions of multi-phase flow (case 1) . . . 49
4.13 Comparison between numeric and analytic solutions for p_D in conditions of multi-phase flow (case 1) . . . 50

4.14 Comparison between the numeric and the analytic solutions for L_D in conditions of multi-phase flow (case 2) . . . 51
4.15 Comparison between numeric and analytic solutions for p_D in conditions of multi-phase flow (case 2) . . . 51
4.16 Comparison between numeric and analytic solutions of P_D and L_D in the thermal simulation (case 1) . . . 53
4.17 Comparison between numeric and analytic solutions of P_D and L_D in the thermal simulation (case 2) . . . 54
4.18 Effective stress maps around the crack in (a) horizontal σ_0 and (b) vertical σ_1 directions . . . 55
4.19 Secondary thermal fracutres perpendicular to a fracture face . . . 55
4.20 Fracture length comparison in the mesh refinement study . . . 56
4.21 Pressure inside the fracture in the mesh refinement study . . . 57
4.22 Development of the Stress Intensity Factor for Mode I K_I in the mesh refinement study . . . 58
4.23 Fracture length comparison in the time step refinement study . . . 58
4.24 Pressure inside the fracture in the time step refinement study . . . 59
4.25 Development of the Stress Intensity Factor for Mode I K_I in the time step refinement study . . . 60
4.26 Fracture length comparison in the variation of the "virtual" fracture segment aperture study . . . 61
4.27 Pressure inside the fracture comparison in the variation of the "virtual" fracture segment aperture study . . . 61
4.28 Fracture length comparison in the variation of the initial fracture length . . . 62
4.29 Pressure inside the fracture comparison in the variation of the initial fracture length . . . 62
4.30 Fracture length comparison in the variation of the total system compressibility C_t 63
4.31 Pressure inside the fracture comparison in the variation of the total system compressibility C_t . . . 64
4.32 Fracture length comparison in the variation of the fracture toughness value K_{Ic} . . 64
4.33 Pressure inside the fracture comparison in the variation of the fracture toughness value K_{Ic} . . . 65
4.34 Fracture path for geometries with no horizontal line in front of the initial fracture 65
4.35 Comparison of fracture lengths in time for meshes without horizontal path for the fracture . . . 66
4.36 Pressure development for meshes without horizontal path for the fracture . . . 66
4.37 Turning fracture trajectory for anisotropic stress fields with ratios σ_h/σ_H equal (a) $1:1.05$, (b) $1:1.075$ and (c) $1:1.1$ . . . 68

5.1 Inverted nine-spot injection pattern and simulated part of it . . . 70
5.2 Fracture conductivity as a function of its aperture (left part) and normal traction (right part) . . . 72
5.3 Pressure and water saturation profiles across the domain in the simulation with $Q_{\mathrm{inj}} = 9$ m^3/day/m after 3 years . . . 73
5.4 Dynamics of the Bottom Hole Pressures and the produced water volumes throughout the simulation with $Q_{\mathrm{inj}} = 9$ m^3/day/m . . . 74
5.5 Pressure and water saturation profiles across the domain in the simulation with $Q_{\mathrm{inj}} = 21$ m^3/day/m after 3 years . . . 75
5.6 Dynamics of the Bottom Hole Pressure at the injector and the fracture length, and the produced water volumes throughout the simulation with $Q_{\mathrm{inj}} = 21$ m^3/day 76

5.7 Normalized Bottom Hole Pressure at the injector and the produced water volume for simulations with $Q_{\text{inj}} = 9$ and 21 m^3/day 76
5.8 Bottom hole pressure at the injector normalized by the minimum horizontal stress σ_h against volume of the injected water V_{injw} normalized by the displaceable pore volume V_{dpor}. 77
5.9 Fracture length normalized by the minimum distance between 2 wells W against volume of the injected water V_{injw} normalized by the displaceable pore volume V_{dpor}. 77
5.10 Produced water volume normalized by volume of the injected water against time 78
5.11 Produced water volume normalized by volume of the injected water against volume of the injected water V_{injw} normalized by the displaceable pore volume V_{dpor}. 78
5.12 Solution for fracture length obtained on meshes with average size equal to 5 and 10 m. 79

List of Tables

4.1 Fluid and rock properties used in the single-phase simulation 41
4.2 Fluid properties used in the multi-phase simulation 45
4.3 Fluid and rock properties used in the thermal simulation 52

5.1 Fluid and rock properties used in the practical example 71

1

Introduction

There are certain technological activities where injection of fluid or gas into subsurface is exploited. Fields where these activities are routinely done comprise extraction of geothermal energy, development of unconventional hydrocarbon reservoirs, disposal of wastewater, sequestration of CO2, storage of natural gas and Enhanced Oil Recovery. Injection of substances into porous media leads to changes in its pressure, temperature and stress states. The latter can potentially lead to generation of hydraulic fractures or activation of pre-existing faults, which directly affects exercised activity and even human comfort. This makes fracture mechanics very important when alteration of subsurface state is considered.

Thermal energy can be extracted from subsurface by drilling wells into a formation, injecting cold fluid through one well and extracting hot fluid from another. Further, heat from this fluid can be transformed into electricity. Circulation of the fluid underground is facilitated by the natural permeability of the rock or by permeability induced by hydraulic fracturing. The latter is done in Enhanced Geothermal Systems (EGS) [97]. Knowledge of induced fractures concentration, their geometry and growth speed is not only necessary for design and optimization of such systems, but also for safety reasons. It is well established, that hydraulic fracturing can lead to anthropogenic earthquakes [70, 73, 82, 112, 112]. Another reason for seismicity can be reactivation of faults. It owes to the increase of fluid pressure in the close proximity to pre-existing fault and successive reduction of the effective normal stress acting perpendicular to it. Extraction of geothermal energy is often accompanied by induced seismicity. Number of geothermal projects registered generation of seismicity associated with fluid injection. Such events were reported in 1983 in the Fenton Hill Enhanced Geothermal System project in New Mexico, USA [14], in 2006 in Basel EGS, Switzerland [44] and in 2013 in the geothermal project near St. Gallen in Switzerland [80]. The last two projects were suspended due to observed seismic events. Thus, ability to predict hydraulic fracturing and behavior of faults is crucial for feasibility of geothermal projects.

Unconventional hydrocarbon reservoirs are low-permeable formations that contain considerable amounts of oil or gas. Their extraction by conventional methods is complicated due to low permeability of the rock. In order to increase it, reservoir is hydraulically fractured. For doing so, horizontal section of a well is divided into isolated stages which are sequentially pressurized until creation of new fractures [111]. Ability to predict induced fracture geometry is necessary for efficient field development.

King et al. [61] reported an average volume of fluid injected into one well for hydrofracking purposes is of order $20,000$ m^3. Approximately $60-90\%$ of this volume remains underground causing changes in pressure and stress fields. The rest of the fluid returns back to the surface in the form of wastewater. Apart from initially contained chemicals, it is contaminated with reser-

voir gases, metals and radioactive materials. Produced wastewater is commonly disposed back to subsurface [110]. Its injection in close proximity to pre-existing faults caused generation of seismicity at the number of cites. Keranen et al. and Zhang et al. report induced quakes due to massive wastewater injection in central Oklahoma, Arkansas and Ohio, USA [58, 119]. Van de Hoek describe re-injection of unfiltered production water under fracturing conditions in Oman [101]. Modeling of hydraulic fractures and fault reactivation due to wastewater injection is necessary for prediction of associated earthquakes.

Injection of natural gas into the formation for storage purposes or geological sequestration of CO2 may also trigger seismicity. The most recent human-felt seismic events were registered in 2013 at the Castor natural gas storage site, Spain [16]. Although no human-felt seismicity was detected in the CO2 storage projects [52], micro-seismicity was reported from several sequestration sites [106]. Zoback and Gorelick warn that even small- to moderate-sized earthquakes threaten the seal integrity of CO2 repositories [122].

Another field where fractures play significant role is Enhanced Oil Recovery. During exploitation of the oil or gas fields, operators often face the problem of maintaining the reservoir pressure, necessary for efficient extraction of hydrocarbons. One way of doing so is waterflooding: method of water injection into the reservoir with aim of maintaining the reservoir pressure and displacing the hydrocarbons [67]. Number of well-test researchers [3, 62, 64] report growth of unstable hydraulic fractures in the injection wells and their effect on field performance. The fractures originate at the surface of injecting well and have lengths comparable with distances to neighboring wells [98]. The fact that fractures are hydraulically much more conductive than continuous rock, makes them a preferable path for the injected fluid to reach the production well, therefore increasing the risk of water breakthrough. When densifying the production wells network, the operating company can unintentionally place a new well in the effective proximity to the existing hydraulic fracture, jeopardizing its efficiency from the beginning.

Production wells, in their turn, can also have connected fractures caused by hydrofracking operations or drilling with excessive mud weight. These fractures would normally orient in the same direction as the waterflood-induced fractures. Having the hydraulic cracks at injection and production wells co-oriented, under certain conditions, can lead to their unification and 100% watercut at the production well.

Apart from water breakthrough prevention, knowledge of fractures geometry can be used for field development plan optimization. Being able to predict an approximate fracture length and its direction, oil field operator can reduce the number of injection wells and bring the production and injection zones as close to each other as possible, without additional costs [4].

From described examples, important role of pre-existing or induced discontinuities during anthropogenic interference into subsurface becomes obvious. In order to produce energy from subsurface or store highly pressurized substances underground, and perform it in efficient and safe manner, study of fractures and faults behavior is essential.

In order to model hydraulic fractures, analytical and numerical models are employed. They are obtained by solving equations of fluid flow and mechanical deformation of rock. Currently, there is a number of analytical solutions for a single hydraulic crack in a homogeneous continuous medium subjected to uniform stress field. Two of the most common 2D models used in fracture treatment design are the Khristianovic-Geertsma-de Klerk (KGD) [36, 59] and the Perkins-Kern-Nordgren (PKN) [79, 84] models. Their solutions are applicable for induced fractures in low-permeable rock, where effect of pressure field alteration around the fracture can be disregarded.

Analytic solutions for slow fractures, typical for waterflooding or water disposal, comprise research by Hagoort [41] and Koning [63]. In their studies, poro- and thermo-elastic contri-

bution to stress field are accounted. 2D fracture models (fracture length and width) were extended to allow variable fracture height in pseudo-three-dimensional (P3D) formulation. The P3D concept in modeling hydraulic fractures was introduced by Settari et al. [90]. This research was further extended by Van Den Hoek et al. [105], who also proposed to evaluate the dimensions and degree of containment of waterflood-induced fractures from pressure-transient analysis [102].

While being effective and cheap tool for conceptual design of a single fracture, analytical models are hardly applicable for field cases due to the assumptions they are based on. In field applications, assumptions of homogeneous rock properties, stress and pressure field symmetry and model's 2-dimensionality do not hold anymore. For that reason, a number of numerical models were developed to tackle the hydraulic fracturing process at the reservoir scale.

In principle, two different groups emerged over the years. The first type couples the finite-volume reservoir simulator with analytical P3D fracture model. The fracture is included into the reservoir simulator as extension of the well. Such models were developed and tested in [24, 49].

Another group of approaches uses full three-dimensional numerical representation of the fracture. For modeling flow in porous media with discrete fractures, several techniques were applied. Within finite-volume approach, following studies stand out [38, 57, 75]. Some authors used finite-element approach to model multi-phase flow in discrete fracture models [53, 55, 60]. Mixed finite-element method was used in [47, 69]. Discontinuous Galerkin method, in its turn, was employed in [29, 46].

Mechanical part is commonly modeled by finite- and boundary-element approaches [20, 48, 121]. Recently, Nordbotten proposed usage of finite-volume method for both flow and mechanics modeling [78]. In order to make fracture path mesh-independent, eXtended Finite-Element Method (XFEM) was developed in [25, 26]. This approach was further combined with cohesive crack model in [114]. For situations of complex crack topologies, where discontinuous crack representation can be complicated, diffusive crack model was introduced by continuum damage approach [54], phase-field approach [71, 72] and level set model [74].

For modeling hydraulic fractures and pre-existing faults, contact mechanics concept is appealing, as it allows to have frictional resistance to sliding. Treatment of fractures as surfaces in contact was extensively studied by means of finite-element [94], extended finite-element [68] and mortar methods [87]. Classical approaches used for the construction of discretization scheme for nonlinear contact problem are the methods of Lagrange multipliers and penalty regularization [94, 96]. Nitsche's method for treating the contact problem was proposed in [43].

Discrete Fracture Model (DFM), developed by Karimi-Fard et al. [56] for simulating fluid flow in fractured rock, has proven its excellent applicability for large scale problems. The proposed DFM model allows accurate representation of the pressure and fluid distributions since all the fractures are taken into account explicitly. DFN was implemented in the Automatic Differentiation General Purpose Reservoir Simulator (AD-GPRS) developed in Stanford University [109]. AD-GPRS posses an extensive set of nonlinear formulations [107, 108, 116], flexible spatial discretization [120] and advanced physics models [32, 34, 117]. DFM was further extended by Garipov et al. to include geomechanics [33]. It is done by coupling the fluid flow equations, discretized using the finite-volume method, with poro-elasticity equations, discretized using finite-element method. Fracture is treated as surfaces in contact. The extended geomechanics model for DFM inherits all benefits of the original method and allows to represent fracture properties, such as aperture and stresses, on each fracture. This work has proven to be effective and stable in modeling hydro-mechanical behavior of pre-existing non-propagating fractures and faults on a large scale. Fracture initiation and propagation, as well as mechanisms of rock failure were not addressed in their work.

1.1. Problem Statement

Contact mechanics is properly suited for modeling discontinuities in rock. Its combination with efficient technique to model fluid flow in fractured media was developed and successfully tested on reservoirs with stationary fractures and faults [33]. Empowering this combination to model growing hydraulic fractures could broaden the spectrum of problems which researchers can investigate. In order to do so, following research questions have to be answered:

- How the combination of classical DFM scheme and finite-element model with contacts should be modified to allow for dynamic addition of fracture segments?
- Which fracture propagation criterion is suitable for this numerical scheme?
- How can fracture grow more than one finite segment in one time step?
- How sensitive is the model to the average mesh size and time step?
- How sensitive is the model to anisotropic stress field?
- How sensitive is it to certain material parameters?

1.2. Code Development Goals

The project tends to improve the existing geomechanical model in AD-GPRS in cooperation with researchers from CiTG at TU Delft and SUPRI-B group at Stanford University. The developed code should be readily applicable to related research and meet the following requirements:

- Be applicable at the reservoir scale.
- Be stable, accurate and mesh-objective.
- Account for poro- and thermo-elasticity effects.
- Be capable of both fracture opening and closure.
- Be capable of opening several fracture segments in one time step.
- Be capable to predict brittle material failure.
- Be implemented in 2D, but expandable to 3D.
- Be validated with existing (semi-) analytic solutions for fracture growth.

1.3. Report Structure

The structure of the report is summarized below. In chapter 2, equations governing physics of fluid and heat flow, solid deformation and fracture growth are reviewed. Numerical schemes commonly used in fracture modeling are also compared. This chapter is completed by justification of the methods adopted in the developed approach. In chapter 3, the discretization of the flow and mechanics equations implemented in the numerical scheme is discussed. Further, the employed grid generation and fracture propagation algorithms are explained. The model description, boundary and initial conditions are followed by semi-analytical solution, used for the model validation. In chapter 4, results of numerical simulations are shown and compared with semi-analytical solutions. Such results are given for stationary and propagating fractures in conditions of single- and multi-phase flows, as well as in iso- and non-isothermal conditions. The chapter is completed by study of model sensitivity to the key parameters. Chapter 5 describes possible application of the developed model to a practical case, namely waterflooding

operations. Obtained results may serve for redesign of the injection pattern and optimization of the operations. In chapter 6, the results of the research are summarized and the recommendations for the future work are given.

2

Theory and Numerical Schemes

2.1. Governing Equations

Physics of hydraulic fracture propagation is governed by laws of fluid and heat flow through porous media, deformation of rock and brittle fracture opening. In this chapter, theoretical background for each of these fields is reviewed.

2.1.1. Fluid Flow

The flow equation for compressible single-phase fluid is obtained by combining the mass conservation equation:

$$\frac{\partial(\rho_f \phi)}{\partial t} + \nabla \cdot (\rho_f \mathbf{v}) - q = 0 \,, \tag{2.1}$$

with Darcy's law:

$$\mathbf{v} = -\frac{\mathbf{k}}{\mu_f}(\nabla p - \rho_f \mathbf{g}) \,, \tag{2.2}$$

which at the end yields:

$$\frac{\partial(\rho_f \phi)}{\partial t} - \nabla \cdot \left[\rho_f \frac{\mathbf{k}}{\mu_f}(\nabla p - \rho_f \mathbf{g}) \right] - q = 0 \,. \tag{2.3}$$

In the above expressions, p is the fluid pressure, $\mathbf{v}$ is the fluid velocity, ρ_f and μ_f are the density and the viscosity of the fluid, ϕ is the porosity of the matrix, $\mathbf{k}$ is the permeability tensor, q is the source term, and $\mathbf{g}$ is the gravity vector.

2.1.2. Poro-Elasticity

Poro-elasticity is the theory describing interaction between porous media and fluid flowing through. Equations of poro-elasticity relate strains of a solid matrix with stress in solids and pressure of liquid. Starting point in obtaining the mechanical formulation is the momentum conservation equation for solid skeleton and pore fluid:

$$\nabla \cdot \boldsymbol{\sigma} + \rho \mathbf{g} = 0 \,, \tag{2.4}$$

where $\boldsymbol{\sigma}$ is the total stress tensor.

Adapting the infinitesimal strain theory, strain tensor $\boldsymbol{\epsilon}$ can be expressed through displacement vector $\mathbf{u}$ as follows:

$$\boldsymbol{\epsilon} = \frac{1}{2}(\nabla \mathbf{u} + \nabla^T \mathbf{u}) \,. \tag{2.5}$$

Much of the poro-elastic theory comes out from the work of Biot [11]. It states that the deformation of poro-elastic media is caused by variation of the effective stress $\boldsymbol{\sigma}''$, which is related to the total stress $\boldsymbol{\sigma}$ by the fluid pressure p and the Biot coefficient α:

$$\boldsymbol{\sigma} = \boldsymbol{\sigma}'' - \alpha \mathbf{I} p \,, \tag{2.6}$$

where $\mathbf{I}$ is the identity matrix. Expression 2.6 can be further extended by incorporating constitutive relation between the effective stress $\boldsymbol{\sigma}''$ and strain tensor $\boldsymbol{\epsilon}$ by means of fourth-order tangent stiffness matrix K:

$$\boldsymbol{\sigma} = K : \boldsymbol{\epsilon} - \alpha \mathbf{I} p \,. \tag{2.7}$$

As failure phenomenon in reservoirs is commonly modeled through activation of faults and growth of fractures, plastic deformation is disregarded. Non-damaged reservoir rock is assumed to behave elastically, and Hooke's law is adapted as a constitutive relation. It can be written in terms of the Lamé parameters λ and μ:

$$\boldsymbol{\sigma} = 2\mu\boldsymbol{\epsilon} + \lambda \mathrm{trace}(\boldsymbol{\epsilon})\mathbf{I} - \alpha \mathbf{I} p \,. \tag{2.8}$$

Equation of poro-elastic equilibrium is derived by combination of the momentum conservation equation 2.4 and definition of the total stress 2.6:

$$\nabla \cdot \boldsymbol{\sigma}'' + \rho \mathbf{g} - \alpha \nabla p = 0 \,. \tag{2.9}$$

Material parameters such as porosity and permeability differ with changes in pressure and strains. Porosity update can be modeled as follows [19]:

$$\phi = \phi_0 + \alpha(\epsilon_v - \epsilon_{v,0}) + \frac{(\alpha - \phi_0)(1-\alpha)}{K_d}(p - p_0) \,, \tag{2.10}$$

where K_d is the drained bulk modulus, and $\epsilon_v = \epsilon_{11} + \epsilon_{22} + \epsilon_{33}$ is the volumetric strain. Advantage of this formulation is that by equating α to 0, we can perform one-way uncoupling of mechanical problem from flow.

Another approach for modeling the porosity change was proposed by Jaeger et al. [51]. They define the porosity change by means of the bulk compressibility of the fluid filled matrix C_{bc}, the bulk compressibility of the rock-forming minerals C_m, the pressure inside the pores p_p, and the confining pressure p_c:

$$\phi = \phi_0 - [(1-\phi_0)C_{bc} - C_m](p_c - p_p) \,. \tag{2.11}$$

Deformation of the rock affects its permeability. The latter can be calculated by David's model [22]:

$$k = k_0 \left(\frac{\phi}{\phi_0}\right)^n \,, \tag{2.12}$$

where k_0 and ϕ_0 are the reference permeability and the porosity of porous media respectively, and n is a fitted parameter. Another method to determine the permeability was proposed by Carman [15]. It was developed considering flow through a porous media, similar to a flow through a bundle of capillary tubes. It states:

$$k = \frac{1}{k_0 S^2} \frac{\phi^2}{(1-\phi)^2} \,, \tag{2.13}$$

where k_0 is the factor depending on a pore shape and a ratio of length of actual flow path to soil bed thickness, and S is a specific surface area.

Fluid density is related to the pressure through its compressibility:

$$\rho_f = \rho_{f,0}(1 - C_f \Delta p) \,, \tag{2.14}$$

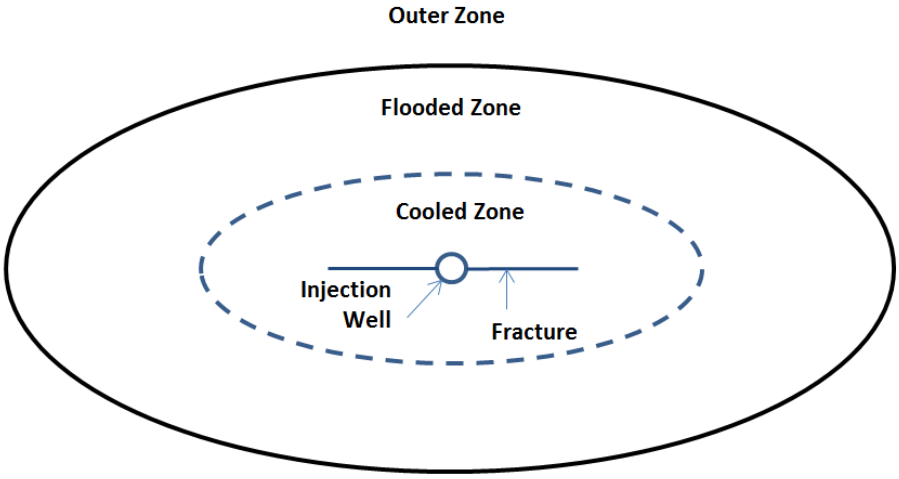

Figure 2.1: Artistic representation of flooded and cooled zones around the injection well and growing hydraulic fracture

where C_f is the compressibility of the fluid, $\rho_{f,0}$ and ρ_f are the initial and current fluid densities respectively.

Coupling between mechanical and flow problems is performed by update of the pressure p and the effective stress $\boldsymbol{\sigma}''$ in a flow-to-mechanics direction and by update of the permeability k, porosity ϕ and fluid density ρ_f in mechanics-to-flow direction.

2.1.3. Thermo-Elasticity

Thermo-elasticity describes the effect of changes in the stresses and displacement of the body due to changes in its temperature. Theory of thermo-elasticity resemble poro-elasticity for the following reasons:

1. Temperature change in isotropic body, similar to pressure change, creates normal strains equal in three principal directions and zero shear.

2. Both temperature and pressure fields are governed by dissipation-type equations.

The effect of the temperature change plays significant role in development of a fracture. Fluids injected into a well during waterflooding operations normally come at lower temperature than the reservoir. Filtration of the injected fluid from existing fracture into the formation cools down the rock within a flooded zone. The cooled region grows as more fluid is injected (see fig. 2.1). Reservoir rock within cooled region contracts, leading to reduction of horizontal stresses in all directions. Reduced minimal horizontal stress σ_h results in lower pressure needed for fracture to initiate and to grow, and as a result, the larger fracture extent.

The theory of thermo-elasticity was developed by Duhamel in 1833 [28]. Temperature change inside a solid piece of rock leads to its expansion or contraction depending on the value of temperature difference:

$$\boldsymbol{\epsilon} = -\boldsymbol{\beta}(T - T_0)\,, \tag{2.15}$$

where $\boldsymbol{\beta}$ is the second-order thermal expansivity tensor. Combination of thermo- and poro-elastic strains yields:

$$\boldsymbol{\epsilon} = \frac{1}{2\mu}\boldsymbol{\sigma} - \frac{\nu}{2\mu(1+\nu)}\mathrm{trace}(\boldsymbol{\epsilon})\mathbf{I} - \frac{\alpha}{3K}\mathbf{I}p - \beta\theta\mathbf{I}\,, \tag{2.16}$$

where K is the macroscopic bulk modulus and θ is the temperature difference $T - T_0$. Inversion of the equation 2.16 yields following expression for stresses:

$$\boldsymbol{\sigma} = 2\mu\boldsymbol{\epsilon} + \lambda \mathrm{trace}(\boldsymbol{\epsilon})\mathbf{I} - \alpha\mathbf{I}p - \beta\theta\mathbf{I}\,. \tag{2.17}$$

Following Noorishad et al.[77], equation accounting for fluid and heat flow is obtained by combination of the mass conservation equations (2.1) with the total energy conservation equation, where thermal equilibrium between fluid and solid skeleton is assumed:

$$\frac{\partial}{\partial t}(\rho C)_M + \rho_f C_{vf}\frac{\mathbf{K}}{\mu_f}\cdot(\nabla p - \rho_f \mathbf{g})\cdot\nabla T = \nabla\cdot\mathbf{K_M}\cdot\nabla T, \tag{2.18}$$

where T is the temperature, $(\rho C)_M$ and K_M are the specific heat capacity and thermal conductivity of the fluid-filled media, defined as

$$\begin{aligned}(\rho C)_M &= \phi\rho_f C_{vf} + (1-\phi)\rho_s C_{vs}\\ \mathbf{K_M} &= \phi\mathbf{K_f} + (1-\phi)\mathbf{K_s}.\end{aligned} \tag{2.19}$$

In the above equations, C_{vf} and C_{vs} are the fluid specific heat capacities, and $\mathbf{K_f}$ and $\mathbf{K_s}$ are the thermal conductivity of fluid and solid.

Change in the rock temperature trigger variation of its porosity. In accordance with Coussy [19], equation 2.10 is modified to account for the thermal effect:

$$\phi = \phi_0 + \alpha(\epsilon_v - \epsilon_{v,0}) + \frac{(\alpha-\phi_0)(1-\alpha)}{K_d}(p - p_0) - 3\beta\Delta T\,. \tag{2.20}$$

2.2. Fracture Mechanics

Let us consider a finite body with a crack in the middle. This body is subjected to the global tensional stress $\boldsymbol{\sigma}$ applied at the boundaries. Presence of the discontinuity leads to intensification of stresses at sharp edges. Increase of stress value in the near-tip area σ up to the material tensile strength $\sigma_T S$ leads to development of a plasticity zone. The theory of fracture mechanics distinguish following scenarios of material failure in such setting. The classification given by Pluvinage is followed [85].

1. The plastic zone around the tip is relatively small. Material fails as a result of fast and unstable fracture growth. This process is commonly modeled by means of Linear Elastic Fracture Mechanics (LEFM).

2. The plastic zone is relatively wide, but it does not reach boundaries of a specimen. In such case, failure mechanism is described by the laws of elasto-plastic fracture mechanics. Nevertheless, LEFM with correction of the plastic zone gives a reasonable solution to this problem.

3. The plastic zone reaches the edges of the specimen and has a shape of stripes originating at the fracture tips.

4. The whole specimen is subjected to plasticity. Failure mechanics problem can be solved through the limit state analysis.

In problems of hydraulic fractures, the material state can vary from 1st to 2nd, depending on material properties and load values.

In figure 2.2, different modes of fracture opening are shown. In mode I, the displacement of the fracture surface is perpendicular to the fracture plane. Mode II takes place when the displacement of the fracture is parallel to the fracture plane and perpendicular to its front. Mode III occurs when displacement of the fracture is in the plane of the fracture and parallel to its front. Three modes can also combine into mixed modes.

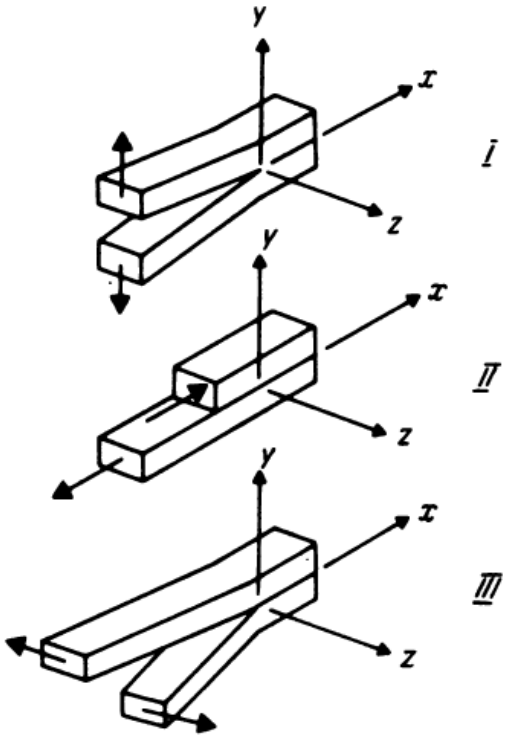

Figure 2.2: Modes of the fracture opening (Source: G. Pluvinage. Elasto-plastic mechanics of failure. In translation. Page 16.[86])

2.2.1. Stresses in the Near-Tip Zone

The three basic modes of crack deformation can be more precisely defined by associated stress ahead of the crack tip. In current subsection, a 2D specimen with pre-existing crack is considered. In such case, only mode I or II are possible. Polar system of coordinates is adopted. Solution to the equilibrium equations 2.9 for stresses in the near-tip area defines tangential $\sigma_{\theta\theta}$, radial σ_{rr} and shear stress $\tau_{r\theta}$ before failure as:

$$\begin{aligned}
\sigma_{\theta\theta} &= \frac{1}{2\sqrt{2\pi r}}[K_I(1+\cos\theta) - 3K_{II}\sin\theta]\cos\frac{\theta}{2}\,, \\
\sigma_{rr} &= \frac{1}{2\sqrt{2\pi r}}\left[K_I(3-\cos\theta) + K_{II}(3\cos\theta - 1)\sin\frac{\theta}{2}\right]\,, \\
\tau_{r\theta} &= \frac{1}{2\sqrt{2\pi r}}[K_I\sin\theta + K_{II}(3\cos\theta - 1)]\cos\frac{\theta}{2}\,,
\end{aligned} \tag{2.21}$$

where θ is the angle between the fracture plane and a line connecting fracture tip with the point of interest, r is the distance from the tip to this point (see figure 2.3), and K_{I} and K_{II} are the Stress Intensity Factors (SIFs) for mode I and mode II respectively.

2.2.2. Stress Intensity Factors

K_{I}, K_{II} and K_{III} are formally defined as [89]:

$$\begin{aligned}
K_{\mathrm{I}} &= \lim_{r\to 0}\sqrt{2\pi r}\,\sigma_{yy}(r,0)\,, \\
K_{\mathrm{II}} &= \lim_{r\to 0}\sqrt{2\pi r}\,\sigma_{yx}(r,0)\,, \\
K_{\mathrm{III}} &= \lim_{r\to 0}\sqrt{2\pi r}\,\sigma_{yz}(r,0)\,,
\end{aligned} \tag{2.22}$$

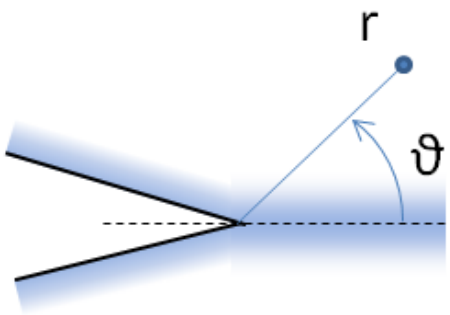

Figure 2.3: Fracture geometry for analytical solution of stresses around the crack-tip

where values in the brackets are the distance r from the crack tip to the point and the angle of deviation θ. Analytical solutions for K_{I}, K_{II} and K_{III} for different geometries are derived and available in the literature [66, 89].

The Stress Intensity Factor for a through crack of length $2a$, at right angles, in an infinite plane, subjected to a uniform stress field σ (see figure 2.3) is [89]:

$$K_{\mathrm{I}} = \sigma\sqrt{\pi a}\,. \tag{2.23}$$

By means of the analytic solution 2.21, stresses around the fracture tip at an arbitrary radius r and different combinations of unitless K_{I} and K_{II} could be calculated and plotted in figures 2.4. Effect of the Stress Intensity Factors (SIFs) on the stresses is clear in these plots. Variation in SIFs permits reproduction of the stress fields typical for specific fracturing mode. In that way, mode I fracture ($K_{\mathrm{I}} > 0$ and $K_{\mathrm{II}} = 0$) has the highest tangential and zero shear stresses in front of the tip (figure 2.4a). This direction coincides with the principle plane as the stress normal to it has the maximum value and the shear component equals to zero. For mixed mode I+II, where both $K_I > 0$ and $K_{II} > 0$, the principle plane is deviated from the fracture direction (see figures 2.4b,c). For the pure mode II (fig. 2.4d), the shear stress $\tau_{r\theta}$ maximizes on the fracture plane, while maximum tangential stress is acting on the plane at approximately $-70°$. The direction of failure and mode in which material fails depends on its brittleness. Fracture in a brittle material, such as glass, extends by splitting in the direction of $-70°$ (mode I), while ductile material fails plastically, developing the shear band in the direction of $0°$.

The simplest failure criterion is defined by three SIFs and has the form $f(K_{\mathrm{I}}, K_{\mathrm{II}}, K_{\mathrm{III}}) = 0$. For mode I, this criterion is

$$K_{\mathrm{I}} \leq K_{\mathrm{Ic}}\,, \tag{2.24}$$

where K_{Ic} is the fracture toughness. Equation 2.24 is known as the Irwin's criterion for linear elastic failure [50].

2.2.3. Griffith Energy Criterion

The Griffith energy criterion [39] states that unstable propagation of a crack decreases strain energy of a system and takes place when incremental release of energy dW is greater than incremental increase of surface energy dW_s:

$$dW \geq dW_s\,. \tag{2.25}$$

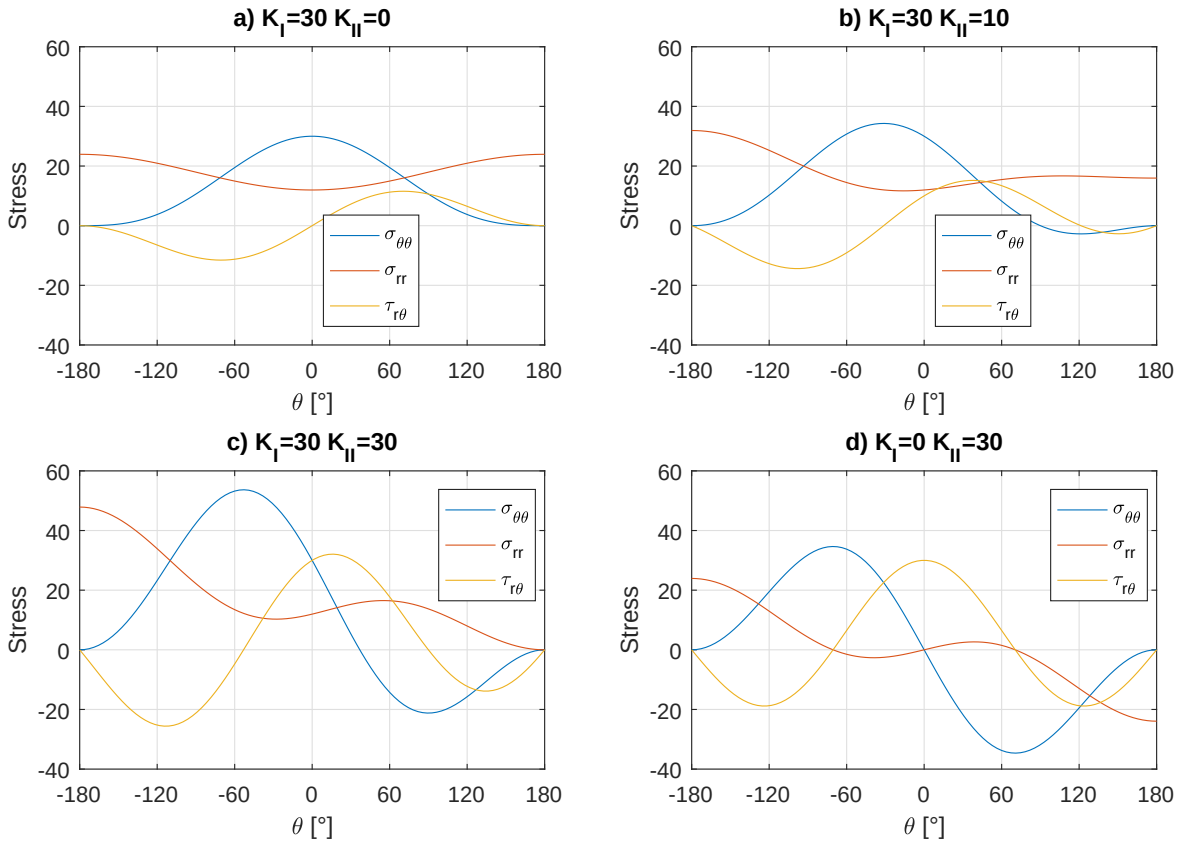

Figure 2.4: Stress fields around a fracture tip for different combinations of K_{I} and K_{II}

Having equations for release of energy and surface energy, Griffith arrived at expression for critical stress applied at infinity σ_{cr}, which led to fracture propagation:

$$\begin{aligned} \sigma_{cr} &= \sqrt{\frac{2E\gamma}{\pi a}} \quad \text{(plane stress)}, \\ \sigma_{cr} &= \sqrt{\frac{2E\gamma}{\pi(1-\nu^2)a}} \quad \text{(plane strain)}, \end{aligned} \tag{2.26}$$

where E is the Young's modulus, γ is the surface energy density, ν is the Poisson's ratio, and a is the fracture half-length.

2.2.4. Strain Energy Release Rate

Strain energy release rate per crack tip G can be expressed through the incremental release of energy dW:

$$G = \frac{dW}{2a}\,. \tag{2.27}$$

Then instability condition can be re-written in terms of strain energy release rate G:

$$G \geq 2\gamma\,. \tag{2.28}$$

Theoretically, the fracture propagates as soon as the energy release rate G becomes equal to 2γ. However in practice, fracture propagates at much higher values of energy release rates. The reason behind is occurrence of plastic deformations near the crack tip. If this additional plastic work γ_p is to be taken into account, the instability condition is [81]:

$$G \geq 2\gamma + \gamma_p\,, \tag{2.29}$$

and critical stress at infinity is defined as:

$$\begin{aligned} \sigma_{cr} &= \sqrt{\frac{EG}{\pi a}} \quad \text{(plane stress)}, \\ \sigma_{cr} &= \sqrt{\frac{EG}{\pi(1-\nu^2)a}} \quad \text{(plane strain)}. \end{aligned} \tag{2.30}$$

For brittle materials, surface energy term dominates and $G \approx 2\gamma$, while for ductile materials, plastic term is the dominating one $G \approx \gamma_p$.

Irwin showed that the strain energy release rate G and the SIFs are related through the following expressions:

$$\begin{aligned} G_I &= \frac{K_{\mathrm{I}}^2(1-\nu^2)}{\pi E}\,, \\ G_{II} &= \frac{K_{\mathrm{II}}^2(1-\nu^2)}{E} \quad \text{(plane strain)}, \\ G_{III} &= \frac{K_{\mathrm{III}}^2(1+\nu)}{E}\,. \end{aligned} \tag{2.31}$$

If mixed mode is taking place, the total strain energy release rate can be calculated as:

$$G = G_I + G_{II} + G_{III}\,. \tag{2.32}$$

Then the Griffith energy criterion modified by Irwin looks like:

$$G = G_{Ic}\,, \tag{2.33}$$

where G_{Ic} is the fracture energy, which is material specific.

2.2.5. Strain Energy Density Criterion

When mixed mode failures is expected, Sih's criterion [93] is appealing. It is based on the local strain energy density concept. The energy density S is defined as follows:

$$\frac{S}{r} = \frac{dU}{dV}, \tag{2.34}$$

where dU/dV is the change of strain energy per unit volume and r is the distance from the fracture tip. At the moment of failure, this density reaches the critical value S_{cr}. Change in strain energy at distance r from the tip, in its turn, is defined by the stress intensity factors. After some elaborations, one arrives at the expression for the strain energy density:

$$S = a_{11}K_{\mathrm{I}}^2 + 2a_{12}K_{\mathrm{I}}K_{\mathrm{II}} + a_{22}K_{\mathrm{II}}^2 + a_{33}K_{\mathrm{III}}^2, \tag{2.35}$$

where coefficients a_{11}, a_{12}, a_{22} and a_{33} are defined as:

$$\begin{aligned} a_{11} &= (1/16\mu)[(1+\cos\theta)(\kappa-\cos\theta)], \\ a_{12} &= (1/16\mu)2\sin\theta[\cos\theta-(\kappa-1)], \\ a_{22} &= (1/16\mu)[(\kappa+1)(1-\cos\theta)+(1+\cos\theta)(3\cos\theta-1)], \\ a_{33} &= 1/4\mu. \end{aligned} \tag{2.36}$$

Here, $\kappa = (3-\nu)/(1+\nu)$ for plane stress and $\kappa = 3-4\nu$ for plane strain conditions, and μ is the shear modulus.

Sih's failure criterion states:

1. Fracture propagates in the direction of the minimum strain energy density at angle θ_0:

$$\frac{\partial S}{\partial \theta} = 0, \quad \frac{\partial^2 S}{\partial \theta^2} > 0 \quad \text{at} \quad \theta = \theta_0, \tag{2.37}$$

2. Fracture grows when strain energy density S reaches its critical value S_{cr}:

$$S(\theta = \theta_0) = S_{cr}. \tag{2.38}$$

Plotting the strain energy density at some arbitrary radius r versus the deviation angle θ, figure 2.5 is obtained. Employed values of SIFs are similar to the one used in figure 2.4. For comparison purposes, tangential stress $\sigma_{\theta\theta}$ from figures 2.4 is also present in figures 2.5. It is seen that introduction of $K_{II} \neq 0$ provokes second local minimum. It should be noted that Sih's failure criterion is applicable for ideally brittle materials failing in tension. Thus, the curve minimum, corresponding to the tensional tangential stress, should be chosen.

After comparison of two curves, one can conclude that the direction where strain energy density reaches its local minimum coincides with the direction of local maximum in tangential stress $\sigma_{\theta\theta}$. The failure criterion for mixed I + II mode written in terms of the hoop stresses around the crack tip was proposed by Erdogan and Sih [31]. In their approach, fracture grows in the direction of maximum tangential tensional stress $\sigma_{\theta\theta}$.

2.2.6. Irwin's Correction for Plastic Zone

As was stated previously, the area of the plastic zone around the crack tip can vary. For high yield strength materials, such zone is relatively small and ,therefore, is usually ignored. For materials with low yield strength, plasticity can develop considerably, and principles of elasto-plastic fracture mechanics should be taken into account.

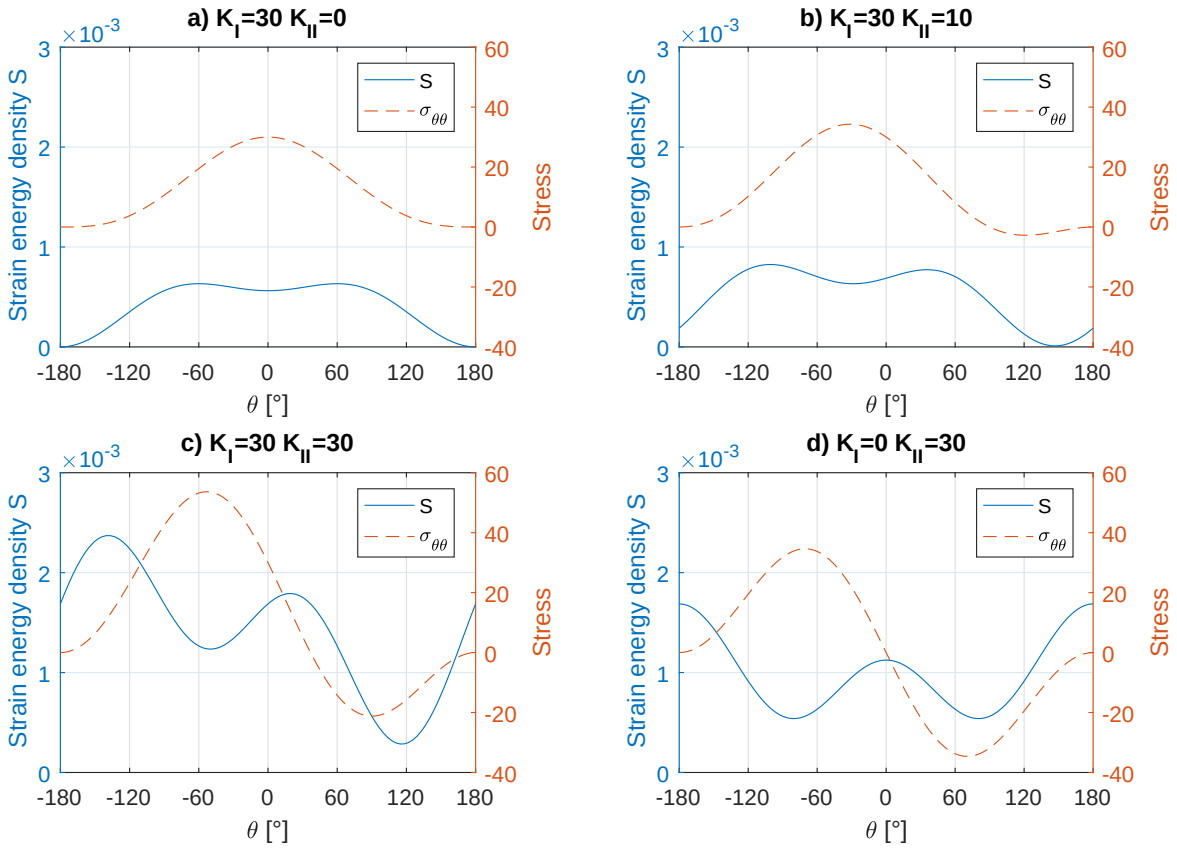

Figure 2.5: Strain energy density around a fracture tip for different combinations of K_I and K_{II}

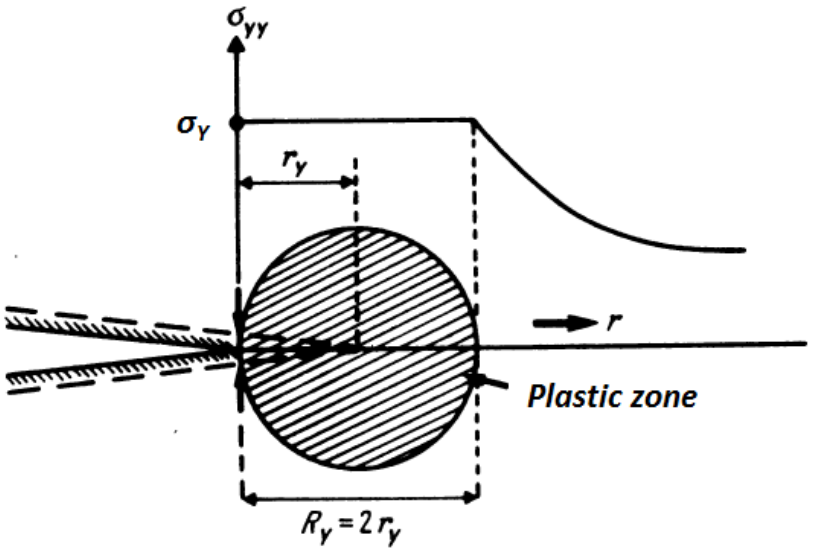

Figure 2.6: Irwin's equivalent crack and plastic zone size (Source: G.Pluvinage. Elasto-plastic mechanics of failure. In translation. Page 33. [86])

Irwin [50] computed the size r_y of the plastic zone by limiting the maximum possible stress to the yield strength σ_Y (see figure 2.6):

$$r_y = \frac{1}{2\pi}\left(\frac{K_I}{\sigma_Y}\right)^2 . \tag{2.39}$$

Artificial restriction of the stresses in the plastic zone up to the material yield strength unbalances the force equilibrium. Balance could be gained again by shifting the stress field on a distance equal to r_y. This leads to a fictitious prolongation of the fracture on the distance equal to the radius of the plastic zone (see the hatched fracture contour in figure 2.6):

$$a_{\text{eff}} = a + r_y = \varphi a , \tag{2.40}$$

where φ is the Irwin's correction factor calculated as:

$$\begin{aligned} \varphi &= 1 + \frac{\sigma^2}{2\sigma_Y^2} \quad \text{(plane stress)}, \\ \varphi &= 1 + \frac{\sigma^2}{18\sigma_Y^2} \quad \text{(plane strain)}. \end{aligned} \tag{2.41}$$

In elasto-plastic fracture mechanics, Irwin's failure criterion 2.24 is transformed into:

$$K \leq K_c^e , \tag{2.42}$$

where K_c^e is the equivalent stress intensity factor, corrected by Irwin's factor φ:

$$K_c^e = K_c\sqrt{\varphi} . \tag{2.43}$$

The drawback of the discussed approach is in its limited applicability. It works well only when the plastic zone size is smaller than the elastic region ahead of the crack. This restriction is removed by introduction of cohesive forces at the crack tip.

2.2.7. Cohesive Zone Theory

Cohesive zone model was developed to take plastic relaxation at the fracture tip into account. Initially, this model was proposed by Barenblatt in 1959 [5] and later by Dugdale in 1960 [27]. It is assumed that the cohesive forces at the tip depend on a distance between atoms. In the ideal crystal, the cohesive forces are null when the inter-atomic distance y equals to the same distance at rest. When the separation δ increases, the cohesive forces σ grow substantially until the distance reaches the value of δ_0 (see figure 2.7a). Further separation of atoms leads to development of unrecoverable damage and reduction of the cohesive forces. After reaching some critical separation δ_{max}, σ vanishes and discontinuity propagates. The whole area under the stress-displacement curve should be equal to the fracture energy G_{Ic}. Similar approach is used in the cohesive element method, where interface elements with pre-defined $\sigma - \delta$ relation are dynamically inserted in-between finite elements in front of the existing fracture tip.

The model of Barenblatt was not based on the pattern of cohesive stresses distribution, but on the absolute value of cohesion modulus C, which is a material constant. C can be simply related to the surface tension γ, Young's modulus E and Poisson's ratio ν:

$$C = \frac{\pi E \gamma}{1 - \nu^2} . \tag{2.44}$$

Barenblatt's propagation criterion states that fracture propagates as soon as the stress intensity factor at the fracture tip K reaches the value of C/π.

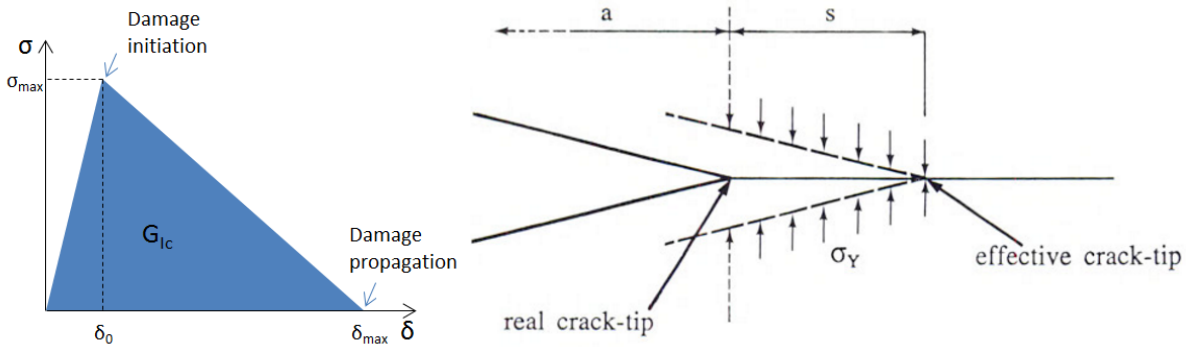

Figure 2.7: Visualization of the cohesive forces theory. (a) Diagram for inter-atomic separation - cohesive forces relation. (b) Dugdale's effective crack and plastic zone size (Source: Aliabadi, M.H. Numerical Fracture Mechanics. Page 35. [2])

Dugdale, in his approach [27], assumed that the cohesive stress is constant along the tip and equals to the yield strength of the material σ_Y. In his approach, the crack artificially extends on a distance s, and the yield stress σ_Y is applied at this extension (see figure 2.7b). Distance s is defined such, that the stress singularity at the tip of the effective fracture disappears, and SIF becomes equal to zero.

Based on the proposed geometry, Dugdale found the expression for the distance s:

$$s = \frac{\pi^2 \sigma^2 a}{8\sigma_Y^2} = \frac{\pi K^2}{8\sigma_Y^2}, \tag{2.45}$$

where σ is the stress applied at infinity.

Based on Dugdale's model, the equation for crack opening δ at the original tip can be derived:

$$\delta = \frac{8a\sigma_Y}{\pi E} \ln\left[\sec\frac{\pi\sigma}{2\sigma_Y}\right]. \tag{2.46}$$

Wells [113] proposed that the process of fracture propagation is controlled by large strains around the fracture. He also suggested that the fracture opening near the tip is the measure of these strains. The critical deformation criterion states that fracture starts growing as soon as its opening δ reaches the critical value δ_c. Translation between critical fracture opening δ_c and energy release rate G_c can be established as follows:

$$\delta_c = \frac{4}{\pi}\frac{G_c}{\sigma_Y}. \tag{2.47}$$

Model of Barenblatt-Dugdale for elasto-plastic deformation permits calculation of following properties: 1) stress distribution around the fracture tip; 2) dimensions of the plastic zone; 3) fracture opening near the tip. Output of such model is more suitable for the experiments than the elastic fracture description, even with Irwin's plasticity correction factor [86].

2.2.8. J-Integral

Due to difficulties in calculation of stresses in close proximity to the crack tip for a nonlinear elastic or elasto-plastic material, an approach based on an integral over the area around the tip was developed. The J-integral is intended to calculate the strain energy release rate for a crack. It is defined as:

$$J = \int_\Gamma \left(W dx - \mathbf{t}\cdot\frac{\partial \mathbf{u}}{dy} dS\right), \tag{2.48}$$

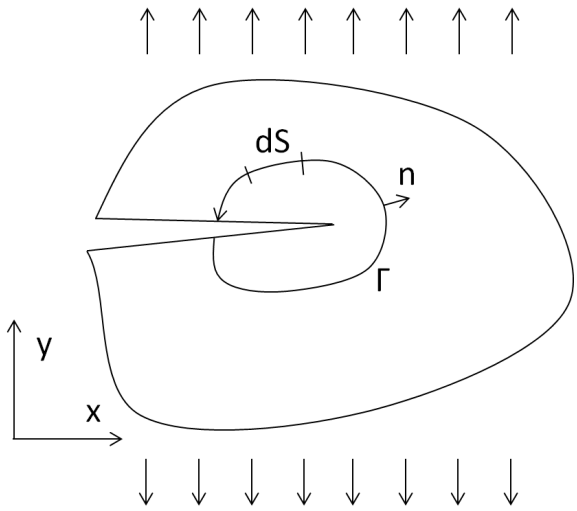

Figure 2.8: Way of calculating the J-integral in a general domain

where $W = \int \sigma_{ij} d\varepsilon_{ij}$ is the strain energy density, $\mathbf{t} = \boldsymbol{\sigma}\mathbf{n}$ is the surface traction vector acting on the contour Γ, $\mathbf{n}$ is the normal to this contour, $\boldsymbol{\sigma}$ is the stress tensor, and $\mathbf{u}$ is the displacement vector. J integral can be thought as the energy flux in the failure zone. Equation for the flux 2.48 was independently developed by Cherepanov [18] and Rice [88]. The line integral is evaluated in a counterclockwise direction starting from the lower crack surface and ending on the upper flat surface (see figure 2.8). For linear and nonlinear elastic materials the J-integral is path Γ independent.

For linear elastic material, J-integral equals to a change of potential energy:

$$J = G = -\frac{\partial \Pi}{\partial l} \,. \tag{2.49}$$

For material with a fracture at rest, change in potential energy equals to zero. The fracture starts growing when J-integral reaches its critical value J_{Ic}:

$$J = J_{Ic} \,, \tag{2.50}$$

which is the J-integral related failure criterion. Parameter J_{Ic} is material specific and independent of load type and geometry.

2.2.9. Fracture Orientation

Fractures tend to grow in the direction perpendicular to the minimum in-situ stress. However, the orientation of the principal planes near the borehole can differ from orientation in the far-field. In practice, fracture initiates in the plane along the wellbore, and as it propagates, it re-orients itself to unaltered in-situ stress. The latter direction would normally coincide with the direction of natural fractures, formed by current stress state. The difference in directions of natural and induced fractures is easily distinguished at the wellbore images (see figure 2.9). Orientation of the induced and natural fractures is used to determine the principal stresses direction.

Series of the lab experiments on hydraulic fracturing [1, 30, 42] gives insight into the nature of turning fractures. Turning, or nonplanar fractures, typically have wall waviness or roughness along the surface within the reorientation plane [1] (see figure 2.10a).

Daneshy [21] demonstrated that the wall waviness and existence of the steps on a fracture face is a proof of the mixed mode of failure, due to tension and shear.

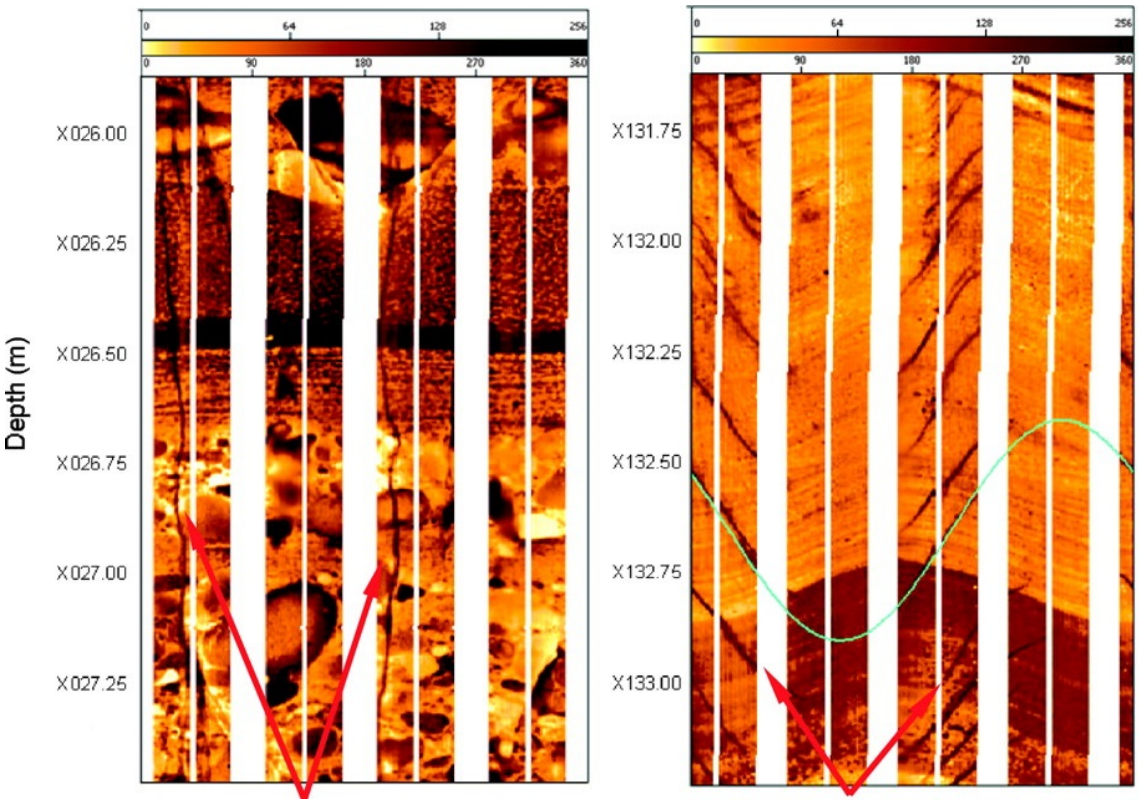

Figure 2.9: Wellbore images of Yufutsu field well in Japan. (a) Example of drilling-induced fracture developed in a subvertical well and (b) drilling-enhanced natural fractures developed within the tensile region of the wellbore wall. Fractures are indicated with red arrows. Although data was taken from the same field and similar type of wells, direction of natural and induced fractures differ. Source: Barton et al. [8]

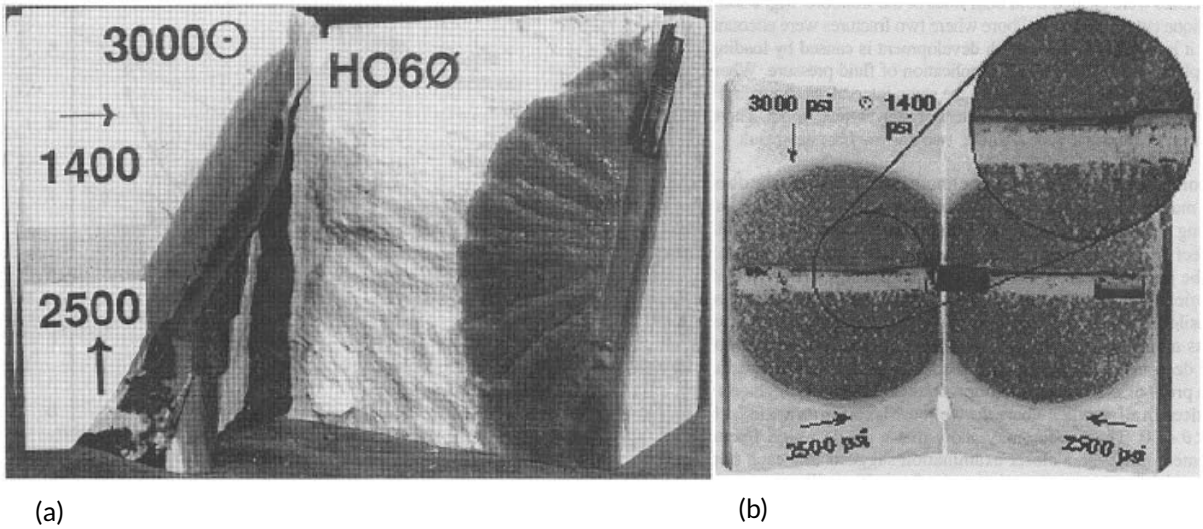

Figure 2.10: Colored fracture in lab specimens sawed in halves. (a) Steps and roughness along a reoriented fracture and (b) smooth single planar fracture. Source: Abass et al. [1]

For vertical wells and horizontal wells drilled towards the maximum horizontal stress, the directions of the minimum horizontal stress in the near-well and far-field zones coincide. As a result, hydraulic fracture is planar. Experiments done by Abass et al. [1] confirm that such a fracture is single and smooth, with full communication with the wellbore (see figure 2.10b).

2.2.10. Adopted Concepts of Fracture Mechanics

Following concepts of fracture mechanics were adapted in the current work:

- Linear Elastic Fracture Mechanics concept. As we are concerned with crack propagation in a brittle rock, plasticity zone, developing around the crack tip, is insignificantly small compared to the rest of the rock which behaves elastically.

- Irwin's criterion for linear elastic failure of mode I $K_{\mathrm{I}} \leq K_{\mathrm{Ic}}$ [50]. Assumption of mode I failure is fair for hydraulic fracturing phenomenon. Application of chosen failure criterion is strictly limited to brittle rock. Different failure criteria should be chosen when ductile material, such as shale, is considered.

- Erdogan and Sih's approach for determination of fracture propagation direction [31]. According to their approach, brittle fracture grows in the direction of the maximum tangential tensional stress $\sigma_{\theta\theta}$. This approach is claimed to be suitable both for mode I and mixed mode fractures in brittle material.

2.3. Numerical Modeling Techniques

In this section, brief review of numerical techniques commonly used for modeling fracture growth is done. Main focus is given to the techniques that permit simulating long fractures on the large reservoir scale.

2.3.1. Finite Element Method

The most common way of modeling fracture growth is by means of Finite Element Method (FEM). The formulation of this technique requires solution of a system of algebraic equations. In the scope of this approach, the whole domain is discretized into finite elements. Unknowns, such as displacements, are defined in elemental vertices. The approximated form of the governing equation is written for each separate cell and then included into a larger system of equations corresponding to the whole geometry.

There are a number of ways of treating fracture in FEM methodology. The most simple approach allows crack to follow the path between neighboring finite elements. Upon opening a new fracture segment, the vertex shared by two elements next to the last fracture segment duplicates. It enables a separation of these elements (see figure 2.11). An advantage of such technique is a constant number of finite elements, although the number of nodes and topology changes.

The weakness of such method is in the fact that the fracture is obliged to follow the path between finite elements which leads to artificial tortuosity of fracture trajectory. It can be avoided by introduction of re-meshing algorithm. In scope of the re-meshing procedure, mesh is rebuilt on each propagation step in such way that the fracture always follows the exact theoretically defined direction. Advantage of the re-meshing is also taken for re-arranging elements with different sizes along the fracture. Having dense mesh closer to the tip helps to reproduce stresses and strains in a more accurate manner, while having larger elements further away helps to save computational time (see figure 2.12).

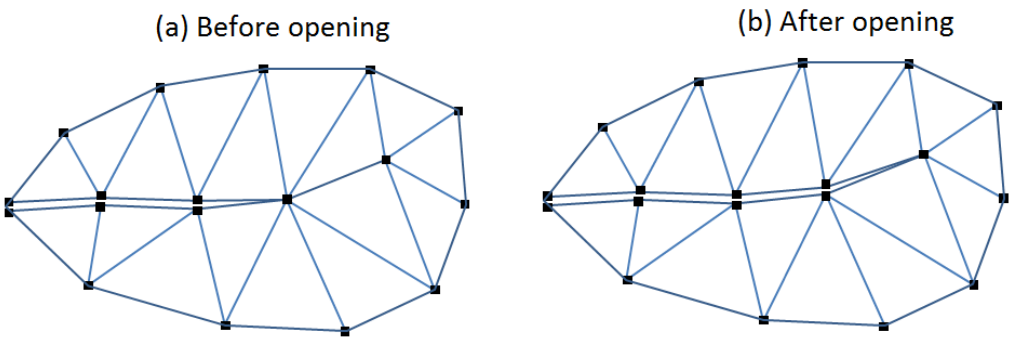

Figure 2.11: 2D illustration of the node duplication upon fracture segment opening

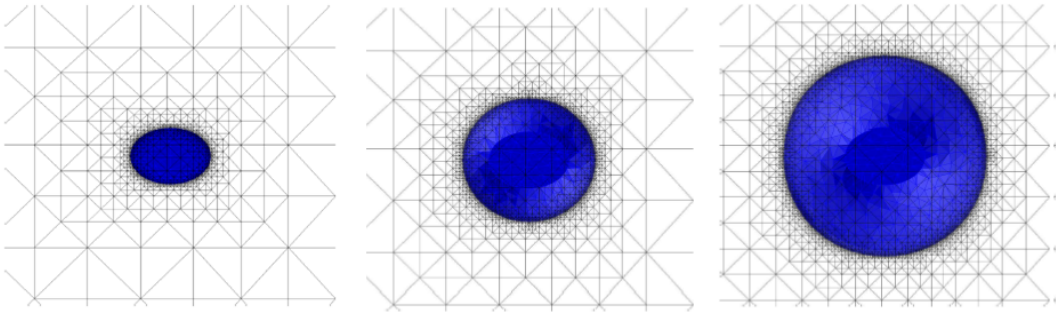

Figure 2.12: Crack growth modeled using re-meshing (Source: Garzon et al., 2010 [35])

2.3.2. Finite Element Method with Contact Plane

A significant drawback of using only finite elements for cracks is the inability to model interaction between two opposite fracture faces when the fractures closes. This problem is solved by introduction of contact surfaces on the fracture segment. It enables having effects of cohesion, friction, and mutual non-penetration as described by Borja [13]. Thus, opening a new fracture segment also causes adding a new contact surface. Mathematically, it leads to addition of a normal and tangent traction components t_N and t_T, and normal and tangent gap components g_N and g_T into numerical scheme (see figure 2.13a). A similar idea of a contact-type fracture growing in-between finite elements was used by Settgast et al. [91] in implementation of GEOS, which is a multi-physics simulator developed at Lawrence Livermore National Laboratory. However, in their approach, a fluid flow is simulated only along the fracture, while the loss of fluid from the main fracture into combination of natural fractures and porous rock material is modeled through a simple sink term. Unlike them, in the current model the fluid flow is modeled across the whole domain, including induced and natural fractures and porous rock. Fluid flow is simulated by means of Discrete Fracture Method. Detailed explanation of the adopted approach is given in chapter 3.

It is important to mention, that positive values of g_N and t_N correspond to fracture "closure": virtual penetration of one fracture face into another. The mechanical behavior of a closed crack can be described through relation between traction forces and gap components as shown by Garipov et al. [33]:

$$\begin{aligned} t_N &= \mathcal{N}(g_N)\,, \\ t_T &= \mathcal{F}(t_N) \quad \text{for} \quad g_t \neq 0 \quad \text{(slip state)}\,, \\ t_T &< \mathcal{F}(t_N) \quad \text{for} \quad g_t = 0 \quad \text{(stick state)}\,, \end{aligned} \tag{2.51}$$

where $\mathcal{F}$ is a friction law and $\mathcal{N}$ is a function describing the relation between normal gap and

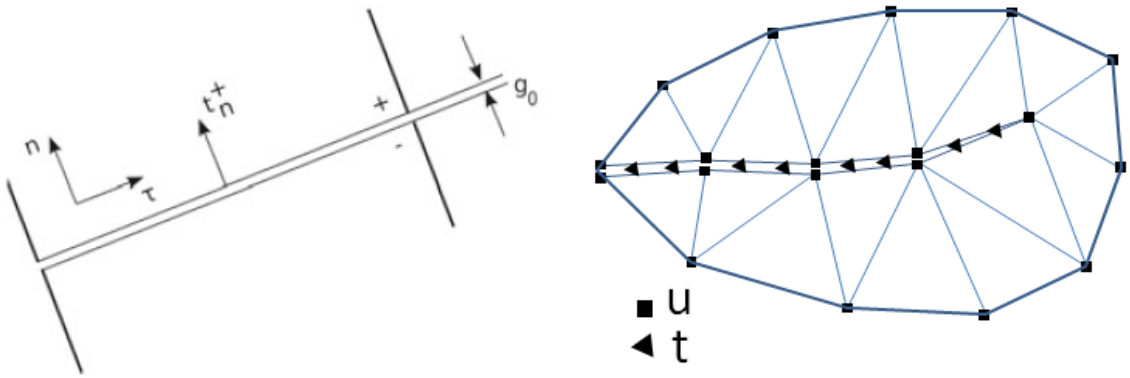

(a) 2D representation of a contact

(b) Model with contacts on fracture

Figure 2.13: Illustration of a contact and its integration into FE model (Source of 2.13a: Garipov et al., 2016 [33])

normal traction.

Advantages of the discussed method are given below:

- No need for remeshing.
- Ease-of-formulation.
- Both open and closed fractures can be modeled

Some disadvantages of this method persist:

- Changing topology.
- Requires conforming mesh.
- Difficulty in determination of principal planes at the fracture tip.

The latter is happening due to difficulty in representing the stress singularity at the tip by common bilinear finite element. That problem is commonly tackled by using the quarter-point elements or elements with enriched strains.

2.3.3. Quarter-Point Element

Barsoum [7] and Henshell and Shaw [45] proposed the use of the quarter-point isoparametric elements in the vicinity of the crack tip to have a good representation of the crack-tip field. Moving the mid-side node towards the crack tip by a quarter size helps to reproduce the $1/\sqrt{r}$ linear-elastic singularity for stresses and strains [40] (see figure 2.14b).

Combining analytic equations for plane strain displacement at quarter point A and vertex B through K_I and solving them for K_I, results in following equation:

$$K_I = \frac{E}{12(1-\nu^2)}\sqrt{\frac{2\pi}{l}}(8v_A - v_B)\,. \tag{2.52}$$

The advantage of such method is no need in explicit extrapolation of the SIF values further than from one element behind the crack tip. Shih [92] showed that numerical K_I values for the double edge crack strip and three point bending specimens to be within 1.2% and 1.1% of analytic values.

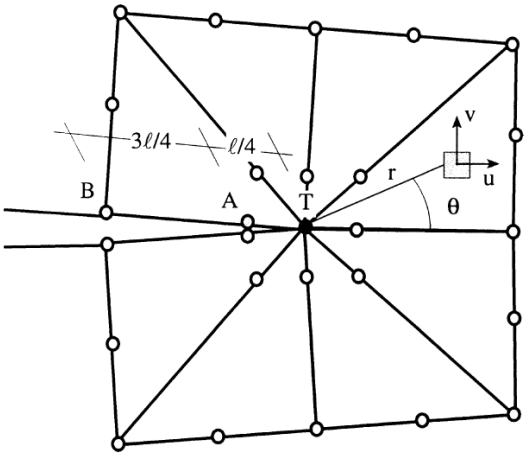

(a) Quarter-point singular elements. Source: Guinea et al., 2000 [40]

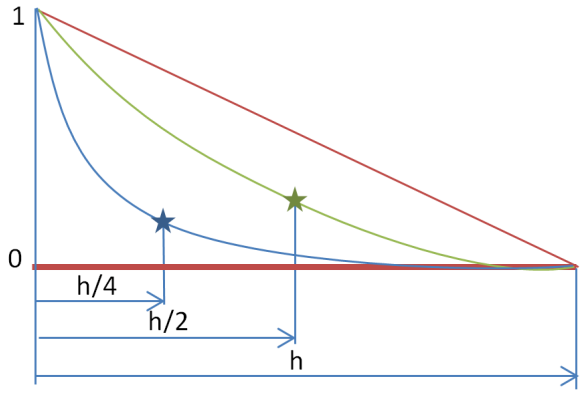

(b) Shape functions for bilinear (red), mid-point (green) and quarter-point elements (blue)

Figure 2.14: Illustration of a quarter-point element

2.3.4. Enriched Element

Another way of retrieving the theoretical stress field around the crack tip is done via element enrichment. The formulation involves incorporation of known beforehand analytic expression for the displacement field into the conventional 4-node (in 2D) finite element approximation for the displacement. Benzley [10] proposed following expression for it:

$$u_i = \sum_{k=1}^{4} N_k u_{ik} + R(a,b)\left[K_I\left(Q_{1i} - \sum_{k=1}^{4} f_k \overline{Q_{1ik}}\right) + K_{II}\left(Q_{2i} - \sum_{k=1}^{4} f_k \overline{Q_{2ik}}\right)\right], \tag{2.53}$$

where

i - 1, 2;

u_i - displacement in the 1 and 2 directions;

K_I, K_{II} - intensities of singular terms;

Q_{li} - specific singular assumptions;

N_k - shape functions;

u_{ik} - displacement in the element's vertices;

$R(a,b)$ - set of functions equal to 1 on boundaries adjacent to "enriched" elements, and 0 on boundaries adjacent to "bilinear" elements;

Q_{lik} - the value of Q_{li} evaluated at node k;

a, b - local coordinates.

Benzley did a series of simulations of a plane strain tensile strip with a side crack and compared them with the reference solutions. Figure 2.15 gives a comparison between finite element solution with the closed form solution for Stress Intensity Factor K_I. Results are in fair agreement with each other.

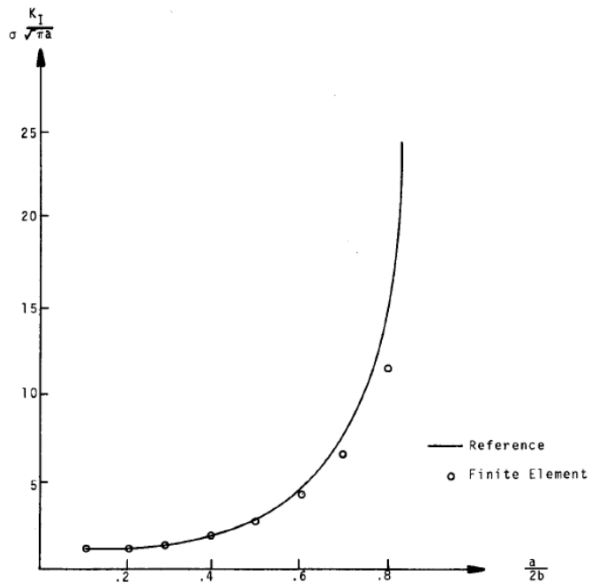

Figure 2.15: SIF as a function of crack length (Source: Benzley, 1974 [10])

2.3.5. Extended Finite Element Method

The idea behind XFEM is the local enrichment of finite elements crossed by a fracture. Fracture path becomes mesh independent. Fracture coming to an element leads to addition of extra degrees of freedom in the vertices and extra term into approximation of displacement function u (see figure 2.16a):

$$u = \underbrace{\sum_{k \subset I} N_k u_k}_{\text{strd. FE approx.}} + \underbrace{\sum_{k \subset I^*} M_{Sk} a_k}_{\text{enrichment}} . \tag{2.54}$$

Here, u is the approximated displacement function, N_k is a standard FE shape function, u_k is the displacement in the node k, I is the set of all nodes in the domain, M_{Sk} is the local enrichment function of node k, a_k is the displacement of the enrichment at node k, I^* is the nodal subset of the enrichment. The enrichment function $M_S(x)$ consists of continuous blending function $f^h(x)$ and discontinuous Heaviside function $H(x)$. Graphic representation of the last two is given in figure 2.16b. Introduction of the jump function M_S into the formulation of the displacement field permits having discontinuity in it.

Following, few advantages of XFEM over standard FEM are given:

- Can have nonconforming mesh.
- Constant topology.
- Mesh independent fracture path.

At the same time, method poses some drawbacks:

- Drastic changes to the FE code:
  - Additional degrees of freedom.
  - Additional Gauss points for integration.
- Computationally expensive.

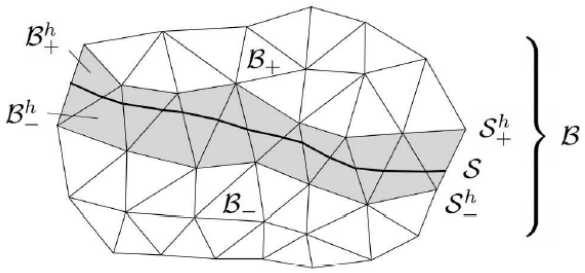

(a) Discontinuity S embedded in a fixed finite element mesh. Shaded region $\mathscr{B}$ is the support of M_S

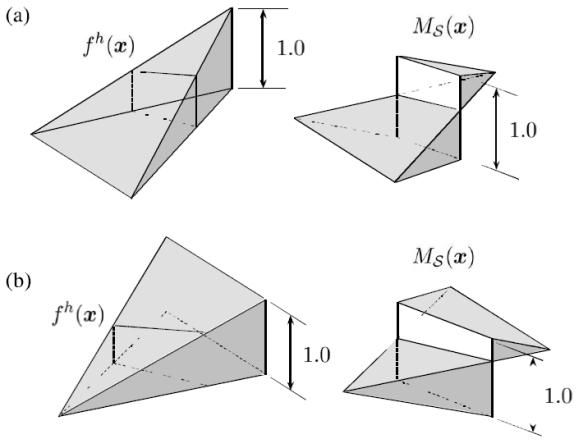

(b) Blending function $f^h(x)$ and jump function $M_S(x)$ for enriched triangular finite elements: (a) one node in $\mathscr{B}_+$; (b) two nodes in $\mathscr{B}_+$

Figure 2.16: Illustration of XFEM method (Source: Borja, R. I. Plasticity, 2013 [13])

2.3.6. Stress Intensity Factor in Finite Element Method Approach

There are three most commonly used approaches for SIFs determination in FEM environment: 1) displacement method, 2) stress method and 3) energy method.

- **Stress method**

  As was previously mentioned in chapter 2.2.1, the analytic solution for stresses around the crack tip is known (see equations 2.21). Inverting it, we can get an expression to estimate the SIF K_I^*:

$$K_I^* = \frac{\sqrt{2\pi r}}{f_{ij}(\theta)}\sigma_{ij}(r,\theta)\,, \tag{2.55}$$

  where

$$\begin{aligned} f_{xx}(\theta) &= \cos(\theta/2)[1-\sin(\theta/2)\sin(3\theta/2)]\,,\\ f_{yy}(\theta) &= \cos(\theta/2)[1+\sin(\theta/2)\sin(3\theta/2)]\,,\\ f_{xy}(\theta) &= \sin(\theta/2)\cos(\theta/2)\cos(3\theta/2)\,. \end{aligned} \tag{2.56}$$

  Similar expression for K_{II}^* can be derived. If exact values of stresses with corresponding distances from the tip r are substituted into equation 2.56, exact value of stress intensity factor K_I is obtained. As a distance from the crack tip becomes smaller, SIF approaches a theoretical value. However, finite element method needs to have infinitely small elements in the crack tip vicinity to be able to reproduce the stress singularity, which is not possible in practice. Therefore, estimation of SIFs from the closest to the tip element would give erroneous number. Chan et al. [17] proposed an K extrapolation technique. They stated that K_I^* curve, obtained from stresses with increasing distance r from the crack tip, rapidly approaches a constant slope. Then they used the intercept of the tangent to the constant slope portion of the curve with the K_I^* axis as the estimate of K_I. The most common choice of the angle θ is 0. Then K_I can be estimated from stress σ_{yy}, and K_{II} from τ_{xy} in the elements laying on continuation of the fracture plane as follows:

$$\begin{aligned} K_I^* &= \sqrt{2\pi r}\sigma_{yy}\,,\\ K_{II}^* &= \sqrt{2\pi r}\tau_{xy}\,. \end{aligned} \tag{2.57}$$

- **Energy method**

  Estimation of the SIFs by energy approach comes from the definition of J-integral (see subsection 2.2.8). Rice [88] showed that for the mixed mode fracture under plane strain condition the following expression holds:

$$J = \frac{1-\nu^2}{E}(K_I^2 + K_{II}^2)\,. \tag{2.58}$$

  Evaluating the J-integral along the contour around the crack tip gives an estimate of K_I and K_{II} separately in case of pure mode I or II, or their combination in case of the mixed mode I+II. Individual estimation of K_I and K_{II} under mixed mode I+II failure is hardly possible.

- **Displacement method**

  Displacement method is similar to the stress method. The analytic expressions for displacement around the tip are derived. Inverting them for K_I yields:

$$K_I^* = \sqrt{\frac{2\pi}{r}}\frac{Gu_i}{f_i(\theta,\nu)}\,, \tag{2.59}$$

  where

$$\begin{aligned} f_1(\theta,\nu) &= \cos(\theta/2)[1-2\nu+\sin^2(\theta/2)]\,,\\ f_2(\theta,\nu) &= \sin(\theta/2)[2-2\nu-\cos^2(\theta/2)]\,, \end{aligned} \tag{2.60}$$

  with $u_1 = u$ and $u_2 = v$ being the horizontal and vertical displacement correspondingly. Above equations are written for plane strain conditions. If analytic values of displacement were substituted in the above equations, exact value of K_I could be obtained. As finite element displacement is inaccurate at an infinitesimal distance from the tip, the extrapolation technique is used. Illustration for the extrapolation method is given in figure 2.17. The average slope of the K_I^* curve is calculated based on the values of displacement of the elements which are sufficiently far from the crack tip to be affected by the stresses distortion. The constant slope line is extended until intersection with the crack tip position. Corresponding value of K_I^* is accepted as K_I.

  Common choice of angle θ for estimation of SIFs is $\theta = \pi$; therefore relative vertical and horizontal displacement v and u are evaluated at the fracture faces :

$$\begin{aligned} K_I^* &= \frac{\sqrt{2\pi}E}{4(1-\nu^2)}\frac{v}{\sqrt{r}}\,,\\ K_{II}^* &= \frac{\sqrt{2\pi}E}{4(1-\nu^2)}\frac{u}{\sqrt{r}}\,. \end{aligned} \tag{2.61}$$

In the developed algorithm, the latter approach is adopted due to its efficiency and computational cheapness. As the displacement data of the fracture segments is already in place, no additional manipulation besides extrapolation is needed.

2.3.7. Adopted Numerical Approach

Based on the techniques discussed above, the developed model was built adapting following approaches:

1. Finite Element Method with contact treatment of fractures. This combination is implemented in geomechanical module of AD-GPRS and has been tested extensively on stationary fractures and faults [33].

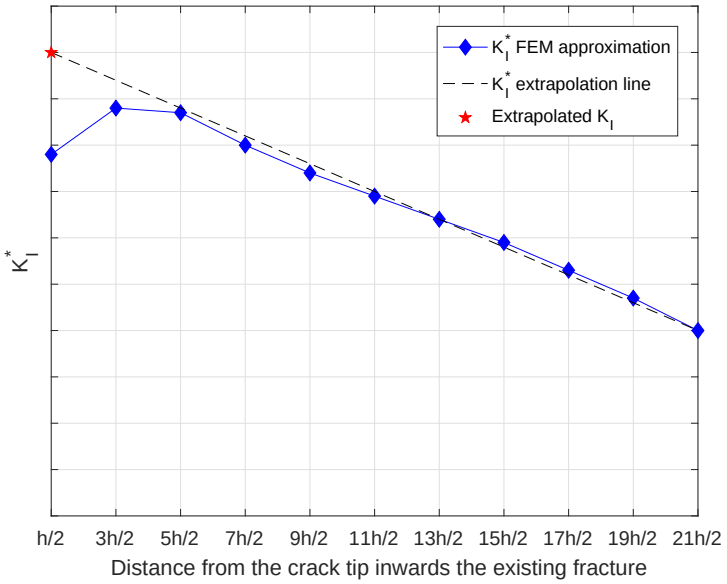

Figure 2.17: Illustration of the displacement extrapolation method. K_I^* are evaluated at the centers of the fracture segments. Left extreme of the plot is the center of the element closest to the crack tip. Distance inward the crack is increasing from left to right.

2. Displacement extrapolation technique for obtaining K values. From FE scheme, displacement field is known. It can be used for evaluation of SIFs.

3

Modeling Methodology

3.1. Discretized Governing Equations

3.1.1. Flow Equation

In this section, the discretization of the flow equation adopted for the model is briefly reviewed. Two-point flux approximation is used in calculation of flow rate between two adjacent volumes:

$$Q_{ij} = \lambda T_{ij}(p_i - p_j)\,, \tag{3.1}$$

where i and j are control volume numbers, p_i and p_j are the pressure values in these volumes, $\lambda = \dfrac{k_f}{\mu_f}$ is the fluid mobility equal, and T_{ij} is the geometric part of transmissibility. The latter is calculated by means of Discrete Fracture Model proposed by Karimi-Fard [56]. T_{ij} is given by:

$$T_{12} = \frac{\alpha_1 \alpha_2}{\alpha_1 + \alpha_2} \quad \text{with} \quad \alpha_i = \frac{A_i k_i}{D_i} \mathbf{n}_i \cdot \mathbf{f}_i\,, \tag{3.2}$$

where A_i is the interface between two Control Volumes (CV), k_i is the permeability of i-th CV, D_i is the distance between the centroid of the interface and the centroid of the CV, $\mathbf{n}_i$ is the unit normal to the surface between two CVs and $\mathbf{f}_i$ is the unit vector along the line connecting the centroid of the interface with the centroid of the CV (see figure 3.1). Definition of the transmissibility between fracture and rock CVs is done in similar way, with only difference that the volumes of two elements can have different magnitudes. The permeability values k of the fracture and the rock may also have large difference.

After integrating the finite-volume approximation of the flux 3.1 into the flow equation 2.3 and using the backward Euler scheme for time, we obtain:

$$\frac{\rho_{fi}^{n+1}\phi_i^{n+1} - \rho_{fi}^{n}\phi_i^{n}}{\Delta t} V_i = \sum_j Q_{ij} + q_i V_i\,, \tag{3.3}$$

where V_i is the volume of the element i, n and $n+1$ are the current and the following moments in time, Δt is the time step size, and j is summed over all adjacent control volumes.

3.1.2. Heat Equation

To model the thermal part, equations 3.1 are modified by changing the fluid mobility λ for thermal conductivity κ and solving for temperatures T instead of pressures p. It yields expression for the heat flux by conduction:

$$\Phi_{ij} = \kappa T_{ij}(T_i - T_j)\,, \tag{3.4}$$

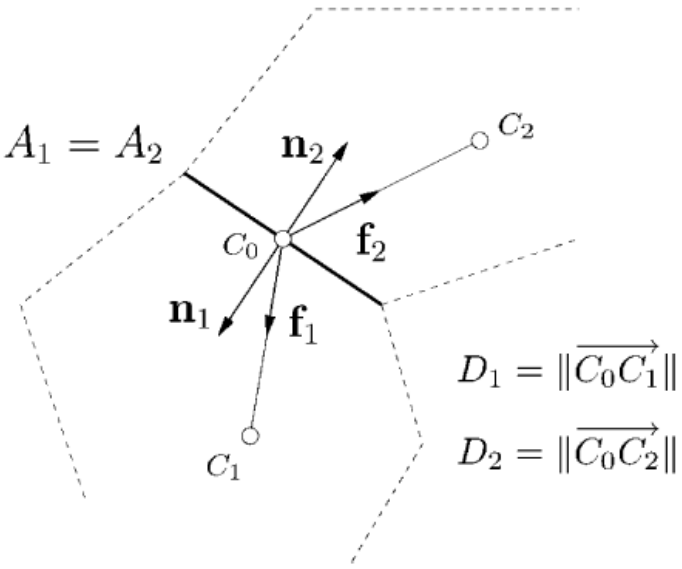

Figure 3.1: 2D illustration of two point flux approximation

where T_{ij} is the transmissibility defined previously. Discretized heat equation is similar to the flow equation 3.3:

$$\frac{\rho_{fi}^{n+1}\phi_i^{n+1} - \rho_{fi}^{n}\phi_i^{n}}{\Delta t} V_i = \sum_j \Phi_{ij} + q_i V_i \,. \tag{3.5}$$

3.1.3. Poro-Elasitcy Equation

The solution of the poro-elasticity equation is done by minimization of the potential energy Π as proposed by Wriggers and Zavarise [115]. It is done by equating the first variation of potential energy to zero:

$$\delta\Pi = \int_\Omega \delta\boldsymbol{\epsilon} : \boldsymbol{\sigma}\, d\Omega - \int_\Omega \delta\mathbf{u}\rho\mathbf{g}\, d\Omega - \int_\Gamma \delta\mathbf{u}\bar{\mathbf{t}}\, d\Gamma - \int_{\Gamma_f} \delta g_N p\, d\Gamma_f - \int_{\Gamma_f} (\delta g_N t_N + \delta g_T t_T)\, d\Gamma_f = 0 \,. \tag{3.6}$$

Here, $\boldsymbol{\epsilon}$ and $\boldsymbol{\sigma}$ are strain and stress tensors in the unfractured body domain Ω, $\mathbf{u}$ is the displacement, $\mathbf{g}$ is the gravity vector, $\bar{\mathbf{t}}_N$ and $\bar{\mathbf{t}}_T$ are normal and tangential components of a traction force $\mathbf{t}$ acting on a crack (same as internal boundary Γ_f), g_N and g_T are the normal and tangential openings of a fracture, p is the pressure inside a fracture, $\bar{\mathbf{t}}$ is the traction acting on external boundary Γ.

It is important to mention that the latter term in the equation 3.6 is present only when fracture is closed, and two surfaces are in contact and push onto each other with t_N and t_T. As soon as the fracture opens and two surfaces separate, term $\int_{\Gamma_f} (\delta g_N t_N + \delta g_T t_T)\, d\Gamma_f$ vanishes. Then, the only force acting on the internal boundary Γ_f is the pressure p inside the term $\int_{\Gamma_f} \delta g_N p\, d\Gamma_f$. Value of normal gap component g_N is positive for situations when surfaces penetrate into each other. Negative values of g_N correspond to the fracture opening.

Nodal-based finite-element approximation used for displacements $\mathbf{u}$:

$$\mathbf{u}(\xi) \approx \sum_a N_a(\xi)\mathbf{u}_a \,, \tag{3.7}$$

where $\mathbf{u}_a$ is the vector of nodal displacements and N_a are shape functions. Gap function g is

approximated in a similar manner:

$$g(\xi) \approx \sum_a N_a(\xi) g_a \,, \tag{3.8}$$

where g_a are the gap function values in the contact surface integration points.

Traction t_N and t_T in equation 3.6 are treated by means of Kuhn-Tucker conditions for Coulomb friction [95]:

$$\begin{aligned} t_N \geq 0, \quad g_N \geq 0, \quad t_N \cdot g_N = 0 \,, \\ \Phi = |t_T| - \mu t_N \leq 0 \,, \\ \dot{\mathbf{g}}_T = \xi \frac{\partial}{\partial t_T} \Phi \,, \\ \xi \geq 0 \,, \\ \xi \Phi = 0 \,. \end{aligned} \tag{3.9}$$

Here, μ is the friction coefficient, Φ is the yield function, which can have only negative or zero value. First equation states that normal opening can happen only when having zero normal traction t_N. The third and forth equations postulate that slip occurs only in the direction opposite to applied tangential traction. The last equation enforces the condition that slip can occur only when $\Phi = 0$. When $|t_T| \leq \mu t_N$, perfect stick occurs and $\dot{\mathbf{g}}_T = 0$.

The method used to impose the contact and stick/slip conditions is penalty method. Previous equations are replaced with:

$$\begin{aligned} t_N = \varepsilon_N g_N \,, \\ \dot{\mathbf{g}}_T - \xi \frac{\partial}{\partial \mathbf{t}_T} \Phi = \frac{1}{\varepsilon_T} \dot{t}_T \,, \\ \xi \geq 0, \quad \Phi \leq 0, \quad \xi \Phi = 0 \,, \end{aligned} \tag{3.10}$$

where ε_N and ε_T are penalty parameters.

When "slip" occurs, the traction vector is evaluated by return mapping algorithm [95]:

$$\begin{aligned} t_N^{n+1} = \mu g_N \,, \\ t_T^{\text{trial}} = t_T^n + \varepsilon_T (g_T^{n+1} - g_T^n) \,, \\ \Phi^{\text{trial}} = |t_T^{\text{trial}}| - \mu t_N^{n+1} \,, \\ t_T^{n+1} = t_T^{\text{trial}} \quad \text{if} \quad \Phi^{\text{trial}} \leq 0 \,, \\ t_T^{n+1} = \mu t_N^{n+1} \quad \text{if} \quad \Phi^{\text{trial}} \geq 0 \,. \end{aligned} \tag{3.11}$$

Although in the developed model, we deal with mode I fractures, where sliding is not a common phenomenon, having the return mapping algorithm enables modeling both hydrofractures and pre-existing natural fractures and faults.

3.2. Domain Discretization

In the current section, description of modification to the meshing and solving technique for a stationary fractures is given. This modification comprises a core of the proposed approach.

The flow equations are solved by finite volume technique, and the mechanics equations are solved by finite element method implicitly. Both methods of solution share the same computational grid. Smoothness of a fracture path is achieved by using an unstructured grid. Although the reservoir simulator handles 3D formulation, the model was developed for 2D case by assigning the third dimension equal to unity. A 2D illustration of the grid type can be seen in figure 3.2b, while actual grid used for simulations is given in figure 3.4c.

Figure 3.2a shows the physical domain with the curved fracture in it. Figure 3.2b shows the discretized domain and the mesh that later would be used by flow and mechanics module in different ways. The geomechanical grid and associated unknowns are shown in figure 3.2c. Non-fractured domain consists of finite elements with displacements u defined in their vertices. Fracture, in its turn, is modeled as a contact surface between two finite elements. Each fracture surface has associated traction vectors t, whose locations coincide with the Gauss integration points. Different nodes are used to represent the displacements on each side of a single fracture surface. Upon activation of a next fracture segment, nodes at the open side of this segment duplicate, which makes the separation of two neighboring finite elements possible (see figure 2.11).

The flow grid, shown in figure 3.2d, is produced as a modification of a typical flow grid for Discrete Fracture Model (DFM) [56]. In DFM, continuous rock is discretized by finite volumes with the pressure p, density ρ_f and viscosity μ_f defined in cell centers. Each fracture segment has assigned a finite volume with corresponding unknowns. In my approach, a fracture propagates along the boundaries of the FEs/FVs. These boundaries are named the "virtual" fracture segments. The classical DFM scheme is modified in such a way that all these boundaries are assigned additional finite volumes from the beginning. By doing so, a single discretized domain is prepared for any possible fracture geometry. Volumes of these "virtual" segments are kept smaller than the non-fractured rock finite volumes. Reason for adding all the finite volumes from the beginning and not doing it dynamically is sensitivity of the DFM to volume changes. A sudden increase in total system volume can easily destabilize numerical scheme for flow. Adding the finite volumes in one step increases the computational as extra unknowns are added to the system of equations. That is the main "price" of the current fracture model payed for no need in re-meshing. Improvement of the finite volume generation scheme should be treated as one of the main priorities in further development of this model. Advantage of such approach is a constant size of the system of equations for flow and no need in its re-assembly after each fracture segment opening or closing.

When a failure criterion is satisfied, fracture propagates one element further from its tip. In mechanical grid, it leads to addition of a contact surface with associated traction vectors. The flow grid is not affected by opening or closing of this segment as it already has finite volumes assigned at every possible position. The permeability of the "activated" finite volume changes from some small value, corresponding to non-fractured rock, to much higher value, for fracture. The latter leads to an update of the transmissibilities around the tip. Any analytic function describing the fracture conductivity could be employed in the model.

3.3. Fracture Opening Algorithm

Fracture opening algorithm is designed to open or close fracture segments on each Newton iteration. The flow chart with this algorithm is given in figure 3.3.

Fracture segments can have three types of activity markers. Marker $\mathbf{0}$ is assigned to non-active fracture segments and corresponds to non-fractured rock. Fracture segments activated during current time step get marker $\mathbf{1}$. Initially, all non-active "virtual" segments have the marker $\mathbf{0}$. Segments of pre-existing fracture have marker $\mathbf{2}$. When fracture append any non-active segment, its marker is updated from $\mathbf{0}$ to $\mathbf{1}$. A segment can be erroneously activated during a Newton iteration. The reason for this could be an overshoot in the pressure. If that happens, in one of the following Newton iterations pressure solution retracts. As a consequence, marker of an erroneously activated segment is also retracted from $\mathbf{1}$ to $\mathbf{0}$. As a result, the fracture can both extend and shorten during one time step. When the solution at the end of a time step converges, all markers $\mathbf{1}$ are updated to $\mathbf{2}$, which means that the fracture can not be shortened anymore.

Apart from markers, active segments (segments with markers $\mathbf{1}$ and $\mathbf{2}$) have also mechanical

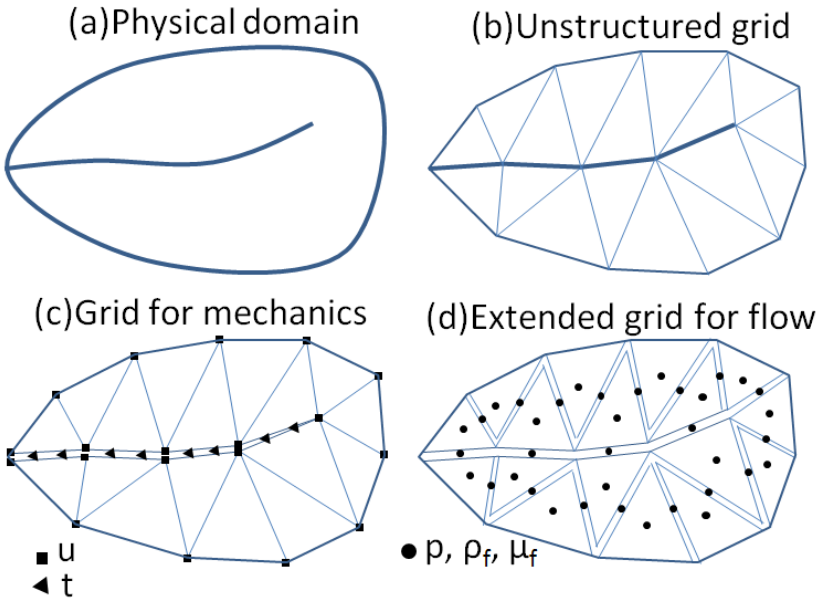

Figure 3.2: Illustration of a grid structure

statuses. Again, three mechanical statuses are possible. Status **2** belongs to an open fracture, faces of which are not in contact. Status **1** corresponds to two surfaces that are in contact and slide along each other (so called "slip" condition). Status **0** is assigned to two surfaces in contact which are stick to each other.

Convergence of Newton iteration is checked separately versus following norms: l^∞-norm for the pressure and temperature, and l^2-norm for mechanics. Based on the stress field from each Newton iteration, decision is made whether to activate a new segment or not. If failure criterion is satisfied, one more segment is added, which triggers update of conductivity and associated transmissibilites values. In mechanical scheme, it leads to renumbering of nodes and addition of new variables g_N and g_T. In the next Newton iteration, updated scheme is solved. Correctness of a segment activation during previous iteration is evaluated in current iteration and is based on the mechanical statuses of a segment. If recently activated segment with marker **1** has mechanical status **2**, then solution is correct. In contrast, if an activated segment is mechanically closed (status **0** or **1**), then the previous solution was wrong and this segment is deactivated. Conductivity and associated transmissibilities of this segment are also retracted.

3.4. Model Geometry, Boundary and Initial Conditions

Reservoir is modeled as the 3D plate with unity thickness which is treated as 2D. As the problem is symmetric with respect to a plane perpendicular to the fracture and originating in its center, only half-space is modeled. The size of the model is chosen to be 300 m in Y direction and 150 m in X direction. Fracture starts at the center of the left edge. Pre-existing crack has a length of 5 m.

Boundary condition for the flow problem is no flow through the left edge and constant pressure at the certain radius from the fracture center ($r = 100$ m). Reason for having an aquifer at the circular boundary is replication of the analytic solution assumptions, namely radially moving pressure penetration front. The reason for keeping the flow boundary far from the mechanical boundary is to reduce the effect of pressure change on the stresses. At the center of the pre-existing fracture, water is injected with a constant flow rate. Illustration of the domain size and boundary conditions for the flow problem can be seen in figure 3.4a. Initial conditions for the

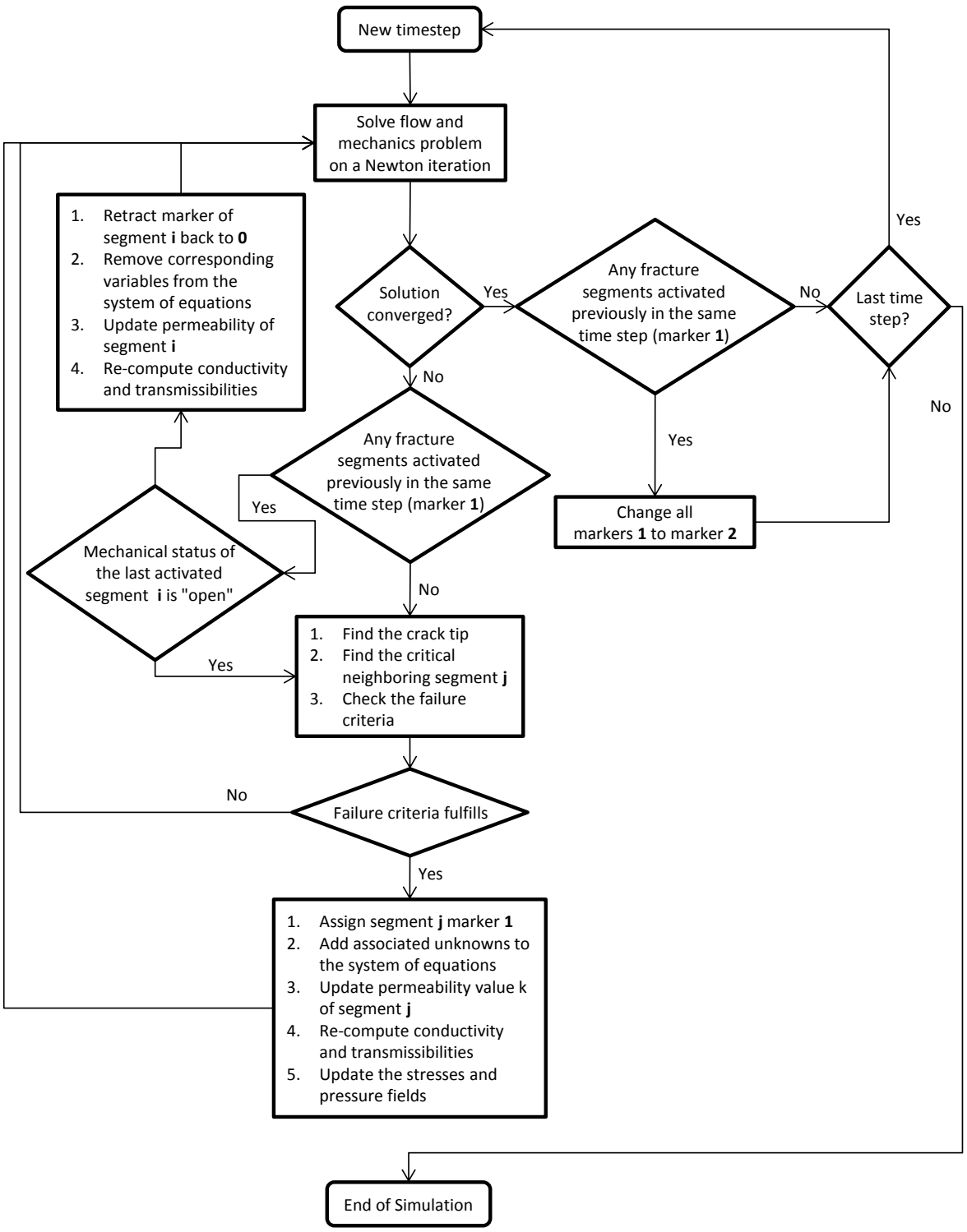

Figure 3.3: Algorithm of fracture propagation

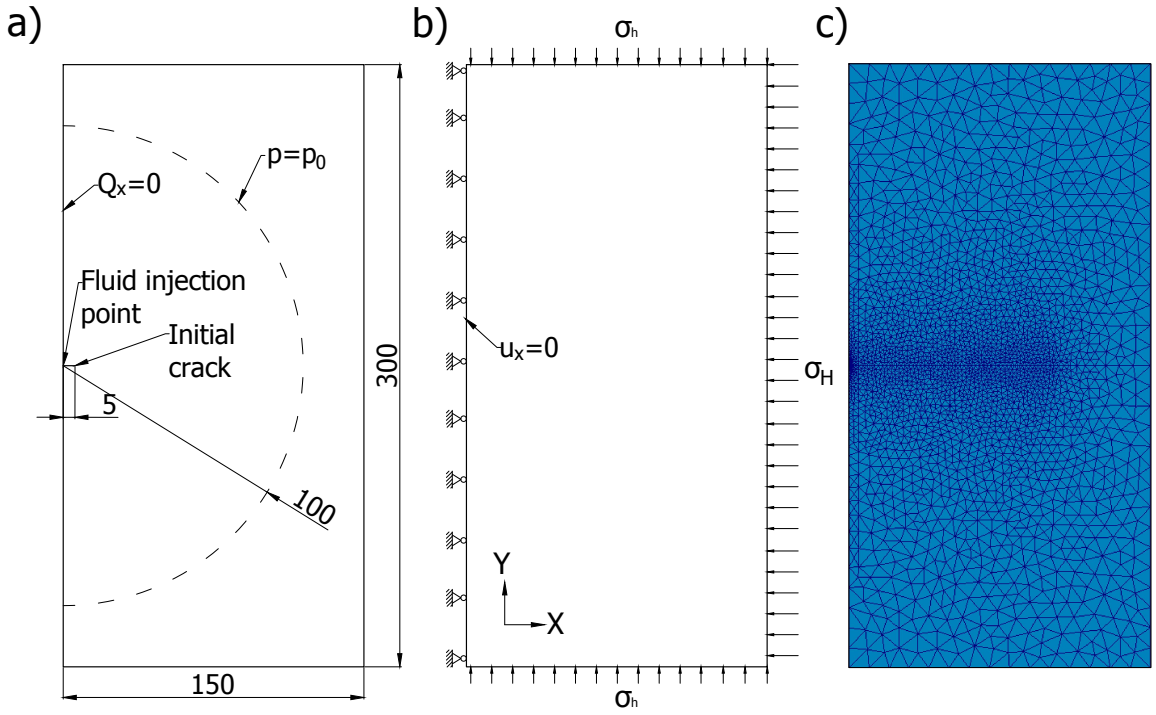

Figure 3.4: Model dimensions and boundary conditions for a) flow and b) mechanics problems; (c) employed unstructured grid.

flow problem is constant reservoir pressure p_{res} across the whole domain.

Mechanical problem has the following settings. Stress field is created by applying the normal stresses on 3 domain sides: the upper and lower boundaries have minimum horizontal stress σ_h, and the right boundary has maximum horizontal stress σ_H. Symmetry condition for mechanics is provided by fixing zero displacements in X direction on the left side. The two planes bounding domain in Z direction have zero displacements out of plane, which replicates the plane strain condition. Schematic view on mechanical boundary conditions is given in figure 3.4b. Initial conditions for the mechanical problem is the anisotropic stress state conforming the boundary conditions.

Geometry and mesh are built by means of free-ware 3D grid generator GMSH [37]. Unstructured grid employed both in the flow and mechanics calculations is given in figure 3.4c. The discretization data together with the rock properties are converted into AD-GPRS input files.

3.5. Semi-Analytical Solution

For validation of developed model, following semi-analytic solution for fracture length is employed. It consists of solution for pressure, stresses and well-known fracture propagation criteria. Semi-analytic solution for the pressure distribution was developed by Koning [63] in his doctoral thesis. He employed the elliptical coordinate system:

$$\begin{aligned} x &= L\cosh\xi\cos\eta\,, \\ x &= L\sinh\xi\sin\eta\,, \end{aligned} \tag{3.12}$$

where L is the fracture length, ξ is the ellipse number starting from the smallest, and η is the direction angle. Further, he used solution for the steady-state pressure profile surrounding an infinite conductivity fracture derived by Muskat [76]:

$$\Delta p(\xi) = \frac{q\mu}{2\pi kh} \ln\left(\frac{a_e + b_e}{L\cosh\xi + L\sinh\xi}\right) = \frac{q\mu}{2\pi kh} \ln\left(\frac{a_e + b_e}{L} - \xi\right), \tag{3.13}$$

where q is the injection flow, μ is the fluid viscosity, k is the rock permeability, h is the fracture thickness, a_e and b_e are the semi-axises of an area influenced by the change in pressure. He assumed that the pressure penetration front moves radially outward with respect to the slowly growing fracture. That allowed him to define an effective time-dependent exterior radius as follows:

$$R_e(t) = 1.5\sqrt{\eta t}\,, \tag{3.14}$$

where η is the fluid diffusivity. After substituting equation 3.14 into 3.13, he obtained the following equation for pressure distribution at late-time regimes:

$$\Delta p(\xi) = \frac{Q\mu}{2\pi kh} \ln\left(\frac{3\sqrt{\eta t}}{L\cosh\xi + L\sinh\xi}\right). \tag{3.15}$$

Koning modified this equation to account for different fluid properties in three domains surrounding the fracture: 1) cold water zone, 2) warm water zone, and 3) oil zone. Expression for the pressure distribution only in the near-fracture (cold water) zone is given. Other 2 expressions are omitted due to their extensiveness:

$$p(\xi, t) = p_R + \frac{Q\mu}{2\pi kh}\left[\frac{1}{\lambda_c}\left(\ln\frac{a_c + b_c}{L} - \xi\right) + \frac{1}{\lambda_w}\ln\frac{a_w + b_w}{a_c + b_c} + \frac{1}{\lambda_{oil}}\ln\frac{3\sqrt{\eta_{oil}t}}{a_w + b_w}\right], \tag{3.16}$$

where $\lambda_c, \lambda_w, \lambda_{oil}$ are the fluid mobilities for cold, warm and oil zones, a_i and b_i with $i = c, w, \text{oil}$ are the major and the minor semi-axises of these zones.

For this solution to be valid, fracture growth should be slow enough, so the pressure penetration front would develop radially. Otherwise, equation 3.14 does not hold. Keeping the reservoir and fluid parameters constant, main parameter that affects fracture growth speed is the injection rate. Keeping Q in certain range assures that the pressure front distribution is radial. Koning defined the range of validity for pseudo-radial solution by condition $q_D < 0.61$, where dimensionless quantity q_D equals to $\frac{Q\mu}{2\pi kh\Delta p}$. Increasing the q_D above this quantity leads to pressure front shape elongating towards the fracture direction and becoming elliptical. At this stage, the best approximation of the flow can be given by the elliptical solution. At values of $q_D > 4.5$, ratio between the pressure penetration depth and the fracture length becomes too small, and the pressure front is propagating parallel to the fracture face. This phenomenon is better approximated by one-dimensional leak-off. In the two latter cases, assumption of pseudo-radial flow is no longer valid; simulation results are compared with radial solution in its range of validity.

Simple analytic solution for the stress intensity factor from stresses in the infinity was used. It was rewritten in terms of pressures and stresses in the rock:

$$p_f - \sigma_0 - \Delta\sigma_P - \Delta\sigma_T = \frac{K_{Ic}}{\sqrt{\pi L}}\,, \tag{3.17}$$

where p_f is the pressure inside the fracture, σ_0 is the far-field total stress perpendicular to the fracture face, $\Delta\sigma_P$ and $\Delta\sigma_T$ are the poro- and thermo-elastic backstresses on the fracture face caused by pressure and temperature changes in the vicinity of the fracture. Koning derived analytic solutions for the poro-elastic backstress which for 2D case is:

$$\Delta\sigma_P = \frac{1}{2}A_p[p(\xi = 0) - p_R] - A_p\frac{Q}{4\pi h}\frac{1}{\lambda_c}\left[\frac{b_c}{a_c + b_c} + \frac{\lambda_c}{\lambda_w}\left(\frac{b_w}{a_w + b_w} - \frac{b_c}{a_c + b_c}\right) + \frac{\lambda_c}{\lambda_{oil}}\left(\frac{1}{2} - \frac{b_f}{a_f + b_f}\right)\right], \tag{3.18}$$

where A_p is the poro-elastic constant, related to Biot coefficient a through $A_p = \frac{1-2\nu}{1-\nu} a$.

Expression for the thermo-elastic backstress is based on research of Perkins and Gonzalez [83], who proposed an empirical fit to numerical simulations:

$$\Delta\sigma_T = A_T(T_c - T_{oil}) \left[\frac{b_c}{a_c + b_c} + \frac{a_c}{a_c + b_c} \cdot \frac{1}{1 + 1/2 \cdot [1.45(h/2b_c)^{0.9} + 0.35(h/2b_c)^2][1 + (b_c/a_c)^{0.774}]} \right], \tag{3.19}$$

where A_T is the thermo-elastic constant, related to the linear thermal expansion coefficient a_T through $A_T = Ea_T/(1-\nu)$. Equation 3.19 is based on the assumption of elliptic shape of the fracture cross-section. Adopting this assumption for the 2D scenario, fracture height h is taken equal to infinity. That makes the second term in the brackets vanish. When obtaining the equation 3.19, authors ignored heat conduction, making heat convection the only energy flow mechanism. Equations 3.17 with 3.16, 3.18, and 3.19 form set of semi-analytic equations used for benchmarking of the developed numerical model.

As the described semi-analytic solution holds only for later times, for early times Mathieu functions are used: analytic expressions, employed in the solution of the diffusivity equation in elliptical systems. In petroleum industry, these functions are applied in Pressure Transient Analysis [PTA] around hydraulically fractured wells. Van den Hoek [104] extended previous work on Mathieu functions for PTA and presented exact solution of the transient pressure around a hydraulic fracture, for both finite and infinite conductivity fractures. These results, expressed in dimensionless time t_D and pressure p_D, are used for comparison with simulated results. Dimensionless time is calculated as $t_D = \frac{k}{\phi\mu C_{tot}} \frac{t}{L^2}$ and pressure as $p_D = p\frac{2\pi kH}{\mu Q}$.

4

Model Validation and Testing

In order to validate the developed model, several benchmarking tests were conducted. Analysis of the pressure field around a stationary fracture and comparison with semi-analytic solution are given first. Further, a single propagating fracture is modeled. Its growth is compared with the semi-analytic solution. Such numerical experiments are conducted for the conditions of a single- and multi-phase flow as well as for conditions of different temperatures of injected fluid and reservoir rock.

4.1. Single-phase Fluid Injection

4.1.1. Stationary Fracture

In the first experiment, injection of the single-phase fluid into stationary fracture is modeled. Properties of the rock, fluid and fracture used in current simulation are given in table 4.1. Temperature values of the injected and stored fluid are equal, and therefore, the problem becomes isothermal. Obtained pressure and stress profiles are shown in figure 4.1).

The fracture has infinite permeability and pressure instantly builds up along its full length. The rock permeability is some finite number, and we see the gradual pressure reduction from $346 \cdot 10^5$ Pa down to $180 \cdot 10^5$ Pa (see figure 4.1a).

Solutions for the stress field (figure 4.1b and 4.1c) shows high tensional stresses in front of the crack tip which is in agreement with the analytic solution (see subsection 2.2.1). Far field pressure and stresses are kept constant.

Dynamics of the pressure development inside the stationary fracture is presented in figure 4.2. Simulated results make a close fit to the Koning's solution. The pressure values are normalized over the initial reservoir pressure to make it dimensionless. In the early-time stage, there is a separation between pseudo-radial solution and numerical results, which disappears at $t < 5 \cdot 10^{-4}$ day. The reason behind is the limited range of validity of the pseudo-radial solution. For verification of early-time results, Mathieu functions are used [104]. In the second stage ($5 \cdot 10^{-4} < t < 6 \cdot 10^{-2}$ days), we observe a logarithmic growth of simulated pressure up to $1.93 P_{res}$, after which its value stabilizes. The second, logarithmic, stage is characterized by the radial seepage from the fracture. There is a perfect match between numerical results and pseudo-radial analytic solution. The breaking point of numerical pressure curve is caused by the pressure front reaching the radially placed aquifers, which is the upper range of validity for the analytic expression.

Benchmarking of the numerical solution in the early-time stage is done via comparison with the analytic solution by Mathieu function (see figure 4.2b). In this graph, pressure is normalized over parameters of the fluid, rock, reservoir, and flow rate. Time, in its turn, is also normal-

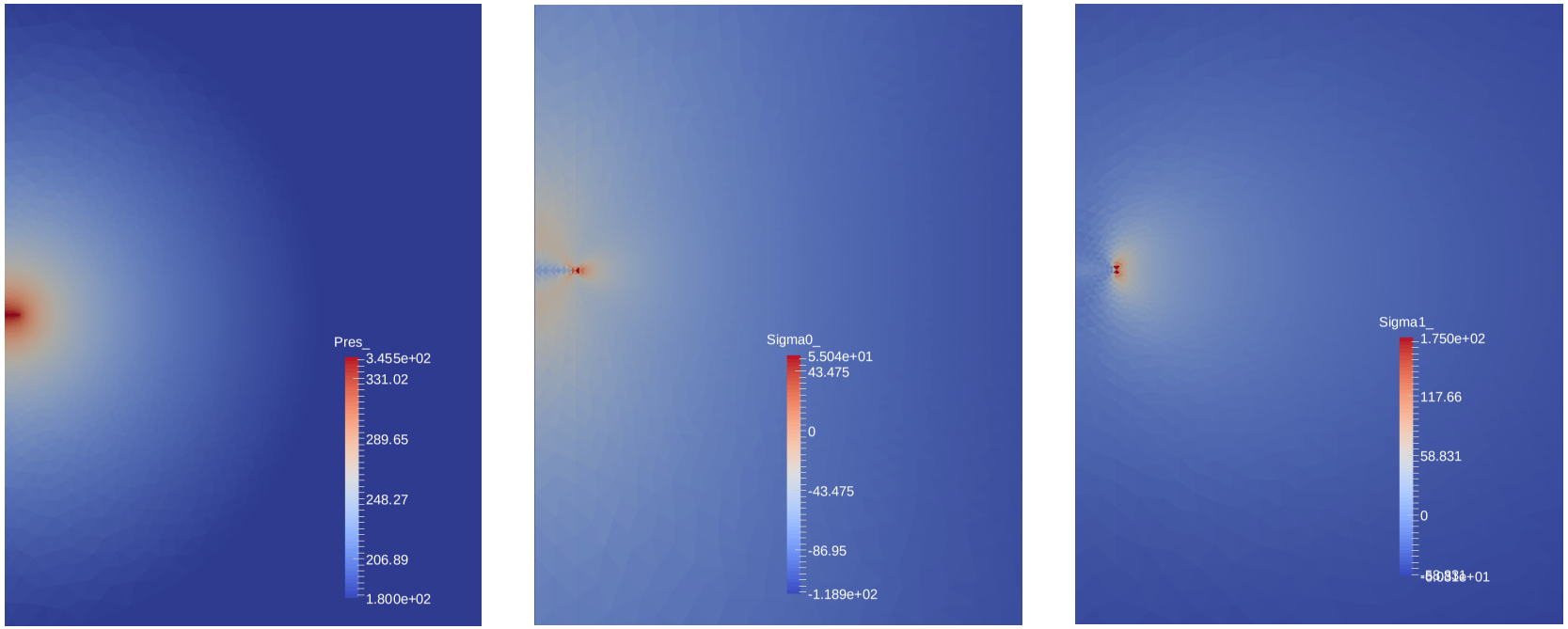

(a) Pressure field (b) Stress σ'_x field (zoomed in) (c) Stress σ'_y field (zoomed in)

Figure 4.1: Simulation results of a non-propagating fracture

Table 4.1: Fluid and rock properties used in the single-phase simulation

Rock properties and stresses	
Matrix porosity ϕ	0.3
Matrix permeability k, mD	250
Fracture conductivity c_{fr}	∞
Density ρ_r, kg/m^3	2500
Biot modulus α	1
Young's modulus E, Pa	$5 \cdot 10^{10}$
Initial reservoir pressure p_r, Pa	$180 \cdot 10^5$
Poisson's ratio ν	0.25
Compressibility C_r, 1/Pa	0
Cohesion c, Pa	$1 \cdot 10^{10}$
Friction angle φ, °	0
Dilation angle ψ, °	0
Total horizontal stress σ_x, Pa	$-300 \cdot 10^5$
Total horizontal stress σ_y, Pa	$-250 \cdot 10^5$
Fluid properties	
Density ρ_f, kg/m^3	1000
Viscosity μ_f, cP	1
Compressibility C_f, 1/Pa	$1 \cdot 10^{-10}$
Injection rate (into half-fracture) Q, m^3/day	30

ized over similar parameters plus the fracture length. There is a close agreement between two curves in the transient regime period ($t_D < 1$)) which indicates correctness of numerical solution for transient flow regime. The reason of separation between two curves in later times is due to the fact that the analytic solution is obtained for an unbounded problem, while numerical model has a well defined aquifer boundaries which causes pressure curve to flatten.

4.1.2. Propagating Fracture

The next stage of validation is the simulation of a fracture, growing under the conditions of injection of a single-phase fluid into the reservoir. First, we confirm that for the chosen fluid parameters and injection rate, expected flow regime falls into category of pseudo-radial, according to Koning's classification. For doing so, dimensionless parameter $q_D = \dfrac{Q\mu}{2\pi k h \Delta p}$ is calculated for 3 possible flow rates and then compared with the limiting values given by Koning (see figure 4.3). Larger injection rate Q results in higher dimensionless flow value q_D. Growth of q_D indicates a shift of the flow regime from pseudo-radial ($q_D < 0.61$) towards pseudo-elliptical and, finally, to linear flow ($q_D > 4.5$). Similar ranges are reported by Van den Hoek [103]. As the analytical solution is developed for the radial flow regime, corresponding injection rate of $Q = 60$ m/day is chosen, which is equal to the injection rate of $q = 30$ m^3/day per one fracture wing.

Growing fracture is modeled with chosen parameters. The fracture activity map and pressure solution across the domain before and after fracture propagation stage are given in figures 4.4 and 4.5 respectively.

Dynamics of the fracture growth and development of the pressure inside can be seen in figure 4.6. Numerical fracture length, given in figure 4.6a, has a good match with the analytic solutions. Both curves coincide in terms of fracture initiation time and its length during growth. The moment when the analytic fracture stops growing ($t = 4 \cdot 10^{-3}$ day) coincides with the mo-

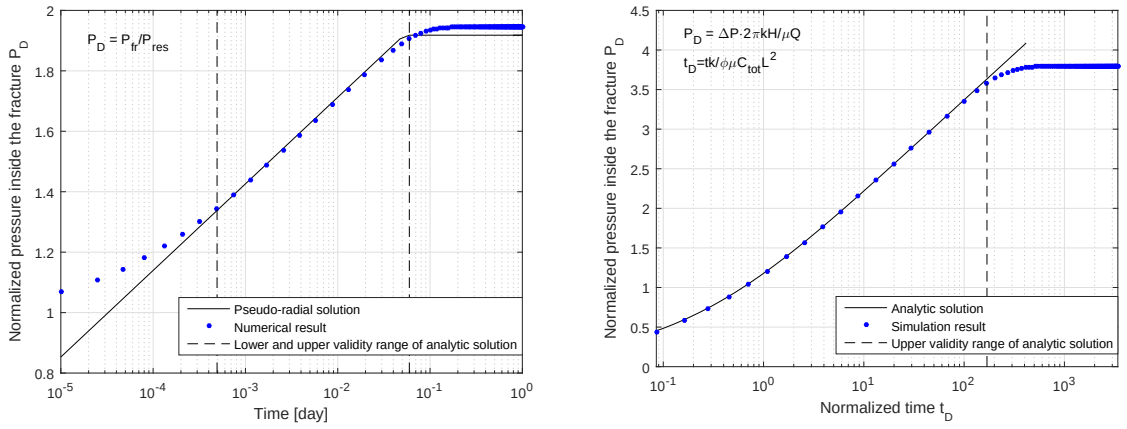

(a) (b)

Figure 4.2: Comparison of pressure dynamics inside the fracture with (a) Koning's pseudo-radial solution [63] and (b) solution obtained through Mathieu functions [104]. Both plots show match between simulated result for a stationary fracture and analytic solutions inside the validity range.

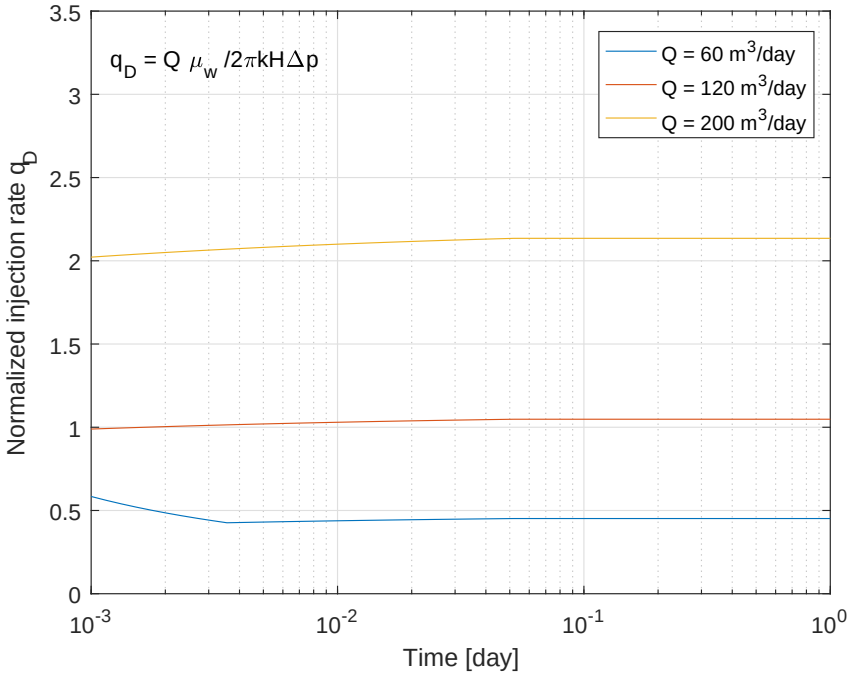

Figure 4.3: Correspondence between the injection rate Q and the dimensionless parameter q_D based on analytic solution for growing fracture. Higher values of Q lead to increase in q_D.

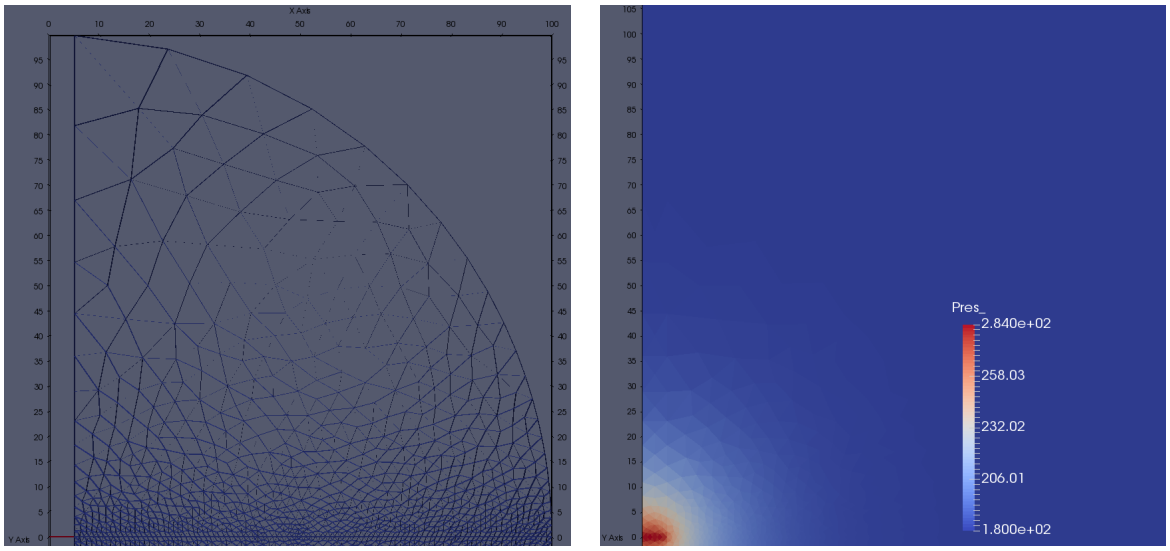

(a) (b)

Figure 4.4: (a) Map of the fracture activity before the fracture started to grow. Red line in the left bottom corner corresponds to the initial fracture, active from the beginning of simulation. Blue lines correspond to non-active fracture segments. (b) Solution for pressure across the domain before fracture starts to propagate.

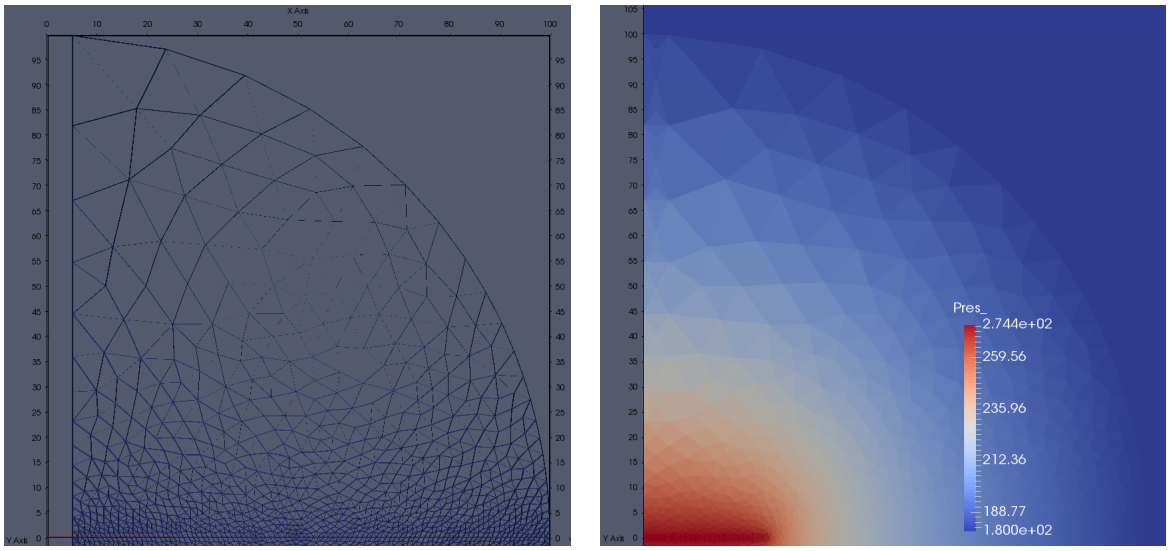

(a) (b)

Figure 4.5: (a) Map of the fracture activity at the end of the fracture growth. Red line of the active fracture extended deep into the domain. The rest of the segments remained non-active. (b) Pressure profile developed according to the new fracture shape. It has a constant high value along the infinite conductivity fracture and a smooth pressure reduction down to the reservoir value at the aquifer boundary.

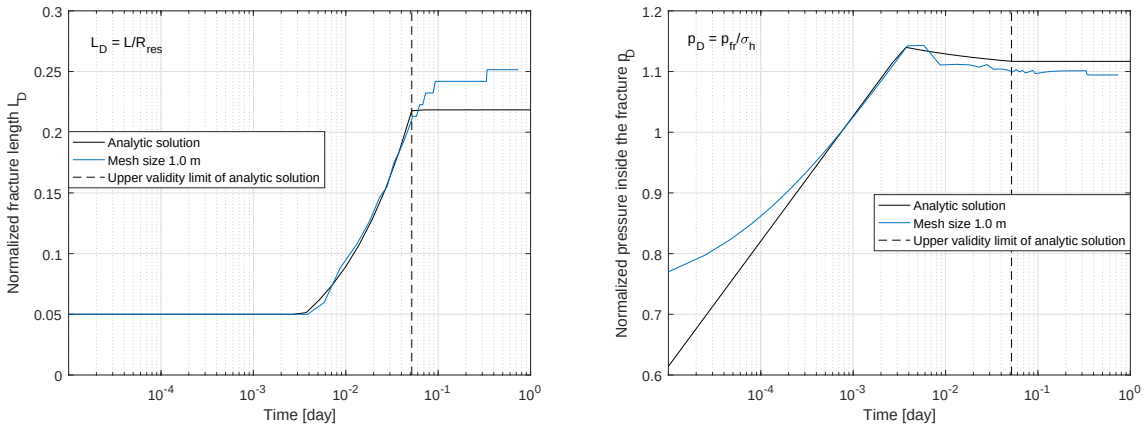

(a) (b)

Figure 4.6: Development of (a)the fracture length and (b) the pressure inside the fracture in numerical model compared with the semi-analytic solution. Numerical model has an average size of the mesh equal to 1.0 m. Time step dynamically grows from $1 \cdot 10^{-5}$ day to $1 \cdot 10^{-2}$ day. Results for fracture length and pressure are normalized by dividing them by the distance to the aquifer R_{res} and the minimum horizontal stress σ_h respectively.

ment when the increase rate of the numerical fracture reduces, which is an indication of the pressure front reaching the aquifers. The difference in the values of final length is caused by the certain simplifications in the semi-analytic solution. Simple logarithmic equations for pressure and stresses (eq. 3.16 - 3.18) are obtained at cost of pressure (and consequently length) cut-off after the pressure wave reaches the aquifer. Early-time transient regime and pressure cut-off upon reaching the aquifer determine the lower and upper validity limits for employed semi-analytic solution. On the contrary, the numerical simulator captures pressure growth inside the fracture after reaching the aquifer. The secondary pressure growth happens due to the residual compressibility of the system.

Pressure buildup inside the fracture is shown in figure 4.6b. To visualize the fracture propagation process, the pressure is normalized over the minimum horizontal stress σ_h. There is a close fit between two curves inside the validity range of analytic solution. Correctness of the numerical pressure solution outside this range was proved in the previous section. During the initial pressure build-up ($t < 4 \cdot 10^{-3}$ day), the pressure in the fracture accumulates above the sum of minimum horizontal stress σ_h and the poro-elastic backstress $\Delta\sigma_p$. When it reaches the critical value, fracture propagates. Less pressure is needed for the fracture to advance when it becomes longer (see equation 3.15). After the moment when first pressure impulse reaches the aquifers, the pressure inside the fracture grows every time slower. This reduction also owes to the residual compressibility of the system. Finally, when pressure solution becomes stationary ($t > 2 \cdot 10^{-1}$ day), fracture growth stops. The difference between two solutions in the final stage ($10^{-1} < t < 1$ day) is caused by the differences in length 4.6a. As the simulation provides a discrete solution, pressure fluctuations due to its accumulation and drop upon opening of a new segment are observed. Analytical solution is smooth due to its continuous nature.

4.2. Multi-Phase Fluid Injection

When fracture growth algorithm is successfully tested in the conditions of a single-phase flow, we proceed with the tests on more complicated cases. In this section, multi-phase flow is considered.

Waterflooding is a common practice in oil recovery operations. In its course, less viscous water is injected into a reservoir with aim to push more viscous oil towards the producing well.

Table 4.2: Fluid properties used in the multi-phase simulation

Fluid parameter	Injected fluid	Displaced fluid
Case 1		
End-point relative permeability k_r	0.3	0.7
Viscosity μ_f, cP	0.5	1.0
Compressibility C_f, 1/Pa	$1 \cdot 10^{-10}$	$1 \cdot 10^{-10}$
Density ρ_f, kg/m^3	1000	850
Irreducible saturation S_i	0	0
Corey exponent	1	1
Mobility ratio M	0.85	
Case 2		
End-point relative permeability k_r	1.0	1.0
Viscosity μ_f, cP	0.5	1.0
Compressibility C_f, 1/Pa	$1 \cdot 10^{-10}$	$1 \cdot 10^{-10}$
Density ρ_f, kg/m^3	1000	850
Irreducible saturation S_i	0	0
Corey exponent	1	1
Mobility ratio M	2.0	

In presence of two fluids with different parameters, pressure profile from fracture towards the pressure distortion front has a broken curve shape, as each fluid zone has its specific pressure gradient. It means that when the pressure front reaches the aquifer boundary, pressure inside the fracture keeps changing due to the expansion of the flooded zone. Whether this pressure grows or drops, depends on the characteristics of the injected fluid.

Analytic solution used for validation was given in section 3.5. As in the single phase flow example, there is no difference in the fluid parameters inside and outside the flooded zone, all the intermediate terms in equation 3.16 disappear. Now, when fluid parameters are different, semi-axes of flooded zone a_w and b_w have to be computed. Equation for the flooded zone semi-axes as well as the pressure distribution inside and outside the flooded zone supposes a piston-like fluid displacement and a constant relative permeabilities of each phase k_{rw} and k_{ro} in every zone. In order to match the numeric solution with the analytic one, ideal piston-like displacement had to be simulated in the model. For doing so, fluid parameters given in the table 4.2 under Case 1 were employed. Mobility ratio $M \leq 1$ means that oil is capable of traveling with the same or even higher velocity than water, which leads to favorable, or piston-like, displacement. On the contrary in Case 2, mobility ratio $M \geq 1$ which means that water is more mobile than oil and can travel faster, therefore by-pass oil forming water tongues or fingers.

Based on the parameters used for Case 1, relative permeability curves shown in figure 4.7a were obtained. They were constructed by the on-line source `mmbbls-app.glassworks.no`. Additionally, it provided the water saturation profile along the reservoir at some specific time. Skipping the input parameters, we show the output in figure 4.7b. Indeed, we clearly see the shock in saturation profile which is characteristic for the piston-like displacement. This combination of the fluids is tested in the non-propagating (subsection 4.2.1) and propagating (subsection 4.2.3) fracture scenarios.

In Case 2, less viscous fluid is injected. Relative permeability curves and saturation profiles are shown in figures 4.8a and 4.8b. Note, that the latter was obtained by means of Welge's approach for determination of the shock front position. In the second figure, we clearly see smearing of the water saturations along the water front. Assumption of piston-like displacement adopted in the semi-analytic solution, is not valid for this case. Numerical modeling of the

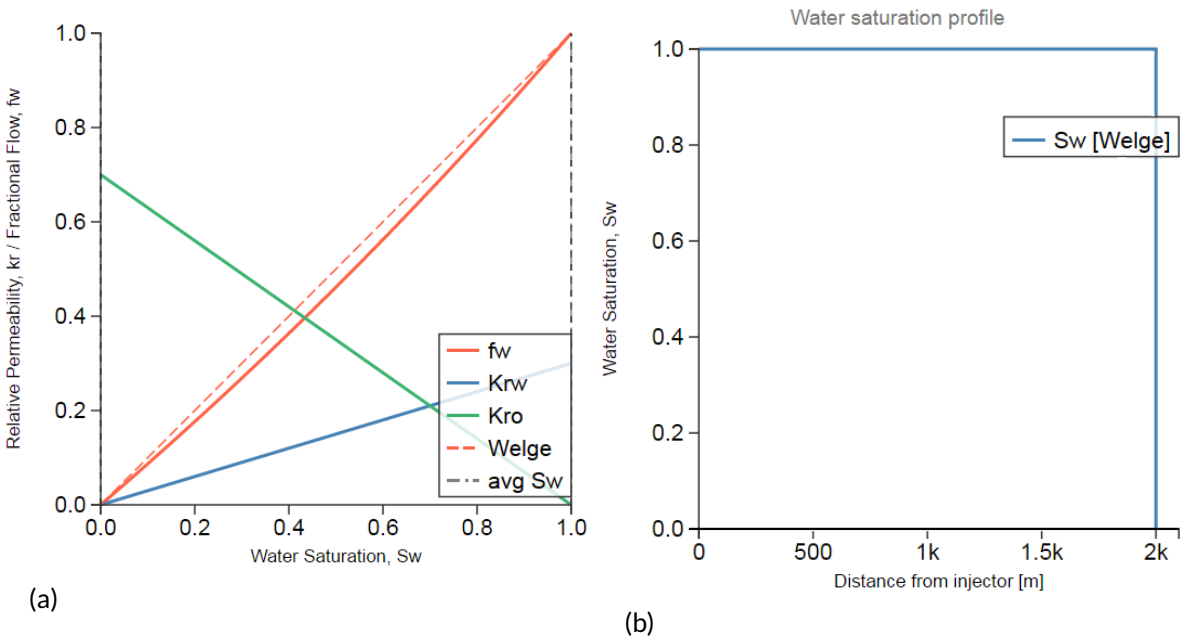

Figure 4.7: (a) Relative permeability curves for case 1 for injected K_{rw} and displaced K_{ro} fluid, fractional flow of water from Buckley-Leverett f_w and Welge solutions, (b) saturation profile at certain time and reservoir dimensions, obtained by Buckley-Leverett $S_w[BL]$ and Welge's $S_w[\text{Welge}]$ solutions.

fracture growth for this fluid combination is done, and the results are compared to the analytic curve qualitatively (see subsection 4.2.4).

4.2.1. Stationary Fracture under the Conditions of Favorable Displacement (Case 1)

First, comparison between the pressure inside the non-propagating fracture and the semi-analytic solution is done. Comparison with the pseudo-radial solution is given in figure 4.9a. The pressure inside the fracture P_{fr} is normalized over the initial reservoir pressure P_{res}. Two curves are matching each other in the late-time stage until the pressure wave reaches the aquifer boundary. Both curves have similar behavior and timing. Difference between two solutions after hitting the aquifer boundary has the similar nature as in the case of the single-phase flow experiment. Secondary pressure growth is caused by the expansion of the flooded zone, which contains less mobile fluid. To prove correctness of the numerical solution in the early-time stage, comparison with the Mathieu solution for transient flow [104] is done. A fair agreement between the numerical data and the analytical curve is observed. As the analytic solution is obtained for an unbounded problem (infinite reservoir), it is valid only until the moment when pressure wave reaches the aquifer boundary.

4.2.2. Stationary Fracture under the Conditions of Unfavorable Displacement (Case 2)

In the second case, more mobile fluid is injected into the reservoir filled with the less mobile oil. Such combination of the injected and displaced fluid is characterized by the unfavorable displacement type. As a result, no shock in saturations is observed, and flooded zone front is smeared. Water saturation profiles for favorable and unfavorable displacement types obtained in the simulations are given in figure 4.10.

Result of numerical simulation of unfavorable displacement type (case 2) is given in figure 4.11. Comparison of the normalized pressure curve with pseudo-radial analytic solution is shown in figure 4.11a. Although two pressure curves have similar behavior, numerical curve is less steep than the analytical one. The reason for this difference is the assumption of piston-like

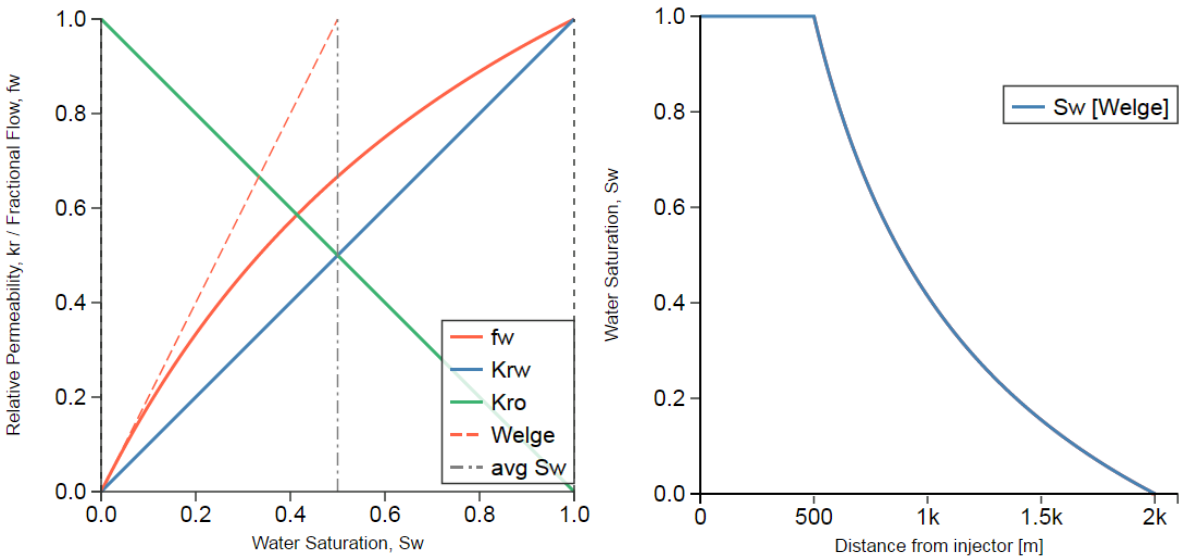

(a) (b)

Figure 4.8: (a) Relative permeability curves and (b) water saturation profile for case 2.

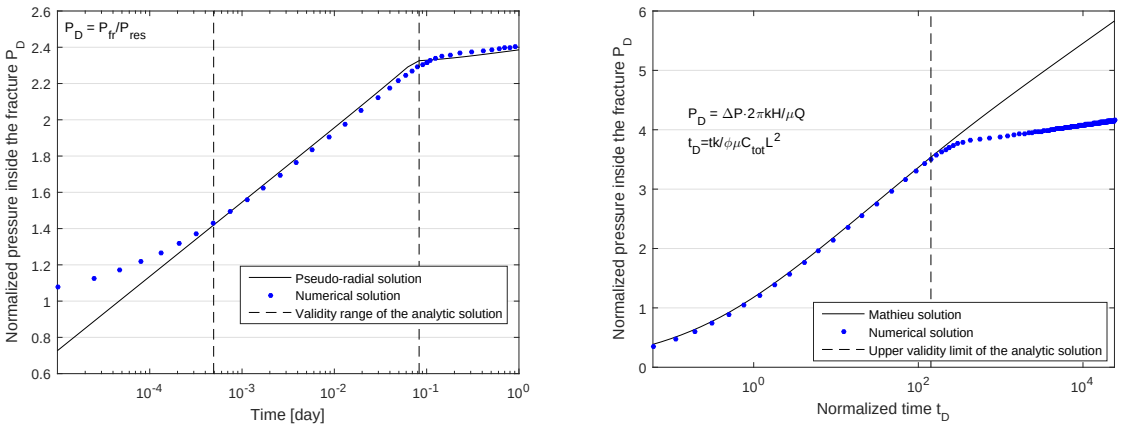

(a) (b)

Figure 4.9: Pressure growth inside the stationary fracture in the multi-phase flow conditions. Comparison with (a) pseudo-radial analytic solution and (b) solution obtained with Mathieu functions. Numerical result matches both analytic curves within their validity ranges.

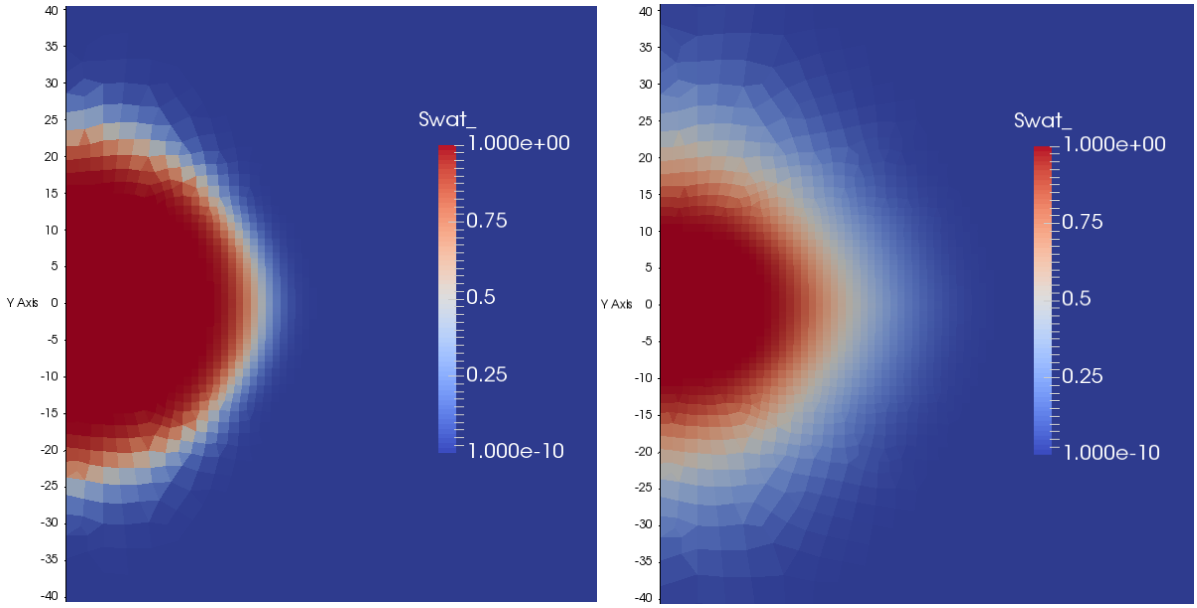

(a) (b)

Figure 4.10: Water saturation profiles for (a) favorable (case 1) and (b) unfavorable (case 2) displacement types. In case 1, water front is well defined and corresponds to the piston-like displacement, while in case 2, water saturation is smeared along the larger area.

displacement in the analytic solution for pressure, which does not hold for chosen fluid parameters. Both curves exhibit decline in the secondary stage. This behavior is the result of the growth of the flooded zone, which contains more mobile fluid in it. As a result, displacement of this fluid requires less steep pressure gradient, than the original oil. Comparison of the normalized pressure with Mathieu solution is given in figure 4.11b. Within the range of applicability of the analytic solution two curves coincide in the early-time stage and deviate in the later stage due to the reasons described above.

4.2.3. Propagating Fracture under the Conditions of Favorable Displacement (Case 1)

When the solution for a stationary fracture is matched with analytical one, we proceed with simulation of the propagating fracture. Similar injection rate of $Q = 30$ m3/day was used as in the single-phase flow example.

Numerical solution for length (see figure 4.13) has perfect match with the analytical solution during the primary crack growth. In this stage, the main driver of propagation is pressure growth in reservoir which is almost 100% filled with oil. After the pressure wave reaches the aquifer, analytic solution "freezes" while numerical solution continues to develop, as it accounts for the residual compressibility of the fluid. Existing difference in length values remains. The secondary crack growth is caused by expansion of the flooded zone. Parameters of the injected and displaced fluid were chosen in such a way, that injected fluid is less mobile than the displaced one. In order to displace a larger volume of the less mobile fluid, fracture surface has to increase. Therefore, expansion of the flooded zone leads to the fracture growth. Rate of the secondary crack extension for numerical and analytic solutions coincide. Two curves stay parallel until the end of the simulation.

Solution for the pressure is shown in figure 4.12. While two solutions differ in the early-time stage due to limited applicability of the analytic equation, there is a fair agreement in the late-time stage. It includes pressure break time due to crack growth initiation as well as further pressure decrease due to the crack opening.

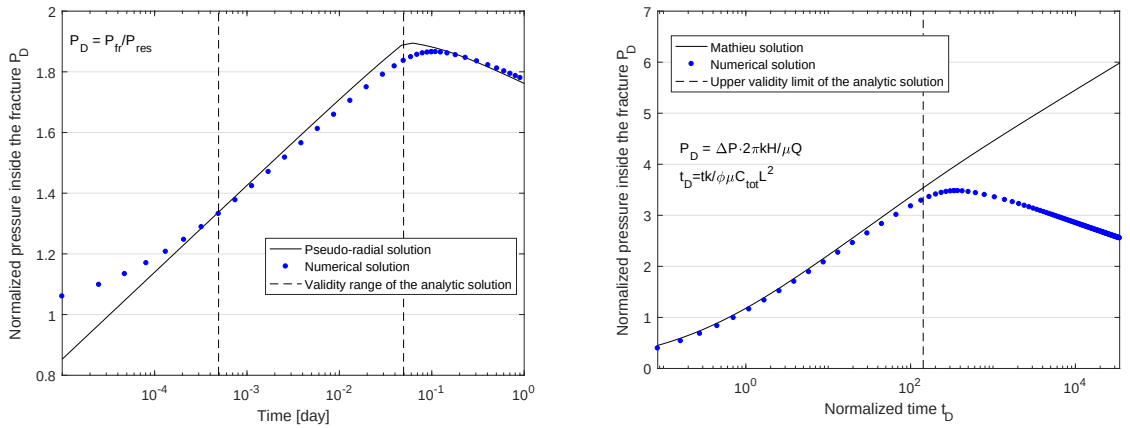

(a) (b)

Figure 4.11: Pressure development inside the stationary fracture in the multi-phase flow conditions for the case 2. Comparison with (a) the pseudo-radial analytic solution and (b) the solution obtained with Mathieu functions. Numerical result and analytic curves have similar behavior within their validity ranges. Reduction of the pressure in the secondary stage is caused by increase of the flooded zone with more mobile fluid in it.

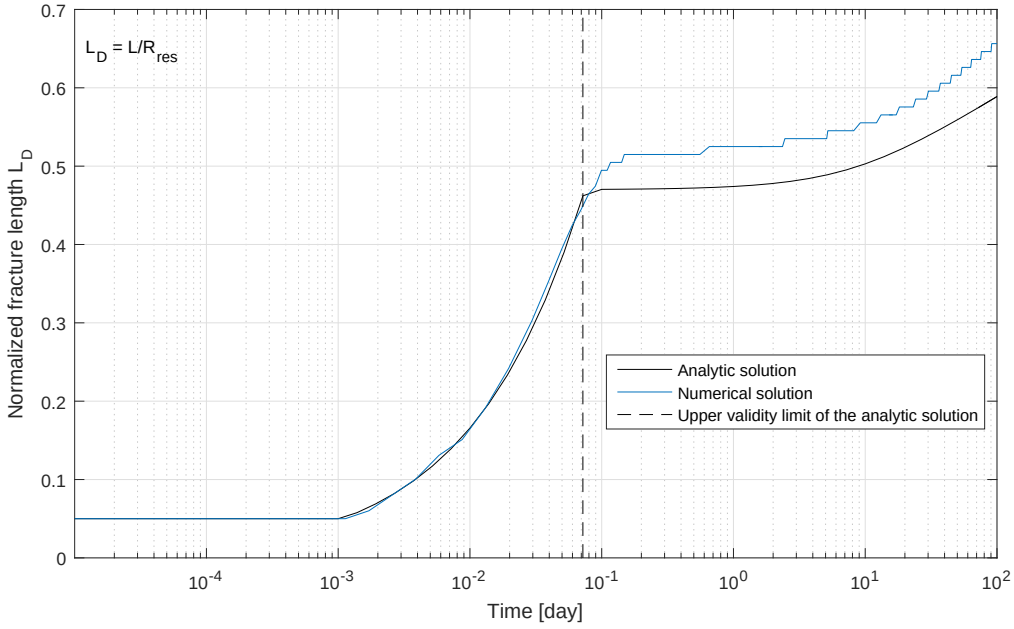

Figure 4.12: Comparison between numeric and analytic solutions for normalized length L_D in conditions of multi-phase flow (case 1). Numerical length is matching the analytical one during the primary growth stage and has the same increase rate during the secondary growth stage.

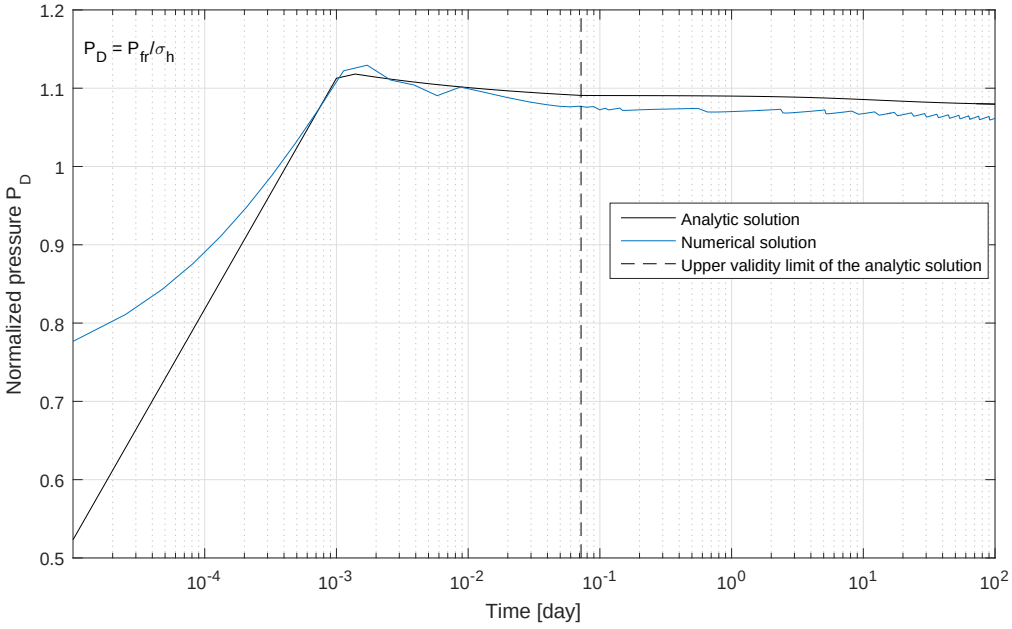

Figure 4.13: Comparison between numeric and analytic solutions for normalized pressure p_D in conditions of multi-phase flow (case 1). Two curves differ in the early-time stage due to limited validity of analytical solution. Both solutions indicate similar fracture growth initiation time, after which pressure decrease as the fracture keeps opening.

4.2.4. Propagating Fracture under the Conditions of Unfavorable Displacement (Case 2)

When modeling the second case of fluid parameters, more mobile water is injected into less mobile oil. This leads to smearing of the water saturation profile. Piston-like displacement assumption, adapted in the analytic solution, could not be satisfied. At the same time, the reservoir simulator can accurately model both saturation front and pressure profile.

Results of the simulation and its comparison with the analytic curve is given in figures 4.14 and 4.15. Primary fracture growth shown in figure 4.14 is caused by initial pressure build-up across the domain. In the second stage, expansion of a zone flooded containing more mobile fluid, leads to the gradual fracture closure. As smaller fracture surface is needed to displace more mobile fluid, fracture shortens. Both numeric and analytic curves capture the closing behavior. In the normalized pressure plot (figure 4.15), moderate separation between two solutions during the initial pressure growth can be seen. Reason behind is the assumption of favorable displacement type in analytic solution. In order to show the limiting range of the numerical solution, the semi-analytic curves for average viscosity across the reservoir equal to 1 cP and 0.8 cP is plotted. The first value corresponds to the initial moment, when original reservoir fluid is not displaced. The second value corresponds to a case when significant part of the reservoir fluid is displaced by less viscous water. In transition from the first value to the second, fracture growth initiation delays and final fracture becomes shorter. In terms of pressure, for the second viscosity value, pressure curve is less steep during the initial pressure build-up (see figure 4.15). Similar tendency is observed in the numerical solution: fracture growth starts later and pressure curve is less steep than in the analytic solution. After length increase stabilizes, fracture starts to close due to expansion of the flooded zone. This example illustrates the ability of the developed numerical model to reproduce fracture closure phenomena, also observed during the lab experiments on hydraulic fractures (see [23], [100]). By this, the validation of the developed model for multi-phase flow conditions is completed.

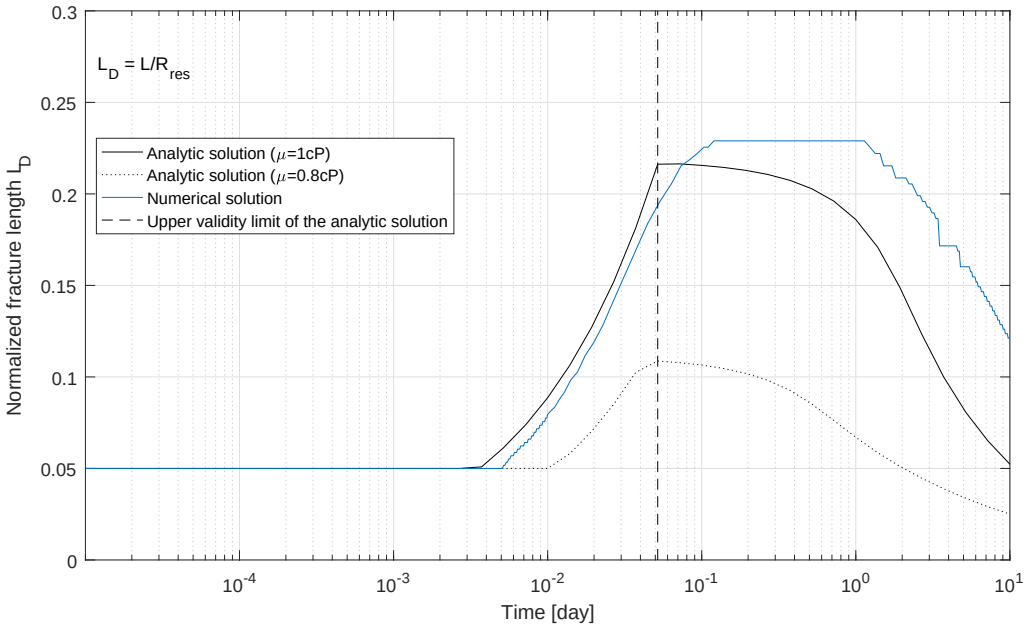

Figure 4.14: Comparison between numeric and analytic solutions for normalized fracture length L_D in conditions of multi-phase flow (case 2). Length development profiles have similar behavior during primary and secondary stage.

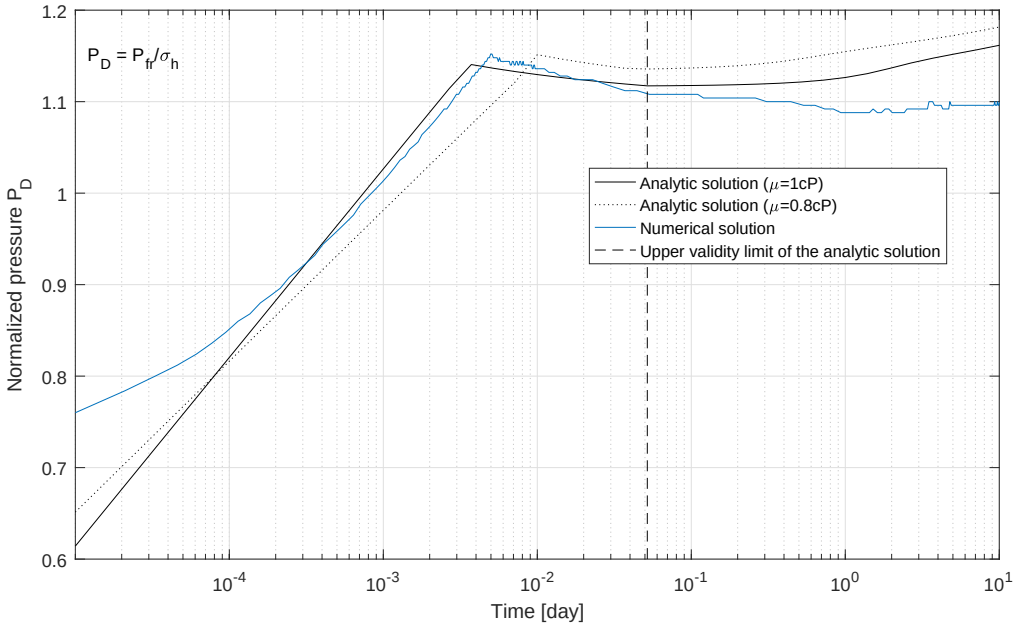

Figure 4.15: Comparison between numeric and analytic solutions for normalized pressure p_D in conditions of multi-phase flow (case 2). Pressure profiles have similar behavior.

Table 4.3: Fluid and rock properties used in the thermal simulation

Rock properties & stresses	**All cases**
Matrix porosity ϕ	0.3
Matrix permeability k, mD	250
Fracture conductivity c_{fr}	∞
Density ρ_r, kg/m^3	2500
Biot modulus α	1
Young's modulus E, Pa	$5 \cdot 10^{10}$
Initial reservoir pressure p_r, Pa	$500 \cdot 10^5$
Poisson's ratio ν	0.25
Compressibility C_r, 1/Pa	0
Linear thermal expansion coefficient a_T, 1/K	$1.5 \cdot 10^{-6}$
Volumetric heat capacity c_r, kJ/m^{3}K	1975
Thermal conductivity λ_r, kJ/m day K	0
Cohesion c, Pa	$1 \cdot 10^{10}$
Friction angle φ, °	0
Dilation angle ψ, °	0
Total horizontal stress σ_x, Pa	$-620 \cdot 10^5$
Total horizontal stress σ_y, Pa	$-570 \cdot 10^5$

Fluid properties	**Case 1**	**Case 2**
Density ρ_f, kg/m^3	1000	1000
Viscosity μ_f, cP	1	1
Compressibility C_f, 1/Pa	$1 \cdot 10^{-8}$	$1 \cdot 10^{-9}$
Thermal conductivity λ_f, kJ/m day K	0	0
Volumetric heat capacity c_f, kJ/m^{3}K	4185	4185
Injection rate (into half-fracture) Q, m^3/day	30	30

4.3. Injection of Cold Single-Phase Fluid into Hot Reservoir with the Growing Fracture

In previous examples, the effect of thermo-elasticity was ignored, assigning the injected fluid temperature similar to the one from reservoir. Now, the effect of rock cooling on the fracture propagation is accounted. For the current simulation, single-phase scenario (injection of water into water) is adopted, but with different fluid temperatures. Fluid and rock parameters used in the following test are given in the table 4.3.

As it was shown in section 3.5, the semi-analytic solution is based on the assumption of zero heat conduction. To reproduce similar set-up, zero thermal conductivity is assigned both for rock and fluid in the numerical model.

To delay the effect of fracture growth due to pressure buildup and to capture pure growth due to rock shrinkage in Case 1, fluid with high compressibility $1 \cdot 10^{-8}$ 1/Pa was used (see table 4.3). In such setup, pressure growth between fracture and aquifer boundary is slower than in previous simulations. However, cold fluid filtration through the rock happens at similar rate and formation steady cools down. Reduction of the effective stresses, necessary for the fracture to propagate, happens first due to the thermal contraction of the rock rather than high pressure inside the fracture. Nevertheless, further contribution of the fracture pressure and poro-elastic effects increases and adds to the thermo-elastic driver. After that moment, crack propagation is due to both pressure and temperature effects. Analytic solutions for fracture pressure and length extension with and without temperature effects can be seen in figure 4.16.

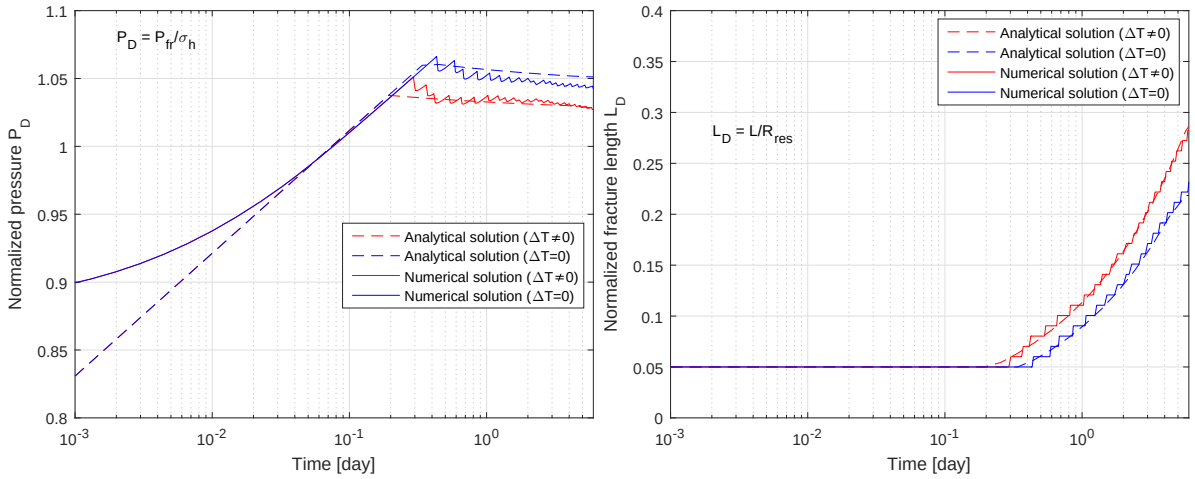

(a) (b)

Figure 4.16: Comparison between numeric and analytic solutions of (a) normalized pressure inside the fracture P_D and (b) normalized length L_D in thermal simulation

Rock shrinkage due to cooling leads to reduction of pressure inside the fracture, necessary for it to propagate. This effect is clearly seen when comparing analytic pressure curves with and without temperature effect (figure 4.16a). Similar behavior is observed in the length vs. time plot in figure 4.16b. "Cold" fracture starts growing earlier than the isothermal one. Besides that, when the latter stops extending, "cold" fracture keeps growing due to strong thermo-elastic effect. Results of the numerical simulations are given in the same figure. Both numerical results for isothermal and thermal simulations are in fair agreement with the analytic results. Effect of thermo-elasticity is particularly revealing itself in different timing of fracture growth initiation and is perfectly captured by the numerical model.

When pronounced effect of rock contraction due to cooling was demonstrated on the example of exaggeratedly high fluid compressibility, previous value of $1 \cdot 10^{-10}$ 1/Pa is used (see table 4.3 Case 2). Results of the numerical simulation including and excluding thermal effects are shown in figure 4.17. As compressibility of the fluid is much higher, development of pressure in the domain is faster than in Case 1. Although thermal rock contraction takes place, its effect on fracture growth comes moments before the crack starts growing due to pure pressure effect. This conclusion is based on the minimal separation between analytic curves for fracture length with and without thermal effects (fig. 4.17b). After the pressure wave reaches the aquifer, fracture growth due to pressure stops, which is observed from the analytic curve for L_D in isothermal conditions. On the contrary, fracture keeps growing only due to rock contraction in the thermal case. Simulated results, also given in figure 4.17, show good accordance with analytics. Numerical curve for length in isothermal conditions fits analytical curve during the initial growth stage. Additionally to that, it captures secondary fracture growth which happens due to compressibility of the fluid after the aquifer boundary is reached by the pressure impulse. As was already mentioned, this effect could not be properly addressed by semi-analytic solution. Similar behavior of numerical curve accounting for thermal effect is observed. It captures initial fracture growth (until reaching the aquifer) and secondary growth due to residual pressure buildup and thermal effect. As analytic solution doesn't have residual pressure growth and accounts only for the thermal growth in the secondary stage, there is a constant gap between two curves.

Analytic and numerical solutions for pressure inside the fracture is shown in figure 4.17a. Similarly to analytic results, numerical model with thermal effects requires less pressure to

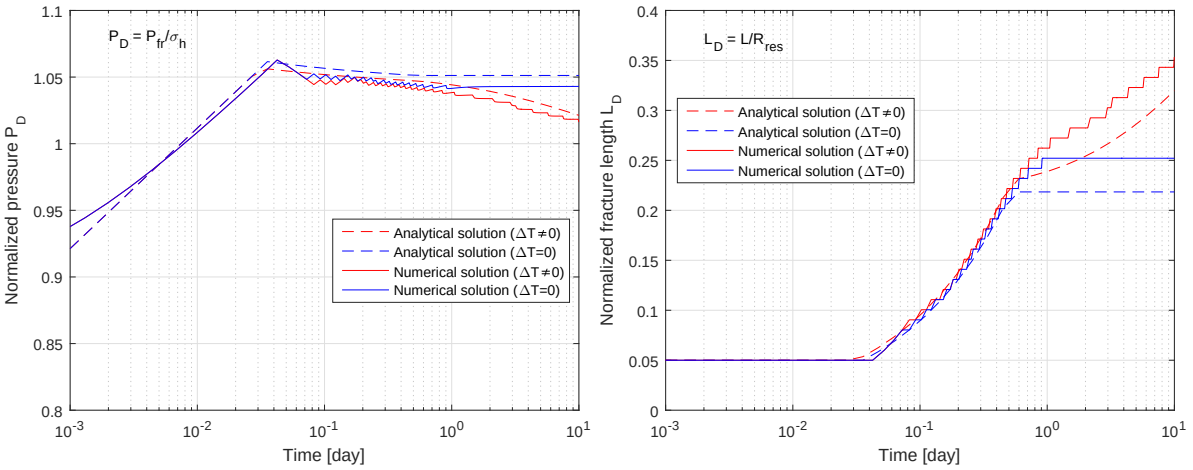

(a) (b)

Figure 4.17: Case 2: comparison between numeric and analytic solutions of (a) normalized pressure inside the fracture P_D and (b) normalized length L_D.

propagate the fracture than the isothermal one. Secondary fracture growth due to the thermoelastic effect forces pressure to drop below constant pressure line in isothermal case.

4.3.1. Material Contraction Along the Fracture

Developed model was able to capture the effect of strong rock contraction along the fracture faces. Simulation of a stationary fracture with nonphysically high value of linear thermal expansion coefficient $a_T = 6 \cdot 10^{-6}$ 1/K was performed. High tensional stress σ_1 in front of the crack tip (see region in front of the crack tip in figure 4.18b) is the one leading to intensive fracture growth. Its nature was already shown and explained in the previous subsections. Here, high horizontal tensional stress along the fracture is noted (see region along the crack face in figure 4.18a). It is much higher than the one perpendicular to it (see figure 4.18b). It is caused by the larger area of contracted rock along the fracture than perpendicular to it. Strong tension along the fracture face may cause thermal fractures to develop. This type of fractures was reported in literature [6, 9, 83]. Perkins and Gonzalez [83] refer to them as to secondary fractures. They attribute appearance of these fractures to flat cooled regions around long primary fractures and relate them to leveling of the effective principle stresses $\sigma'_0 = \sigma'_1$ (see figure 4.19). As the developed algorithm is designed to model slow hydraulic fracturing process where single continuous fracture develops, growth of secondary thermal fractures is not currently accounted. However, model is properly capturing temperature and stress changes leading to appearance of such fractures.

4.4. Study of Model Sensitivity to Parameters

The following step in the model verification is testing the effects of various model parameters on the results. In this section, the effects of such parameters as an average mesh size, timestep, and initial fracture length are tested. All the tests are done on the base of setup where single-phase fluid is injected into the reservoir. Parameters of the fluid and the rock are given in table 4.1 unless otherwise indicated.

4.4.1. Mesh Refinement Study

To evaluate the effect of mesh size on the resulting solution, mesh refinement study was conducted. Simulations were done with four different average mesh size: 2.0 m, 1.0 m, 0.5 m and 0.25

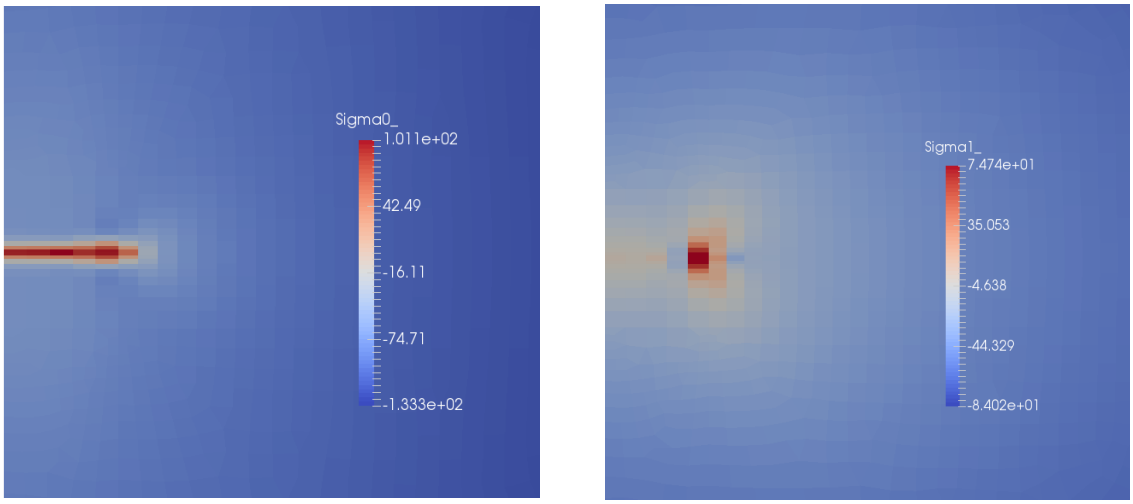

(a) (b)

Figure 4.18: Effective stress maps around the crack in (a) horizontal σ_0 and (b) vertical σ_1 directions. There are highly tensional stresses along the crack faces in horizontal direction. Tension in perpendicular direction is much lower on the fracture face. Highly tensional stresses are observed in front of the crack.

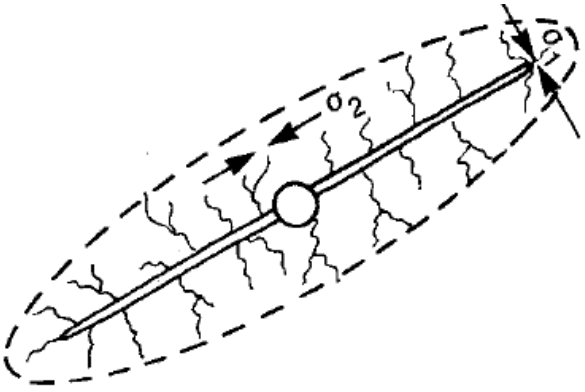

Figure 4.19: Secondary thermal fractures perpendicular to fracture face. Source: Perkins and Gonzalez [83]

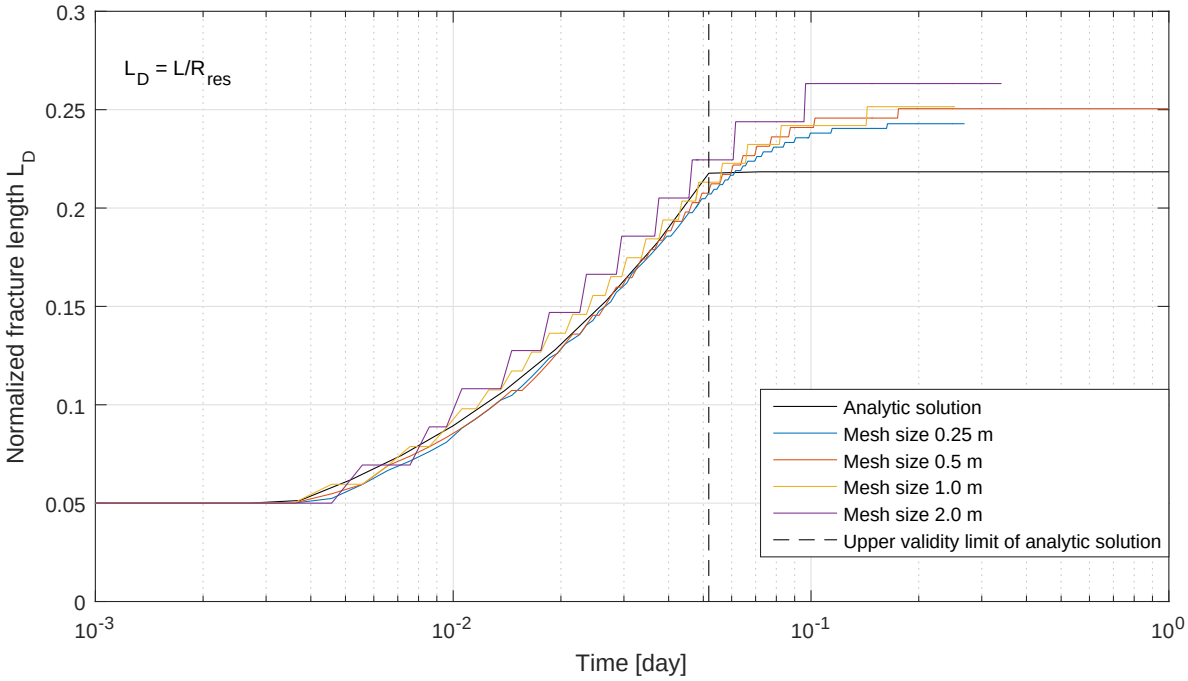

Figure 4.20: Fracture length comparison in the mesh refinement study for simulations with the maximum time step equal to $1 \cdot 10^{-3}$ day. Increase of the average mesh size makes the numerical fracture exceed its analytic analogue. Solutions obtained with average mesh size of 0.25 m and 0.5 m fit the analytic solution

m. Maximum time step employed was $1 \cdot 10^{-3}$ day. Following results were obtained. Figure 4.20 shows the effect of average mesh size on the fracture growth. Curves corresponding to meshes of 0.25 m and 0.5 m are in fair agreement with each other and with the analytic curve. Results for the larger mesh sizes are slightly displaced to the left of the analytic solution. That indicates that the numerical solution passes ahead of the analytical one, and the fracture develops earlier than it should be. Analysis of the length plotted against time allows drawing a conclusion that for the chosen time step, solution obtained on meshes with average size less or equal to 0.5 m is already converged.

Figure 4.21 shows variation in pressure inside the fracture for four mesh sizes. Larger mesh displays higher jumps in pressure upon opening of each segment. For smaller mesh sizes these jumps are less noticeable as smaller volume of newly opened fracture has to be filled with a fluid. Pressure for the mesh size of 2.0 m stays below all other curves which is also correlated with the previous figure 4.20: longer fracture has lower pressure inside.

Figure 4.22 gives overview of K_{I} during iteration process. Only 3 out of 5 curves were left to make the plot less dense. Each "tooth" represents one time step. Every node on the tooth is one Newton iteration within the time step. In the beginning, pressure in the fracture is too low, so that $K_{\mathrm{I}} = 0$. When pressure starts to overcome the total normal stress acting on the fracture face, K_{I} starts growing. If during iterations value of K_{I} grows above fracture toughness K_{Ic} (horizontal line at 30 bar$\sqrt{m}$ level), algorithm tends to drop it by extending the fracture. During the following iterations within the same time step, segments are opened. Opening of one segment leads to drop in K_{I} as the pressure redistributes within all the fracture segments including the newly opened. This happens until K_{I} goes below K_{Ic} . When K_{I} is below it and all other norms are satisfied, solution is accepted, saved and the next time step is initiated. K_{I} curve for larger mesh size has higher jumps than the smaller mesh sizes. It happens due to the fact that opening of one segment in a mesh with a size of 2 m decreases pressure more than the same event in a mesh with a size of 0.25 m. Larger drop of pressure leads to relaxation of stresses and

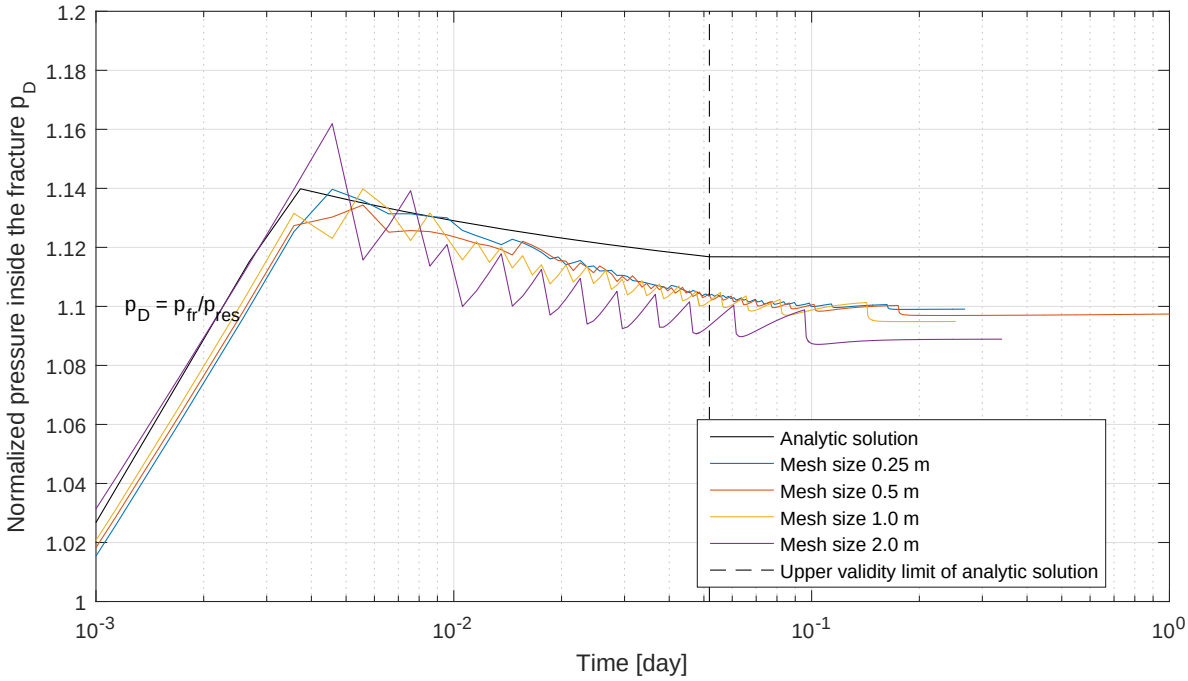

Figure 4.21: Pressure inside the fracture in the mesh refinement study for simulations with the maximum time step equal to $1 \cdot 10^{-3}$ day. Curve for a larger mesh size exhibits higher pressure jumps upon opening of new fracture segments. Pressure curves corresponding to denser meshes show smoother behavior

therefore smaller values of the Stress Intensity Factors. Higher number of iterations is needed for a model with larger mesh size to grow the K_{I} above the K_{Ic}. As a result, solutions for denser meshes have fewer iterations per time step. As the pressure inside the fracture grows slower after the pressure wave reaches the aquifer boundary, more iterations are needed to build-up K_{I} in the late time stage.

4.4.2. Time Step Size Effect

In current subsection, effect of time step size on the solution for pressure and fracture length is studied. Following simulations were done on the same model with average mesh size equal to 0.5 m. Range of the used time steps has the smallest one of $1 \cdot 10^{-3}$ day and the biggest of 0.1 day. Time step was fixed throughout the whole simulation. First data point of each solution corresponds to the time step size employed.

In figure 4.23, length solution for different time steps is plotted. The smaller the time step, the closer the numerical solution is to the analytical curve. Increase of the time step shifts the numerical result to the right of the analytical one. In physical terms, it leads to delay in the fracture growth. Irrespective of the time step employed, all solutions yield the same final fracture length. It is important to mention, that irrespective of the chosen time step, all the curves have similar increase rate during the active fracture growth.

Figure 4.24 shows variation of pressure inside the fracture for solutions obtained with different time steps. All the solutions exhibit similar height of fluctuations as they were obtained on the same mesh. However, width of the fluctuations is different for different time steps. Numerical pressure curves are very close to each other irrespective of how close is the numerical solution for length to the analytical one.

Analysis of both plots led us to conclusion that in order to capture the fracture growth, time step size should be sufficiently small. Absence of the evaluation points during the active fracture growth stage ($4 \cdot 10^{-3}$ day to $5 \cdot 10^{-2}$ day) for solutions with large time steps caused significant

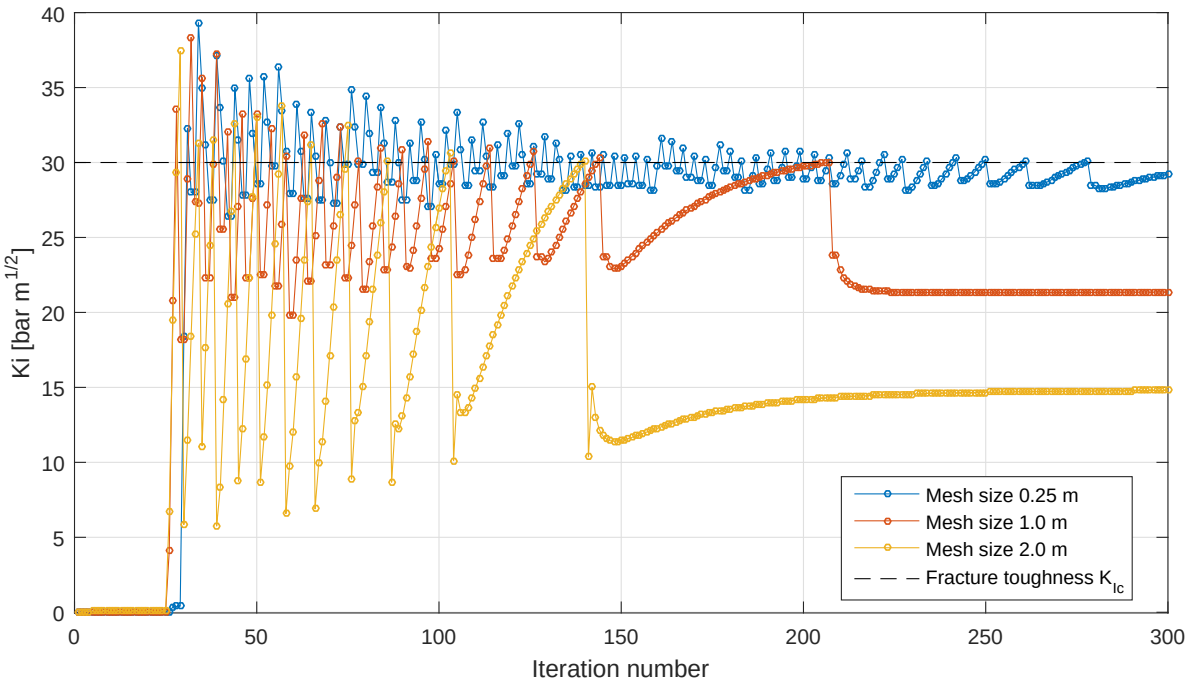

Figure 4.22: Development of the Stress Intensity Factor for Mode I K_I for simulations with 3 different average mesh sizes and the maximum time step equal to $1 \cdot 10^{-3}$ day. Solution for larger mesh size exhibit higher fluctuations due to opening of elements with larger size and following stresses relaxation.

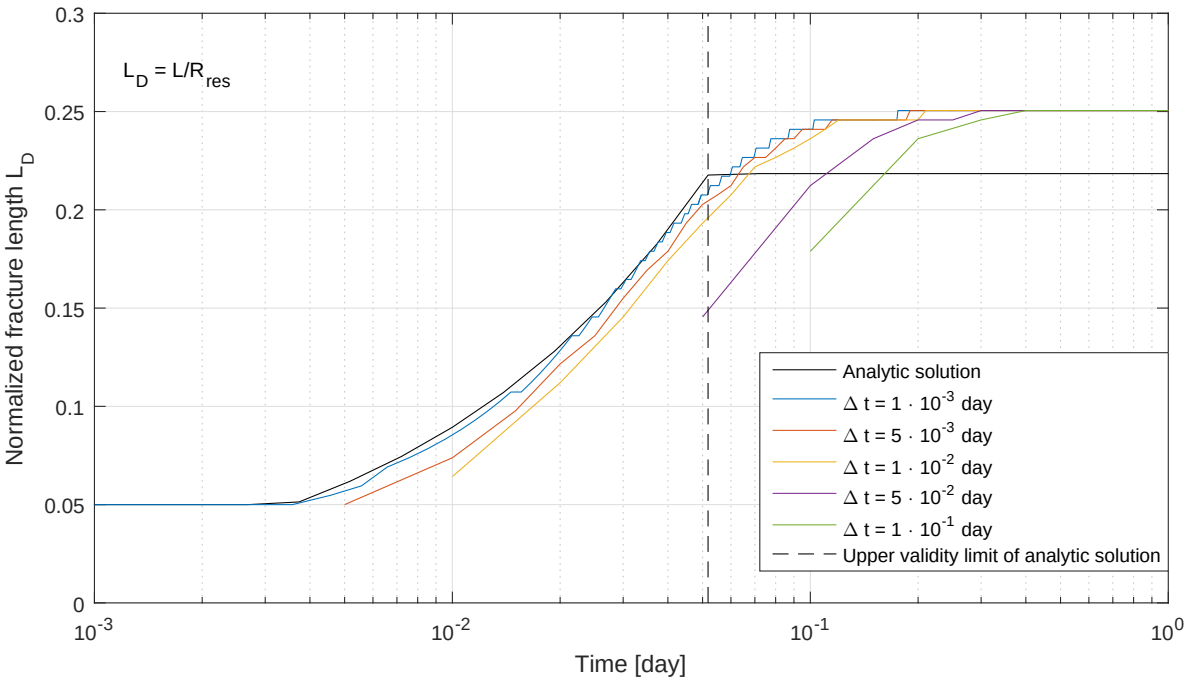

Figure 4.23: Fracture length comparison in the time step refinement study for the model with the average mesh size equal to 0.5 m. Increase of the time step leads to the delayed fracture growth. Irrespective of the time step size, the final fracture length and increase rate are similar for all the simulations. Length obtained with the smallest time step size ($1 \cdot 10^{-3}$ day) has the best match with analytic length in its validity range.

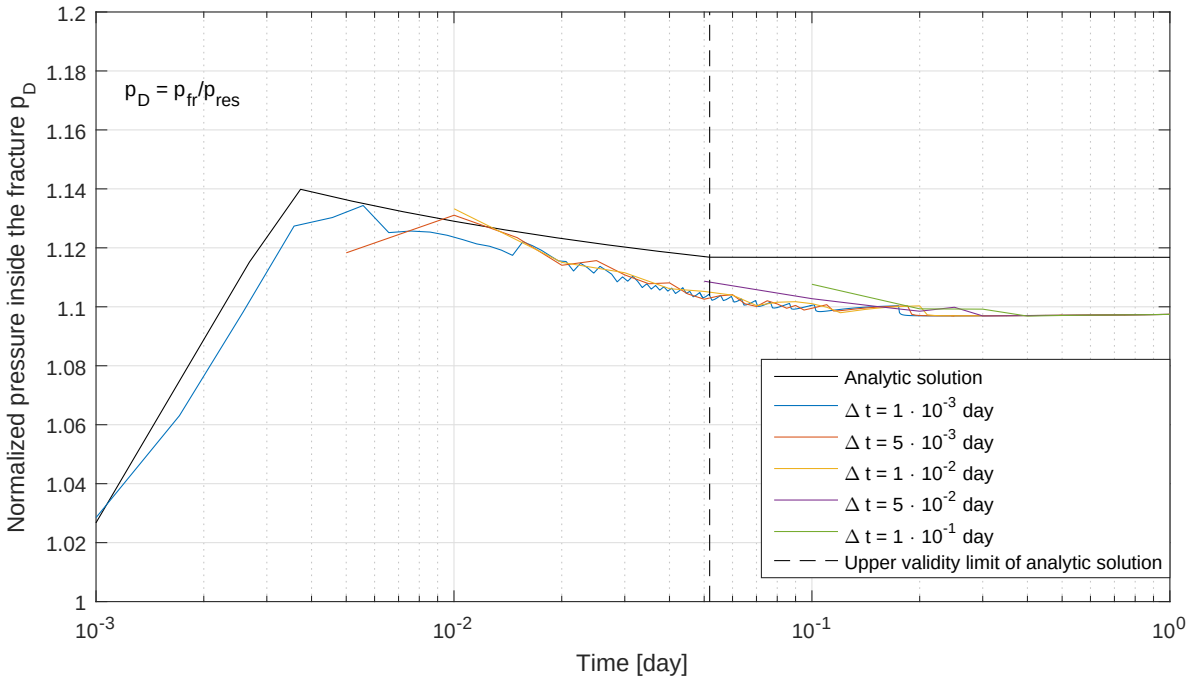

Figure 4.24: Pressure inside the fracture in the time step refinement study for the model with the average mesh size equal to 0.5 m. Pressure curve obtained with the smallest time step size ($1 \cdot 10^{-3}$ day) has the best match with analytic pressure in its validity range.

delay in length development.

Figure 4.25 shows the behavior of K_{I} value during iteration process with 3 different time steps. 2 other curves were removed to make the plot less dense. The value of K_{I} rises above K_{Ic} during the first iteration of every time step. In the further iterations, the algorithm opens segment by segment to relieve the K_{I} value. Finally, when K_{I} is below K_{Ic}, solution is converged, and the next time step is initiated. Solution obtained with larger time step has larger initial value of K_{I}, as the pressure had more time to build-up. Further, algorithm does more iterations in order to drop the K_{I} value, therefore activates more segments in one time step.

4.4.3. "Virtual" Fracture Segments Aperture Effect

As some artificiality was introduced into both mechanical and flow scheme in the form of additional volumes of the "virtual" fracture segments, the effect of these volumes on the final solution was investigated. 4 models with different opening sizes were tested. To make the formulation of the problem dimensionless, ratio between the volume of an average "virtual" fracture segment V_{vf} and the volume of an average "normal" cell V_{cell} is given. Following ratios $\frac{V_{\mathrm{vf}}}{V_{\mathrm{cell}}}$ were employed: $2 \cdot 10^{-7}$, $2 \cdot 10^{-5}$, $6 \cdot 10^{-3}$ and $2 \cdot 10^{-2}$. Note that all the previous simulations were done with the default value of ratio $\frac{V_{\mathrm{vf}}}{V_{\mathrm{cell}}} = 2 \cdot 10^{-5}$. Same mesh with average size of 1.0 m was used in all simulations. Adaptive time step with the smallest value of $1 \cdot 10^{-5}$ day and the highest value of $5 \cdot 10^{-3}$ day was used. The results of the tests are given in figures 4.26 and 4.27.

Figure 4.26 shows effect of the "virtual" fracture segment aperture on the fracture length. Reduction of the ratio $\frac{V_{\mathrm{vf}}}{V_{\mathrm{cell}}}$ below the default value doesn't have any effect on the solution. Both curves fit the analytic solution. However, increase of the ratio $\frac{V_{\mathrm{vf}}}{V_{\mathrm{cell}}}$ above the default leads to premature fracture growth and longer final solution. It is seen in figure 4.27 that pressure also

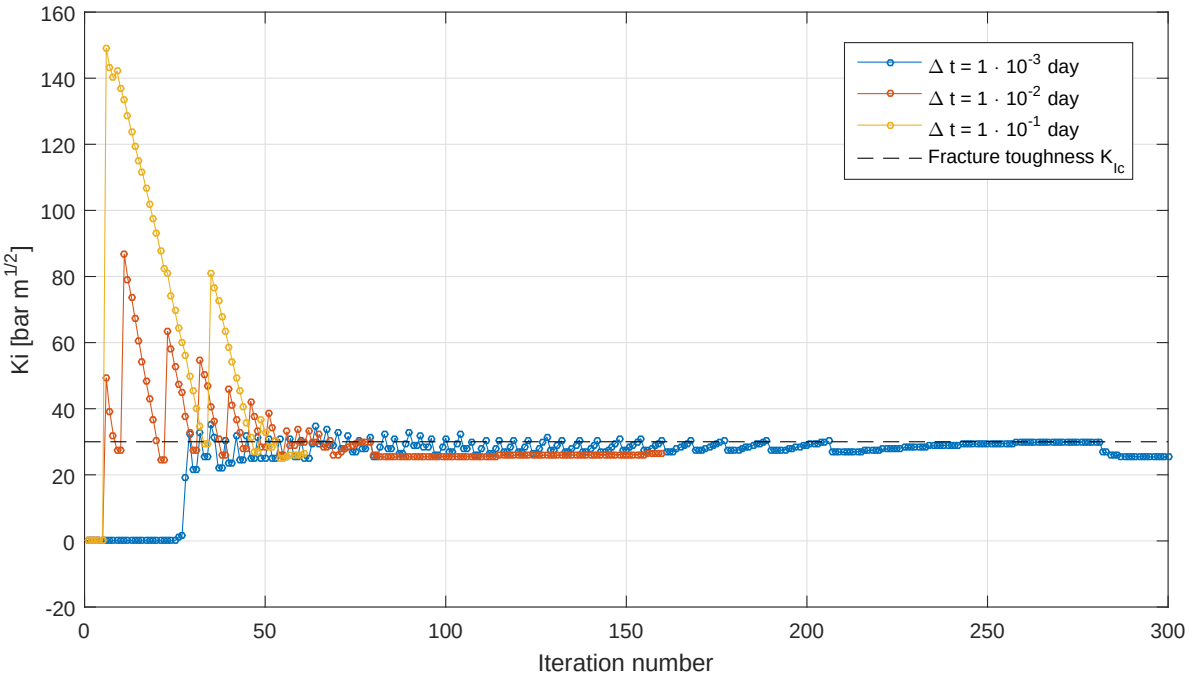

Figure 4.25: Development of the Stress Intensity Factor for Mode I K_I for simulations with 3 different time step sizes and single mesh with average size equal to 0.5 m. Solution obtained with the larger time step exhibit higher jumps in the K_{I} value and consequently has higher number of iterations to decrease it by opening fracture segments.

builds up faster than in the default case. The reason behind is the fact that, although the aperture of the "virtual" segments was increased, corresponding conductivity and therefore transmissibility values were not updated. Thus, larger volume had conductivity value corresponding to a smaller one. As a result, fluid flow from the fracture towards the formation was impeded, which in its turn, accelerated pressure growth inside the fracture. High pressure inside the fracture and weak fluid filtration led to a faster fracture growth.

In order to exclude the effect of the conductivity of the "virtual" fracture segments, it was increased proportionally to the segment's volume. The last curve presented in figures 4.26 and 4.27 corresponds to simulation with updated conductivity. This curve coincides with the numerical curve for default value and fits the analytic solution. By this, I conclude, that when the "virtual" segment aperture and its conductivity are upscaled correspondingly, no effect on final solution for pressure and fracture length is observed.

4.4.4. Initial Fracture Length Effect

Models with 3 different initial lengths of the fracture were tested. The following lengths were used: 5 m, 10 m and 15 m. Results of the simulations together with corresponding analytic curves are given in figures 4.28 and 4.29. Larger initial length leads to the slower pressure development. However, after initiation of the fracture growth, curves for length and pressure for all 3 models merge with each other and with the analytical solution.

4.4.5. Effect of the Total Compressibility C_t

Variation of the total compressibility C_t was studied on the model with average mesh size equal to 1.0 m and adaptive time step size with the maximum value of $5 \cdot 10^{-3}$ day. 3 compressibility values were used: $5 \cdot 10^{-11}$ 1/Pa, $1 \cdot 10^{-10}$ 1/Pa and $5 \cdot 10^{-10}$ 1/Pa. Results of the simulations are given in figures 4.30 and 4.31. Less compressible medium tends to build-up pressure faster than te medium with the higher compressibility. Early pressure build-up leads to early fracture growth

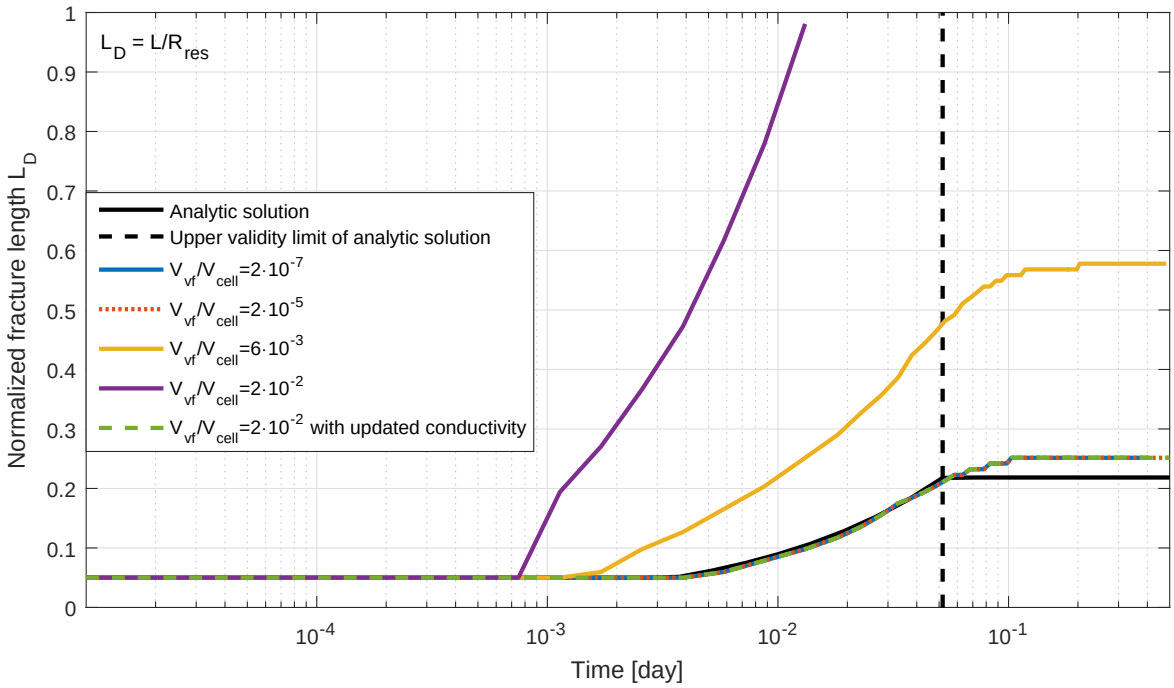

Figure 4.26: Fracture length comparison in the variation of "virtual" fracture segment aperture study for the model with the average mesh size equal to 1.0 m and the adaptive time step. Increase of the volume ratio $\frac{V_{\text{vf}}}{V_{\text{cell}}}$ above the default one ($2 \cdot 10^{-5}$) without increasing the corresponding conductivity leads to premature fracture initiation and larger final solution. Corresponding increase of the ratio $\frac{V_{\text{vf}}}{V_{\text{cell}}}$ and the conductivity maintain the solution unaffected.

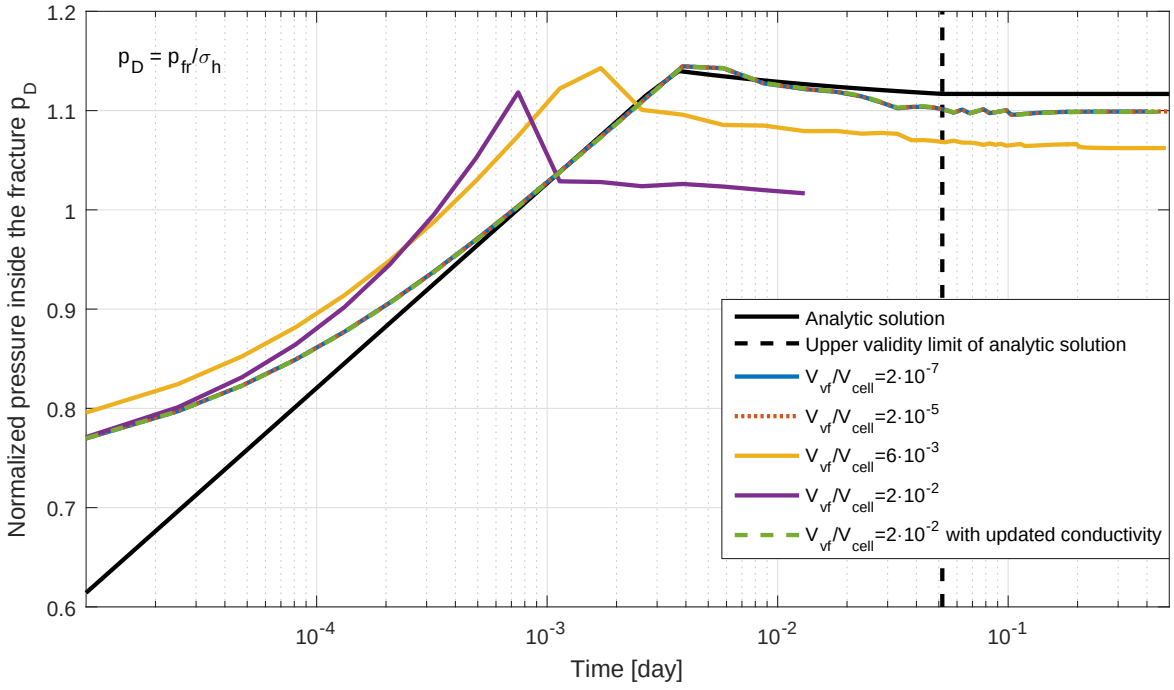

Figure 4.27: Pressure inside the fracture comparison in the variation of the "virtual" fracture segment aperture study for the model with the average mesh size equal to 1.0 m and the adaptive time step. Earlier pressure build-up is caused by the increase in $\frac{V_{\text{vf}}}{V_{\text{cell}}}$ ratio without upscaling the conductivity.

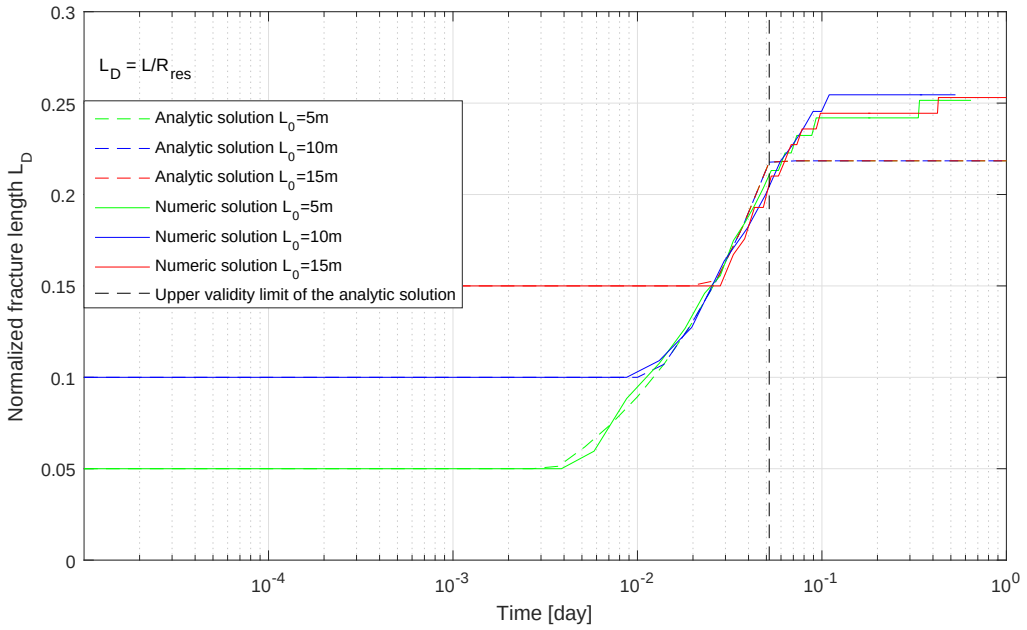

Figure 4.28: Fracture length comparison in the variation of the initial fracture length for the model with the average mesh size equal to 1.0 m and the adaptive time step. Increase of the initial length leads to later fracture growth initiation. All the solutions fit the analytical length prediction in its validity range.

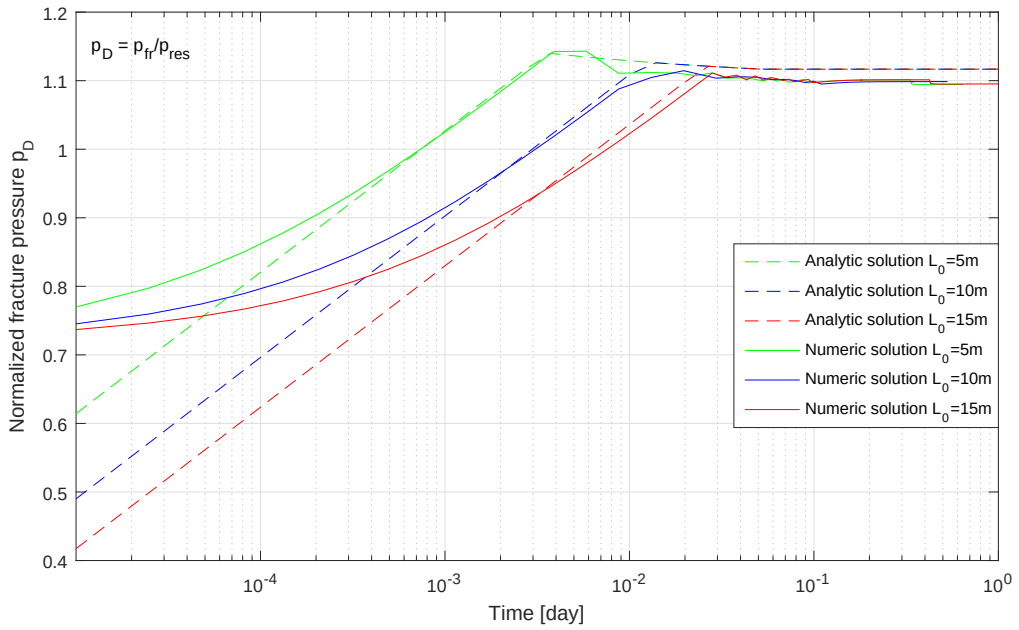

Figure 4.29: Pressure inside the fracture comparison in the variation of the initial fracture length for the model with the average mesh size equal to 1.0 m and the adaptive time step. Longer initial length leads to slower pressure development. After reaching the critical pressure value, fracture starts propagating and pressure solutions for different initial lengths merge.

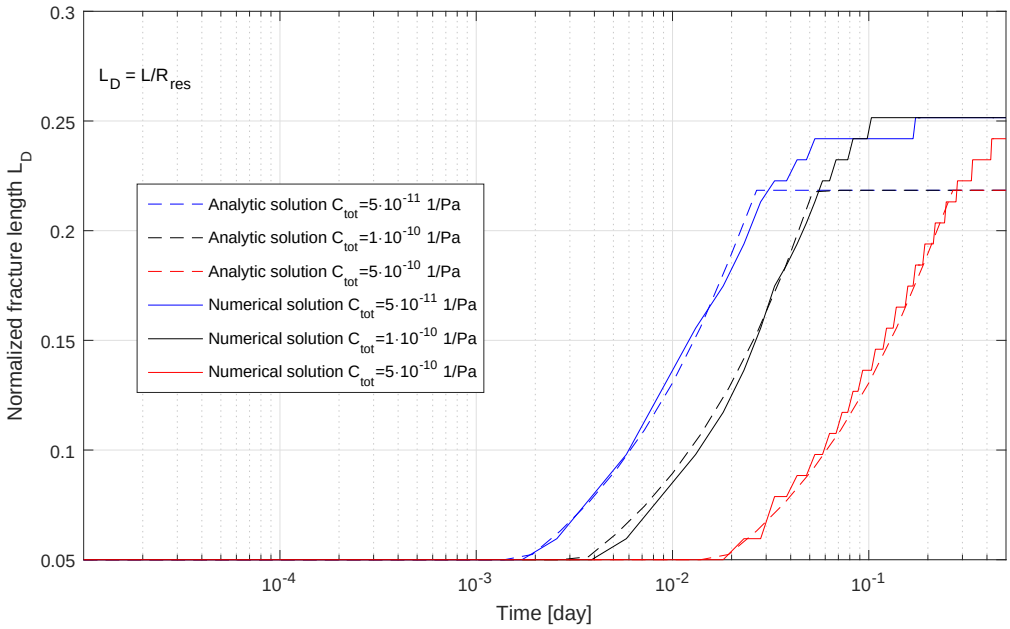

Figure 4.30: Fracture length comparison in the variation of the total system compressibility C_t for the model with the average mesh size equal to 1.0 m and the adaptive time step. Reduction of the compressibility (blue curve) leads to early fracture growth in comparison with more compressible systems. All the solutions fit the analytical length prediction in its validity range.

initiation. All the solutions for pressure and fracture length fit their analytical analogues in their ranges of validity.

4.4.6. Effect of the Fracture Toughness Value K_{Ic}

Rate of the fracture growth as well as its final length are controlled by the fracture toughness value K_{Ic}. The higher this value, the higher should be concentration of stresses at the tip for the fracture to propagate. Lower values of K_{Ic} require less effort for the fracture to grow and the final length becomes larger. To demonstrate the sensitivity of the developed model to the fracture toughness, 3 simulations with $K_{\mathrm{Ic}} = 1, 3$ and 5 MPa·m$^{0.5}$ were conducted. Results for the fracture length and pressure are given in figures **??** and **??**. Numerical model is capable of capturing the effect of K_{Ic} on the dynamics of the fracture growth. Numerical solution is matching the analytical curves within their validity range.

4.4.7. Effect of the Fracture Path Tortuosity

In the previous examples, fracture was developing along the horizontal line, defined in the geometry (see figures 4.4a and 4.5a). In this subsection, tests are done on geometries where no such "comfortable" path exists. Fracture growth was simulated on four geometries with different average mesh size. The sizes are 0.25 m, 0.5 m, 1.0 m and 2.0 m. All simulations were done with the adaptive time step starting with $1 \cdot 10^{-5}$ day and ending with $5 \cdot 10^{-3}$ day. Resulting fracture geometries are given in figure 4.34. Development of fracture length and pressure is shown in figures 4.35 and 4.36.

From analysis of figure 4.34, conclusion is made that for denser mesh, fracture trajectory tends to become more horizontal. In case of coarser mesh, deviation from the horizontal path is more significant. In figure 4.35, we can see that the large mesh size (green line) has larger deviation from the analytic curve. Similar behavior was observed in the case with horizontal path for

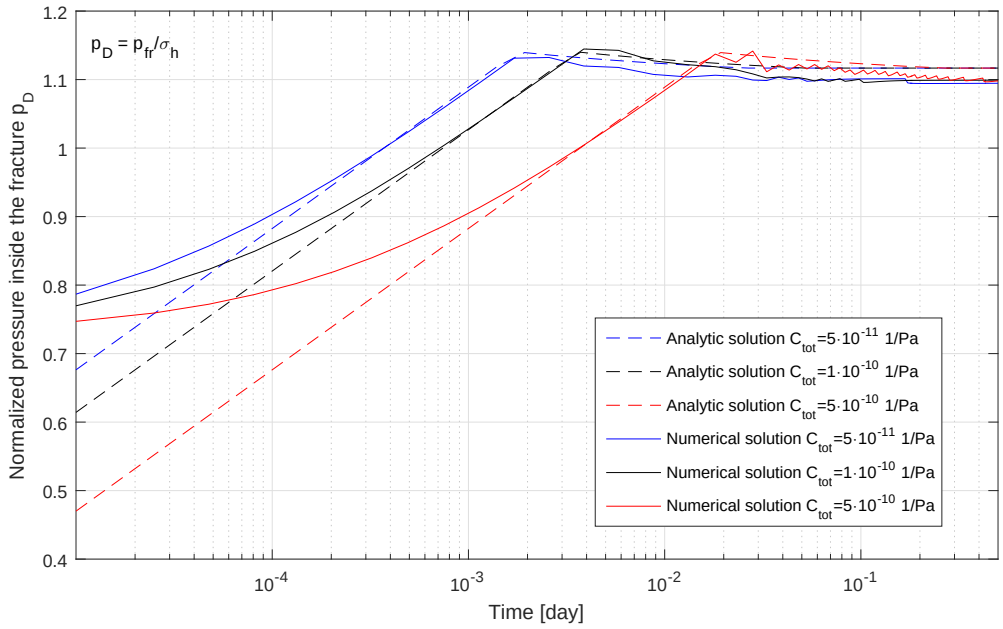

Figure 4.31: Pressure inside the fracture comparison in the variation of the total system compressibility C_t for the model with the average mesh size equal to 1.0 m and the adaptive time step. Less compressible media develops pressure inside faster than its more compressible analogue.

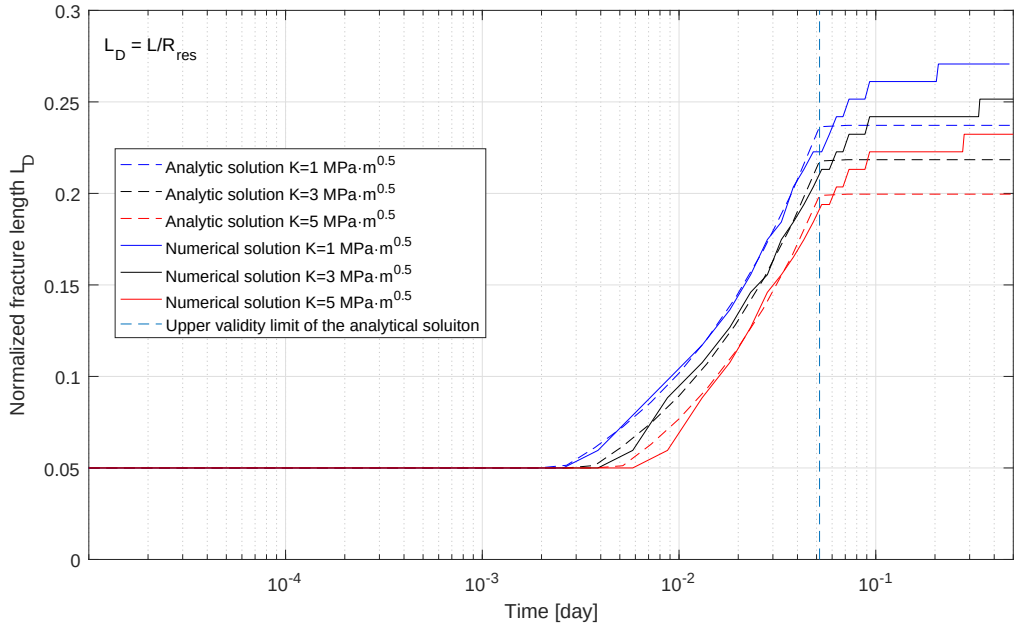

Figure 4.32: Fracture length comparison in the variation of the fracture toughness value K_{Ic} for the model with the average mesh size equal to 1.0 m and the adaptive time step. Higher value of K_{Ic} leads to later fracture growth initiation. It also leads to shorter fracture in final solution.

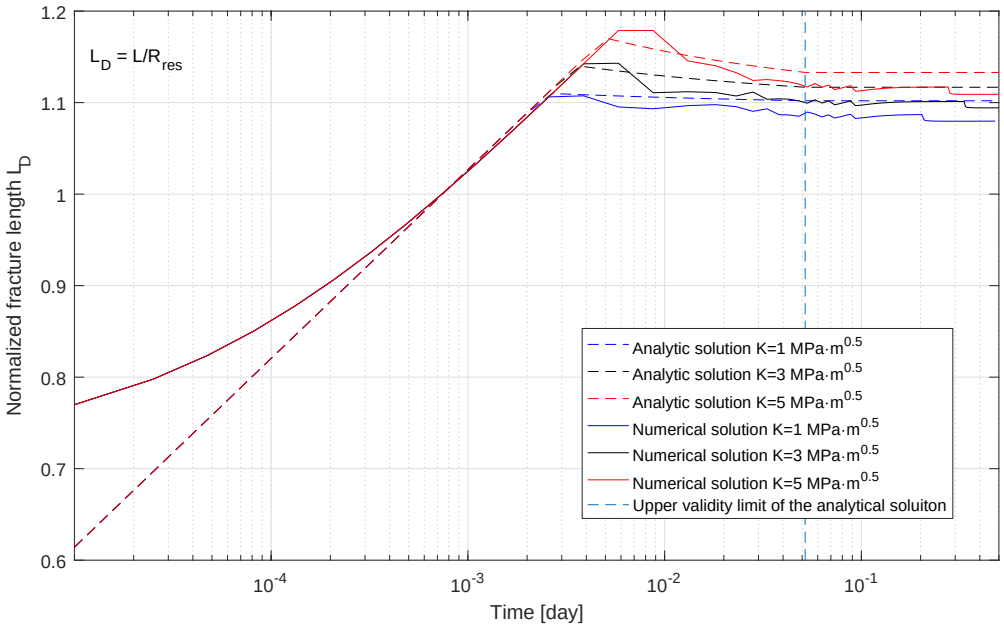

Figure 4.33: Pressure inside the fracture comparison in the variation of the fracture toughness value K_{Ic} for the model with the average mesh size equal to 1.0 m and the adaptive time step. Higher K_{Ic} value leads to later initiation of the fracture growth. The pressure peak also displaces further in time.

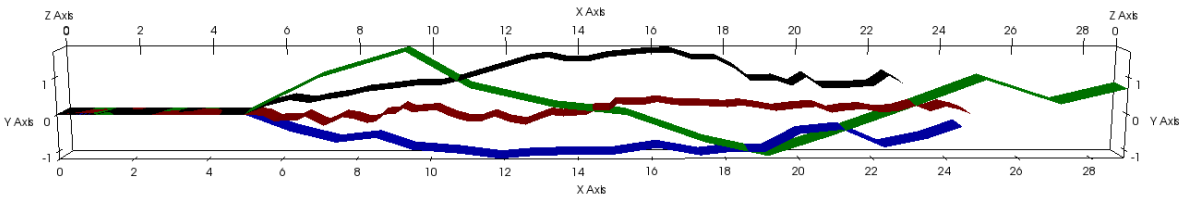

Figure 4.34: Fracture path for geometries with no horizontal line in front of the initial fracture. Red line corresponds to the average mesh size of 0.25 m, black line - to the mesh size of 0.5 m, blue line - to the mesh size of 1.0 m and green line - to the mesh size of 2.0 m.

the fracture (see subsection 4.4.1 and figure 4.20). The rest of the meshes (0.25 m, 0.5 m and 1.0 m) give length solutions very close to the analytic curve. Pressure growth given in figure 4.36 shows behavior similar to the solution obtained on the meshes with horizontal fracture path (figure 4.21). Pressure has larger fluctuations upon opening of new segments for meshes with larger average element size. Shown study demonstrates applicability of the proposed algorithm for the class of problems where fracture path is straight.

4.4.8. Effect of the Stress Anisotropy Level on Turning Fracture

All previous examples of growing fracture were modeled in anisotropic stress field where initial fracture direction coincided with the direction perpendicular to the minimum horizontal stress σ_h. Therefore, fracture grew straight. In the current series of experiments, the stress field was turned $90°$, forcing the fracture to change its initial direction. 3 stress fields with different anisotropy were modeled. Following ratios between minimum and maximum horizontal stresses σ_h/σ_H were employed $1:1.05$, $1:1.075$ and $1:1.1$. Tests were done on domains with 3 different average mesh sizes: 1.25, 2.5 and 5.0 m. Results are given in figure 4.37.

In figure 4.37, we see that the proposed algorithm allows for fracture re-orientation in space. Additional to that, the numerical scheme is sensitive to the level of stress anisotropy. Model

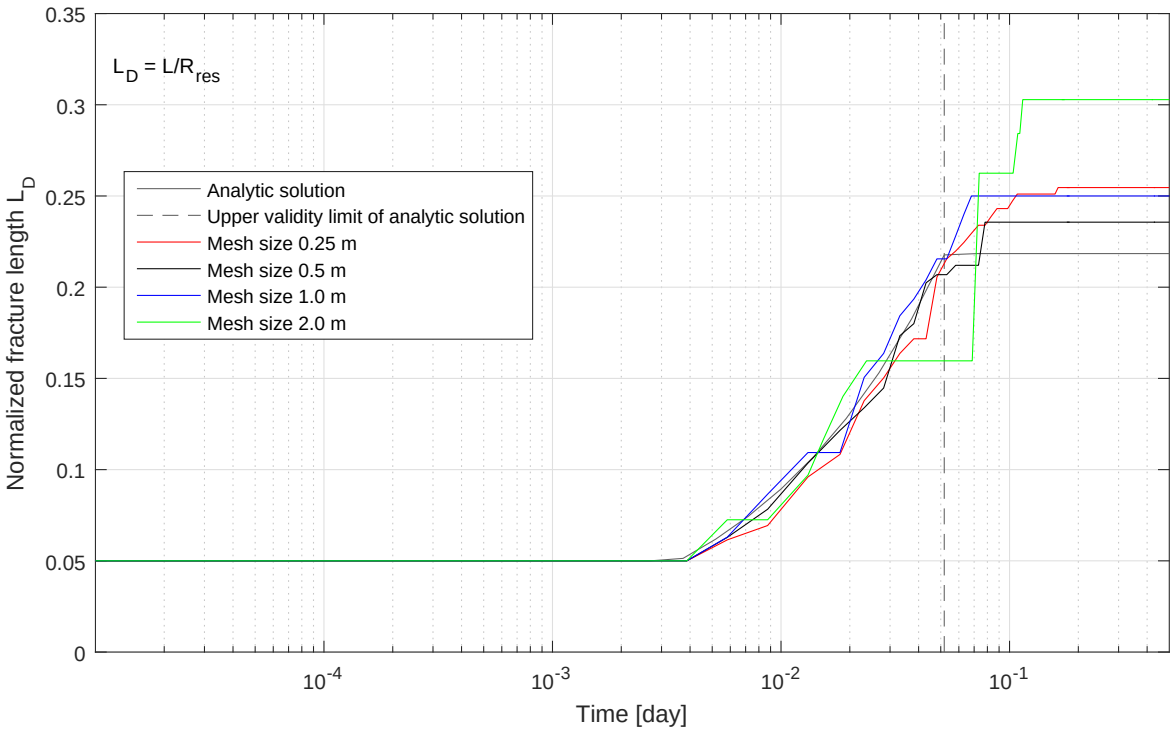

Figure 4.35: Comparison of fracture lengths in time for meshes without horizontal path for the fracture. The largest mesh size shows overshoot in length and non-smooth growth in time. Denser meshes have better agreement with analytic curve and variation of the final length in the range of 3%.

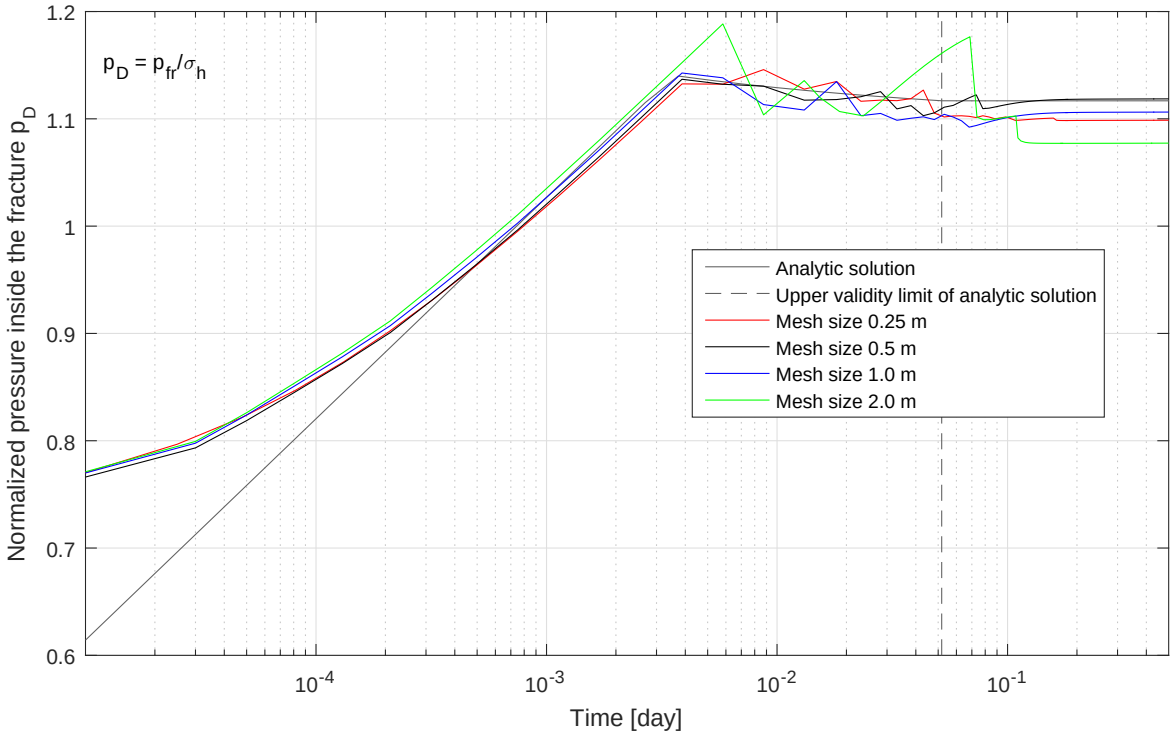

Figure 4.36: Pressure development for meshes without horizontal path for the fracture. Solution obtained on the larger mesh size exhibit higher pressure fluctuations upon opening of new segments.

with only 5% of anisotropy shows smooth fracture turning, while larger values of anisotropy (7.5% and 10%) make fracture turn under a more acute angle to the initial direction right from the beginning. However, difference between fracture trajectories calculated on meshes with different average size is apparent. In contrast to straight fracture, results of simulations for turning fracture are rather qualitative. The reason for that is the disturbance of the stress field around the crack tip, which is caused by finite size of the elements at the tip as well as their size ratio.

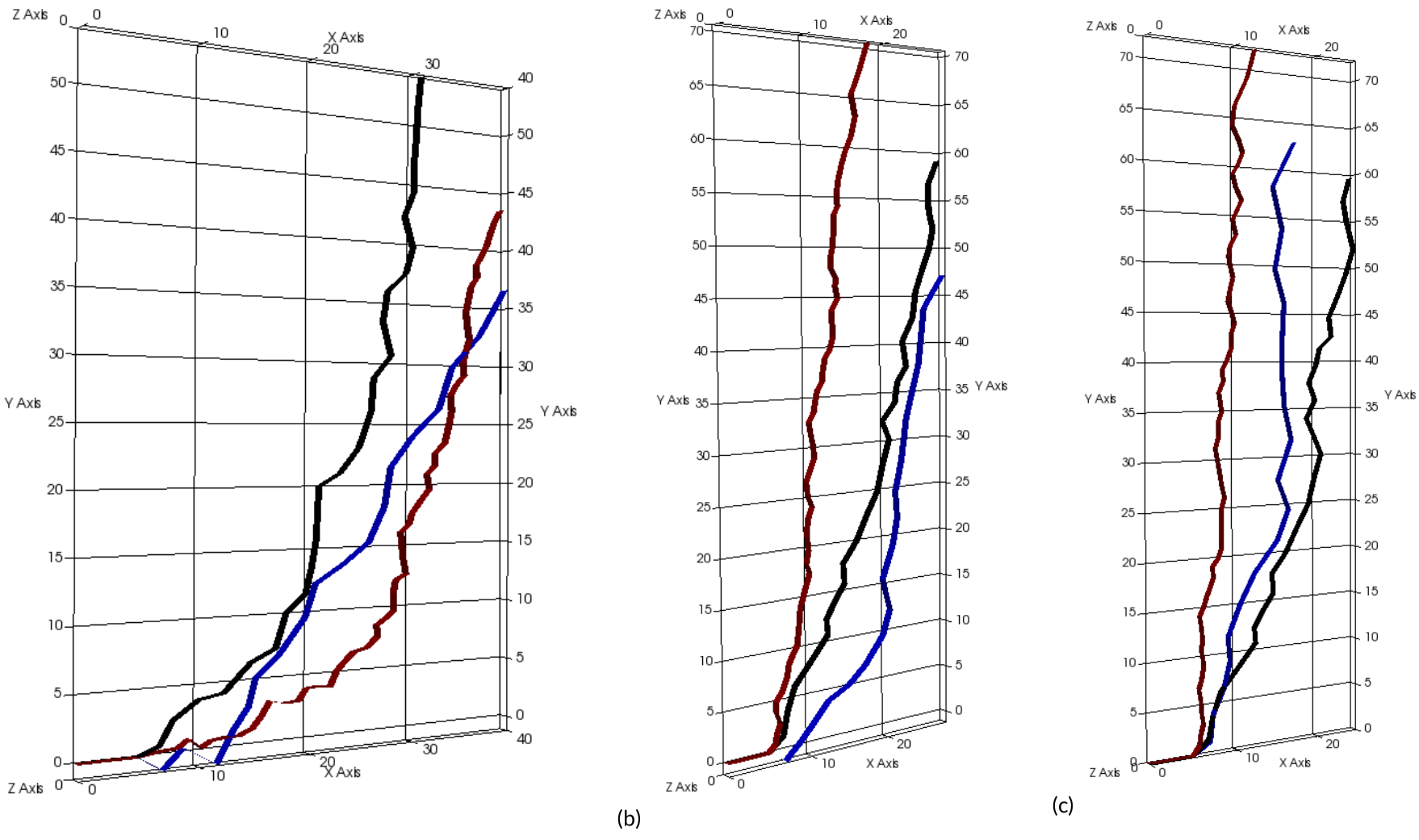

Figure 4.37: Turning fracture trajectory for anisotropic stress fields with ratios σ_h/σ_H equal (a) $1:1.05$, (b) $1:1.075$ and (c) $1:1.1$. Red line corresponds to the average mesh size of 1.25 m, black line - to the mesh size of 2.5 m, blue line - to the mesh size of 5.0 m. 5% value of anisotropy (a) is characterized by smoother turning profile, than 10% of anisotropy (c), where fracture turns under angle close to $90°$ right from the beginning.

5

Application

The purpose of this chapter is to demonstrate the applicability of the developed model to practical tasks. The specific problem that we solve is to model the hydraulic fracture growth during waterflooding operations within a classical injection pattern.

The waterflooding operation aim is to increase the recovery of hydrocarbons by displacing them by injected water. Different injection patterns are employed for such operation. Here we consider one the most commonly used patterns called an inverted nine-spot. This injection pattern is a specific design of the reservoir development plan, where water is injected into a well surrounded by 8 producing wells. Schematics of this pattern is given in figure 5.1a. It is adopted on many oil & gas fields worldwide due to its high extraction rates and coverage ratio, and therefore, maximum Net Present Value and Oil Recovery Value. One of the places where such injection pattern is successfully employed is Priobskoye field in Western Siberia, Russia. Priobskoye is the second by amount of geological reserves field in Russia, after Samotlorskoye field.

In the oil fields of Western Siberia with low permeable producing rock, hydraulic fracturing is a common practice of increasing oil recovery [65]. Likewise, hydraulic fracturing is widely used in Priobskoye field [99]. Half-lengths of stimulated fractures are reaching $150 - 200$ m. After injection starts, a waterflood-induced fracture grows as a continuation of an existing hydraulic fracture. Half-lengths of such fractures may reach $350 - 400$ m and lead to a 100% watercut at producing wells. In order to avoid this situation, a reservoir development plan should be designed, considering waterflood-induced fractures. Specific parameters which could be optimized are distances between wells, intensity of hydraulic stimulation, injection and extraction rates. To illustrate the effect of early watercut and show the importance of including waterflood-induced fractures into a reservoir development plan, we setup the following synthetic problem.

5.1. Model description

Here we model a waterflood-induced fracture in a limited section of the injection pattern. The considered region is limited by the dashed line in figure 5.1a and comprises one injecting well and three producers. Induced hydraulic fractures are oriented in the direction perpendicular to the minimum horizontal stress σ_h with small deviations of $\pm 8°$. Lengths of induced fractures are contained in the region $200 - 300$ m for a whole 2-winged fracture. In order to simplify the generation of the model input files, boundaries of the modeled region are co-oriented with the principal stresses directions. The simulated domain and its boundary conditions for mechanics are given in figure 5.1b. To reduce the size of the discrete model, only half-space is considered. The symmetrical boundary condition is imposed at $x = 0$ m. The model is compressed by the

horizontal stresses, $\sigma_x = 386 \cdot 10^5$ Pa and $\sigma_y = -360 \cdot 10^5$ Pa. The displacement in Z direction is restricted for every node. The computational domain is defined by $\Omega = [900 \times 920 \times 1\text{m}]$. The mesh with the average size of elements equal to 10 m in the center and 100 towards the boundaries was employed. The matrix is discretized using $9,990$ tetrahedral elements ($10,052$ vertices). The fractures are discretized by $11,695$ rectangles. The total number of control volumes is $21,685$. Initial conditions for the mechanical part correspond to the stresses applied at the boundaries. Flow domain is surrounded by impermeable boundaries. The initial reservoir pressure equals to $p_r = 200 \cdot 10^5$ Pa. The fluid is injected with the rate Q_{inj}. Full recovery is ensured by extracting from 3 wells with the production rate of $Q_{ext} = Q_{\text{inj}}/3$ per each well. As we are modeling a 2D case, but the numerical domain has a third dimension equal to 1, injection flow rates are given per unit height of the reservoir, and the unit for it is m^3/day/m. Conductivity of the fractures is sensitive to the stress field and will change during operations. Conductivity values corresponding to the Barnett shale were adopted from [118]. They are plotted as a function of the normal traction and aperture in figure **??**. The curve in the left part of the figure is plotted against the normal fracture aperture, while in the right part it is plotted against normal traction on a fracture face. Reduction in compression between faces and following opening of the fracture leads to the increase of its conductivity. Properties of the rock, injected and extracted fluids, as well as the operational parameters are provided in table 5.1.

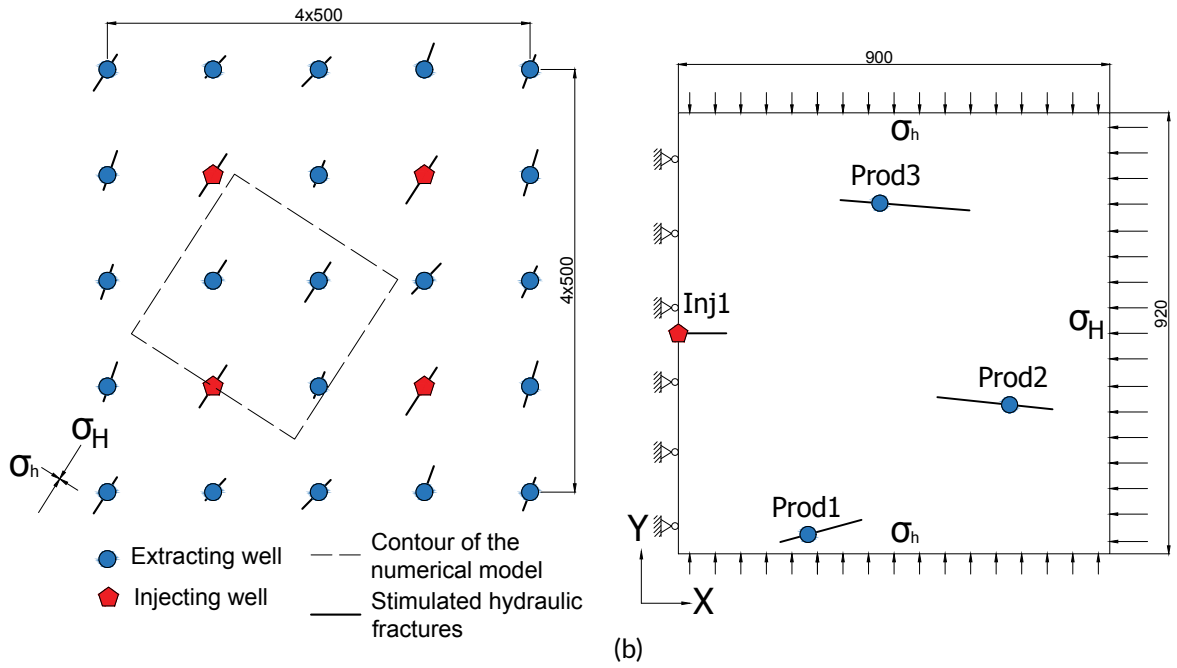

Figure 5.1: (a) Inverted nine-spot injection pattern. (b) Simulated part of the pattern with boundary conditions for mechanical part. Hydraulic boundary conditions are no flow through its sides.

5.2. Results

Two typical waterflooding scenarios are considered. The first behavior is characterized by no induced fracture. This typically happens when the injection flow rate is low. The second behavior is an induction of fracture growth by the injection of water under a high rate. Even for the no-induced-fracture case, including the geomechanics into simulation is important. It allows predicting conductivity changes of both stationary crack and porous media. Observation

Table 5.1: Fluid and rock properties used in the practical example

Rock properties and stresses	
Matrix porosity ϕ	0.2
Matrix permeability k, mD	5
Density ρ_r, kg/m^3	2500
Biot modulus α	1
Young's modulus E, Pa	$2 \cdot 10^{10}$
Initial reservoir pressure p_r, Pa	$200 \cdot 10^5$
Poisson's ratio ν	0.25
Compressibility C_r, 1/Pa	$1 \cdot 10^{-10}$
Cohesion c, Pa	$1 \cdot 10^{10}$
Friction angle φ, °	0
Dilation angle ψ, °	0
Total horizontal stress σ_x, Pa	$-386 \cdot 10^5$
Total horizontal stress σ_y, Pa	$-360 \cdot 10^5$
Rock temperature T_r, °K	373
Fracture toughness K_{Ic}, Pa$\sqrt{\mathrm{m}}$	$30 \cdot 10^5$
Fluid properties	
Oil density ρ_o, kg/m^3	1000
Water density ρ_w, kg/m^3	1000
Oil viscosity μ_o, cP	0.5
Water viscosity μ_w, cP	0.2
Oil compressibility C_o, 1/Pa	$5 \cdot 10^{-10}$
Water compressibility C_w, 1/Pa	$4 \cdot 10^{-10}$
Connate water saturation $S_w r$	0.25
End-point relative permeability of oil k_{ro}	0.8
End-point relative permeability of water k_{rw}	0.8
Mobility ratio M	2.5
Injected water temperature T_w, °K	373

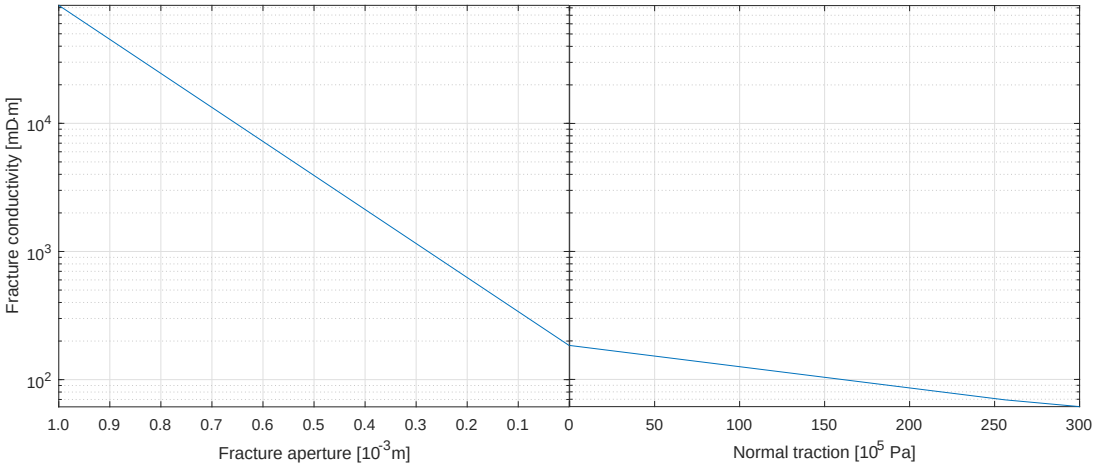

Figure 5.2: Fracture conductivity as a function of its aperture (left part) and normal traction (right part)

and comparison of two numerical simulations corresponding to the two typical behaviors during the waterflooding operation are given.

The first typical behavior was achieved in the numerical simulations with the water injection rate $Q_{\text{inj}} = 9$ m^3/day/m. Pressure and water saturation profiles after 3 years of simulation time are given in figure 5.3. Pressure increase along the existing hydraulic fracture connected to the injection well is much more pronounced than the pressure drop on wells-producers. The reason behind is the aperture dependent fracture conductivities. As the injection well tends to "blow-up" the neighboring fracture, compression of the fracture tends to decrease leading to increase in its conductivity. In contrast, producing wells reduce the pressure in their neighborhood, which leads to the increase of the normal traction on the neighboring fracture faces. As a result, conductivity of fractures at producing wells reduces. Waterflood front, given in figure 5.3b, still does not reach any of the producing wells after 3 years. Smeared water saturation front corresponds to the unfavorable displacement type, indicated by the mobility ratio $M > 1$ (see table 5.1).

Pressure dynamics at each well is given in figure 5.4a. Bottom Hole Pressure (BHP) at the injector grows intensively during the first 200 days after which it stabilizes. The maximum value of pressure stays close to $1.08\sigma_h$ which is not enough to overcome the sum of the minimum horizontal stress σ_h, the poro-elastic component $\Delta\sigma_p$, and the contribution from fracture toughness K_{Ic}. Therefore, the fracture does not propagate. Pressure profiles at two of the producing wells have a decrease after 2300 days. The reason for such behavior is the water breakthrough which is clearly seen in figure 5.4b. Here, the collective water production from 3 wells is given. It is normalized over the volume of the injected water. Water breaks at 2300 days which is distinguished by a steep increase in the produced water volume.

The next typical waterflooding behavior is the one with the growing hydraulic fracture. As an illustration, results of the simulation with the injection rate $Q_{\text{inj}} = 21$ m^3/day/m are investigated. Pressure and water saturation profiles across the domain after 3 numerical years are given in figure 5.5. In comparison to the stationary fracture case, pressure and water saturation front advanced on a larger distance owing both to a conductive path created by the fracture and the higher value of injection rate.

Dynamics of the Bottom Hole Pressure at the injection well and the fracture length is given in figure 5.6a. Here, pressure increases above the critical stress[1], which makes propagation pos-

[1] which approximately equals to $1.12\sigma_h$

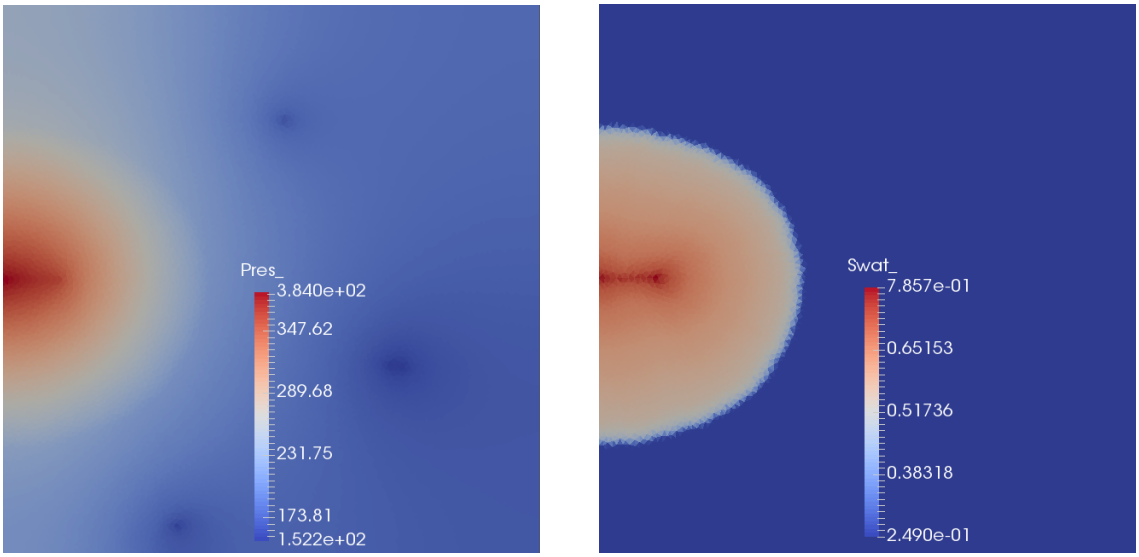

(a) (b)

Figure 5.3: (a) Pressure and (b) water saturation profiles across the domain in the simulation with $Q_{\text{inj}} = 9$ m^3/day/m after 3 years. Water front yet didn't reach any of the producing wells.

sible. Unlike the stationary fracture case, the pressure profile for growing crack has fluctuations associated with openings of fracture segments. Crack, which initiates with the length of $\frac{1}{4}W$ [2], develops dimensions even larger than W. Water production history is given in figure 5.6b. Water breaks after 900 days.

In order to compare two typical behaviors irrespective of time, variables are plotted against volume of the injected water normalized by the displaceable pore volume of the domain $\frac{V_{\text{injw}}}{V_{\text{dpor}}}$. The ratio $\frac{V_{\text{injw}}}{V_{\text{dpor}}}$ shows the fraction of the total available pore volume already displaced by water and serves as the indicator of the waterflooding progress. Normalized BHP curves at the injecting well for two simulations are plotted against $\frac{V_{\text{injw}}}{V_{\text{dpor}}}$ in figure 5.7a. Pressure curve for stationary fracture case stays below the similar curve for growing fracture during the whole simulation. The critical pressure value after which the fracture starts growing is found in-between these two curves. Normalized volume of the produced water for two simulations is given in figure 5.7b. If the hydraulic fracture is induced, less injected water is needed to cause the water breakthrough. This statement holds for these specific injection rates and the current domain.

In order to identify patterns in behavior of pressure, length and water breakthrough initiation, 4 more simulations were performed. Their injection rates are $Q_{\text{inj}} = 5$, 7, 14, and 28 m^3/day/m. Data from all 6 simulations is plotted together. Profiles of the BHP at the injector for all 6 simulations are given in figure 5.8. Increase in the injection rate leads to a higher pressure level. After a rapid pressure growth during injection of the first 2% of the displaceable pore volume, the pressure value stabilizes. When pressure exceeds the critical value (approximately $1.1\sigma_h$), the fracture starts to grow. It is important to mention that for a propagating fracture, BHP does not vary significantly for different injection rates.

Dynamics of the fracture length is shown in figure 5.9. The figure reveals that the growth rate is directly dependent on the injection rate. Similar to the pressure behavior, the most in-

[2] W is the shortest distance between two neighboring wells

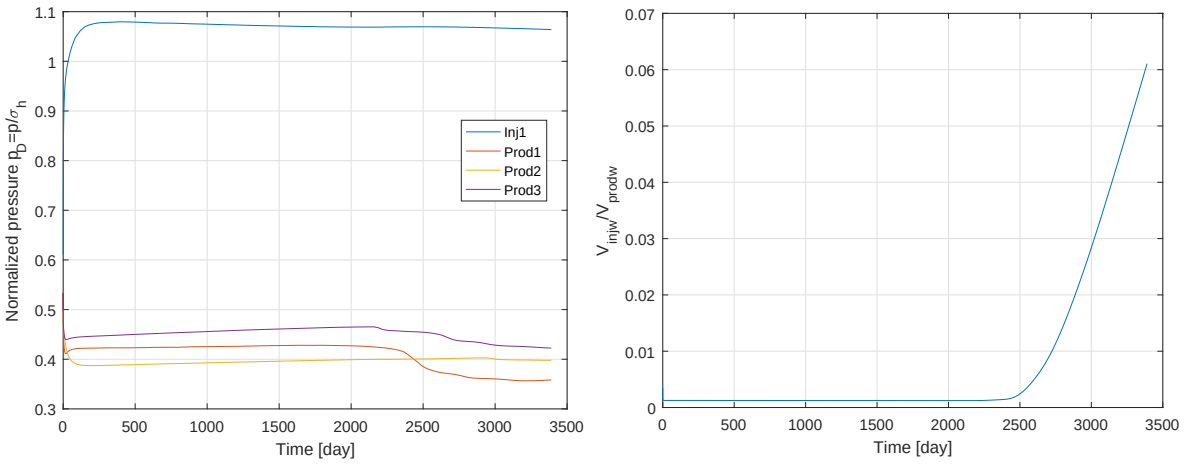

(a) (b)

Figure 5.4: Dynamics of (a) the Bottom Hole Pressures and (b) the produced water volumes throughout the simulation with $Q_{\text{inj}} = 9$ m^3/day/m. Values of the BHP at every well are normalized with respect to the minimum horizontal stress σ_h. The cumulative volume of water produced by 3 wells Q_{prodw} is normalized by the cumulative volume of the injected water Q_{injw}.

tensive fracture growth fall on the displacement of the first 2% of the total volume. Assessment of figures 5.8 and 5.9 shows that, although the BHPs at the injector are very similar during the crack growth, corresponding lengths can differ at times. One conclusion is that during the waterflooding operation, controlling only the injection pressure is not sufficient for having control over the induced fracture length.

Water production in time is given in figure 5.10. It is clear that higher injection rates are leading to earlier water breakthrough. However, this information is not sufficient to evaluate efficiency of the waterflooding operation. For this, production volumes should be plotted with respect to the injected volumes.

Figure 5.11 gives the volume of the produced water with respect to the volume of the injected water. It is seen that, when no fracture is induced, water production curve is the same for all the flow rates (5, 7 and 9 m^3/day/m). In contrast, the growing fracture changes the waterflooding performance. In this particular case, development of the fracture with $Q_{\text{inj}} = 14$ m^3/day/m leads to a more effective operation and later water breakthrough than in case where no fracture is induced. However, a further increase of injection rate leads to a water breakthrough happening earlier, like in case of $Q_{\text{inj}} = 14$ m^3/day/m.

In addition, scenarios with $Q_{\text{inj}} = 14$ and 21 m^3/day/m were simulated on two different meshes with average size equal to 5 and 10 m. Comparison of the solutions for length is given in figure 5.12. Results show good agreement in each pair of curves.

5.3. Summary

The developed model is of great value for this specific application. Results of the simulations reveal the nature of the waterflooding process. Evolution of pore pressure and stress fields, growth of water saturation front and variation of the rock conductivity are only few among many other features traced by the model. Properties of both stationary and growing fracture can be accurately predicted. For a stationary crack, these properties include aperture, traction and conductivity. For a growing fracture, the list is extended to include the crack length, growth rate, critical stress necessary for propagation, etc. In addition, it allows accounting for the properties of the injected proppant and dependency of fracture conductivity on stresses.

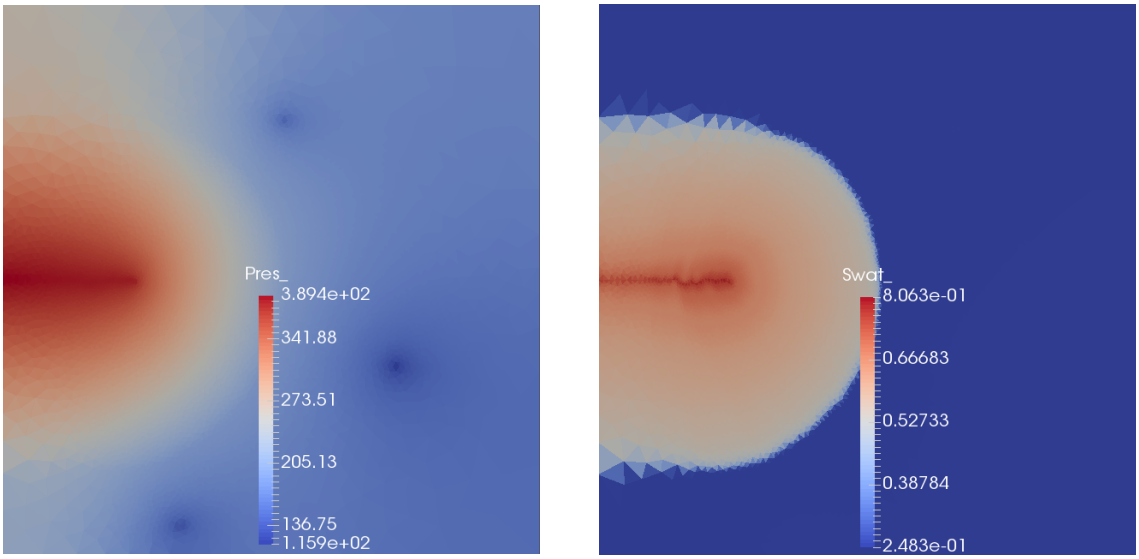

(a) (b)

Figure 5.5: (a) Pressure and (b) water saturation profiles across the domain in the simulation with $Q_{\text{inj}} = 21$ m^3/day/m after 3 years. The pressure and water saturation front follow advancing fracture.

The employment of the developed model to design waterflooding operations is advantageous. Based on the predicted final fracture length and the water breakthrough time, well plan and the injection pattern could be optimized allowing for a more cost-effective solution. The choice of operational parameters such as limiting pressures, injection and production rates could be also based on the model predictions.

From the operational point of view, the model provides key parameters such as critical injection rate and associated bottom hole pressure, after exceedance of which starts the fracture propagation. The model can also estimate the final fracture length depending on the employed injection rate.

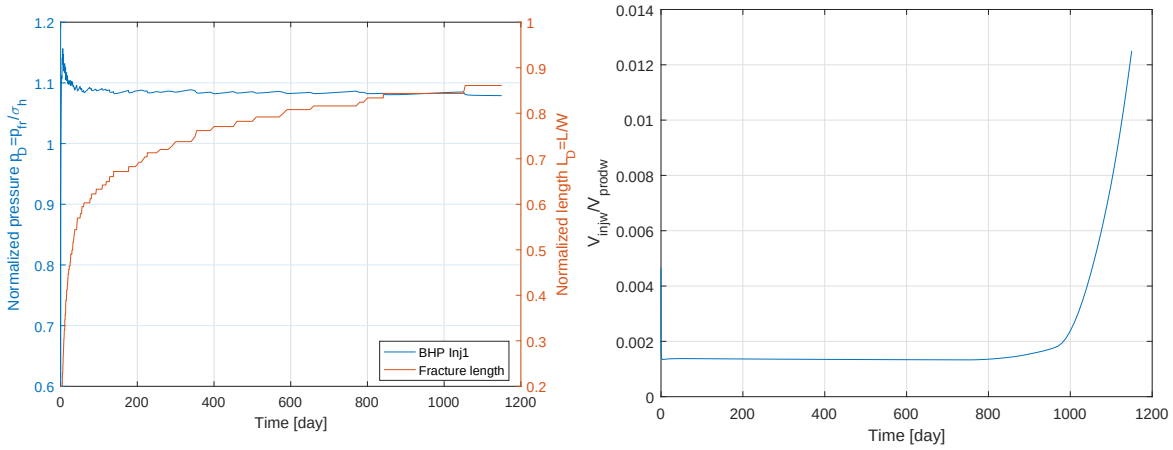

(a) (b)

Figure 5.6: Dynamics of (a) the Bottom Hole Pressure at the injector and the fracture length, and (b)the produced water volumes throughout the simulation with $Q_{\text{inj}} = 21$ m^3/day/m. Values of the BHP are normalized with respect to the minimum horizontal stress σ_h, the fracture length L is normalized by the distance between neighboring wells $W = 500$ m. The cumulative volume of water produced by 3 wells together V_{prodw} is normalized by the cumulative volume of injected water V_{injw}.

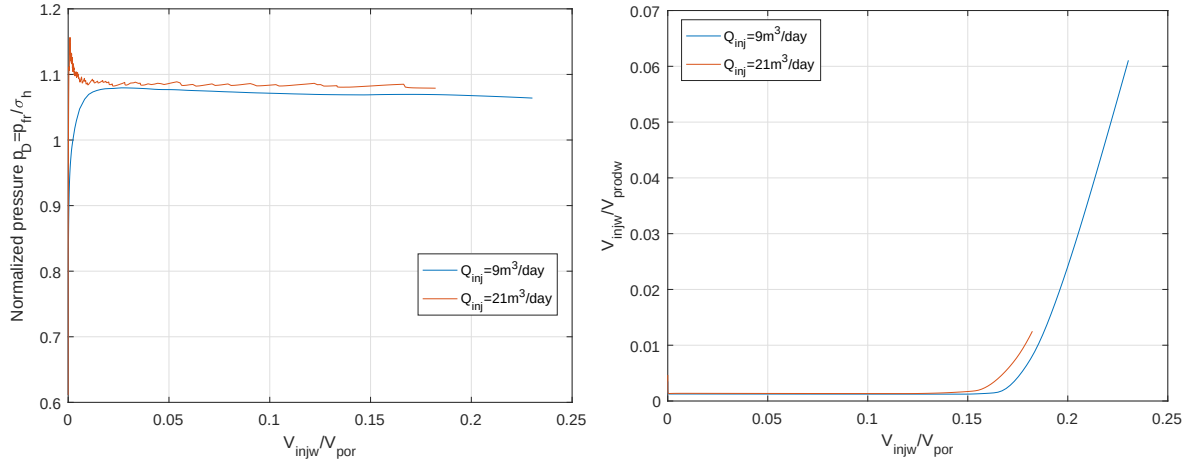

(a) (b)

Figure 5.7: (a) Normalized Bottom Hole Pressure at the injector and (b) the produced water volume for simulations with $Q_{\text{inj}} = 9$ and 21 m^3/day.

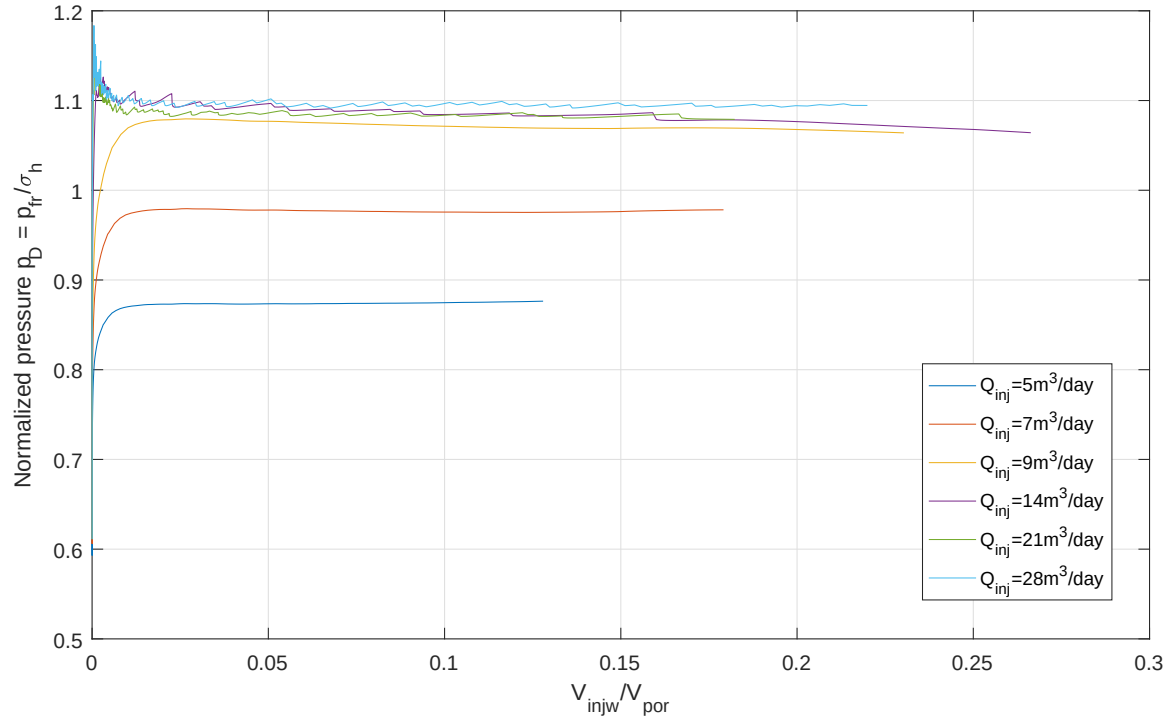

Figure 5.8: Bottom hole pressure at the injector normalized by the minimum horizontal stress σ_h against volume of the injected water V_{injw} normalized by the displaceable pore volume V_{dpor}.

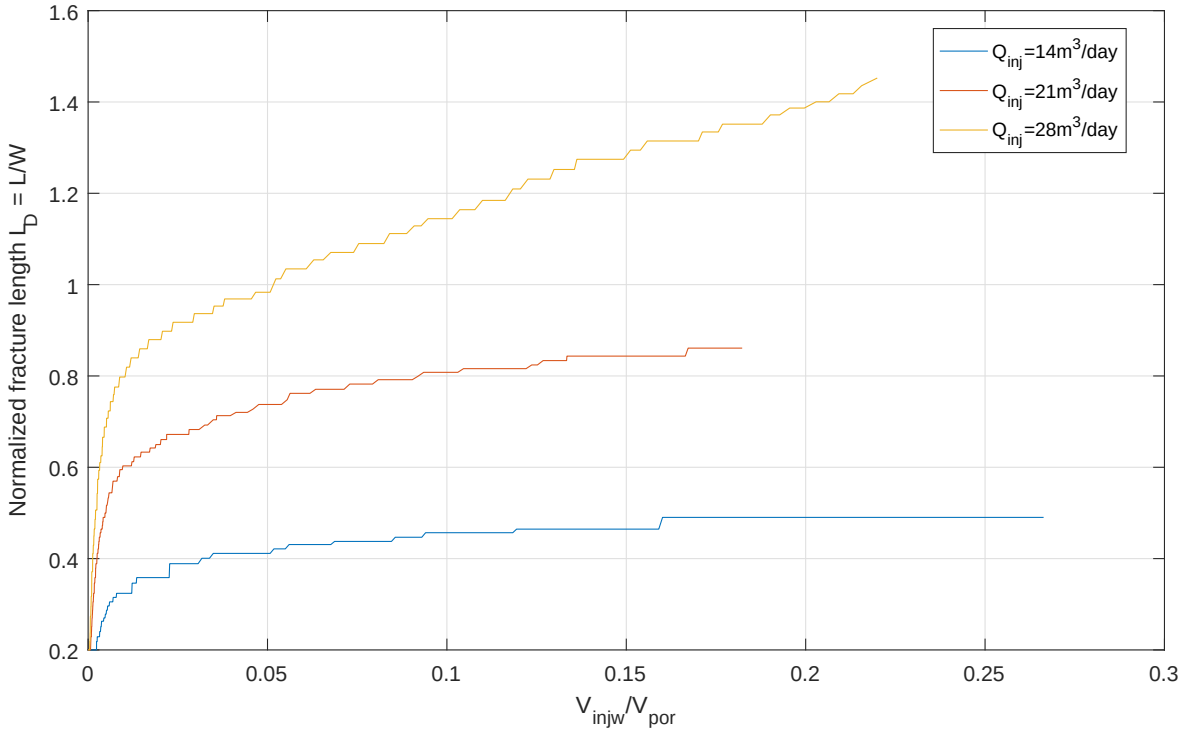

Figure 5.9: Fracture length normalized by the minimum distance between 2 wells W against volume of the injected water V_{injw} normalized by the displaceable pore volume V_{dpor}.

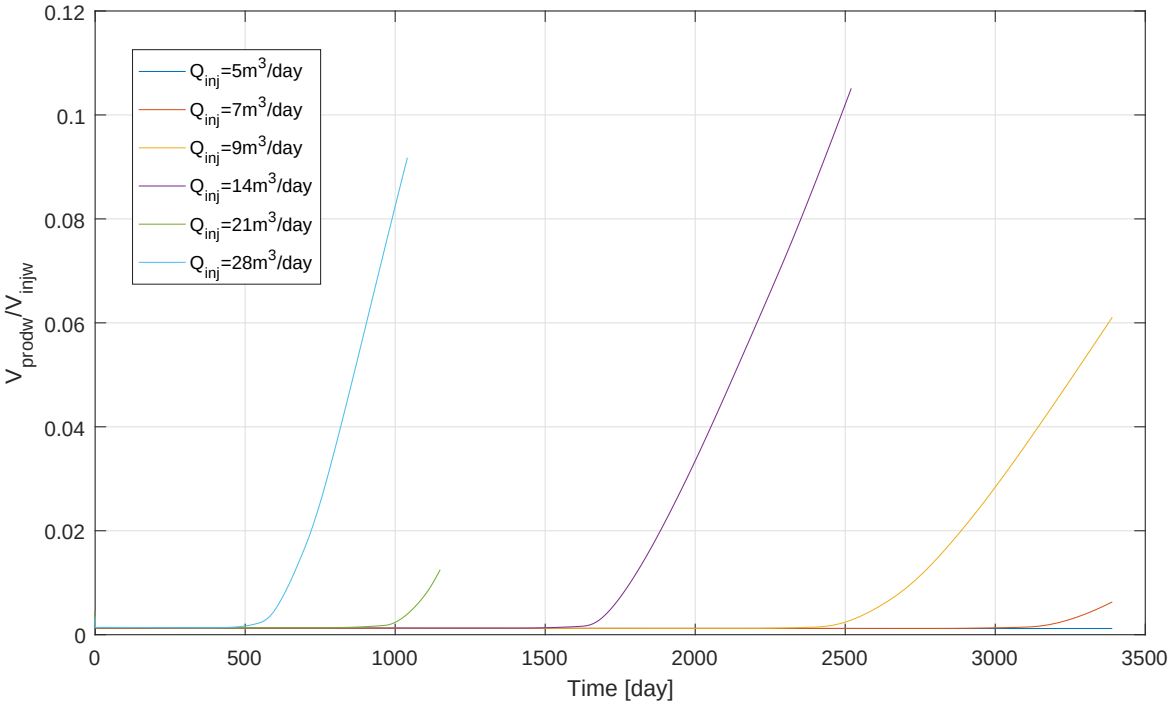

Figure 5.10: Produced water volume normalized by volume of the injected water against time

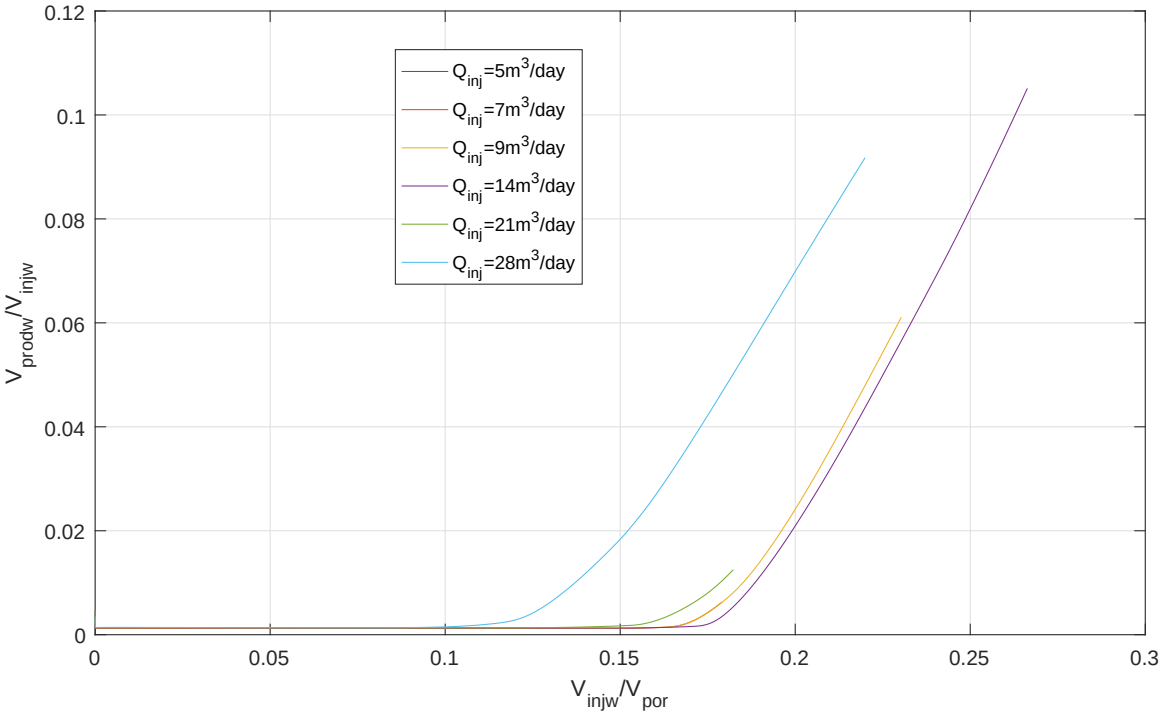

Figure 5.11: Produced water volume normalized by volume of the injected water against volume of the injected water V_{injw} normalized by the displaceable pore volume V_{dpor}.

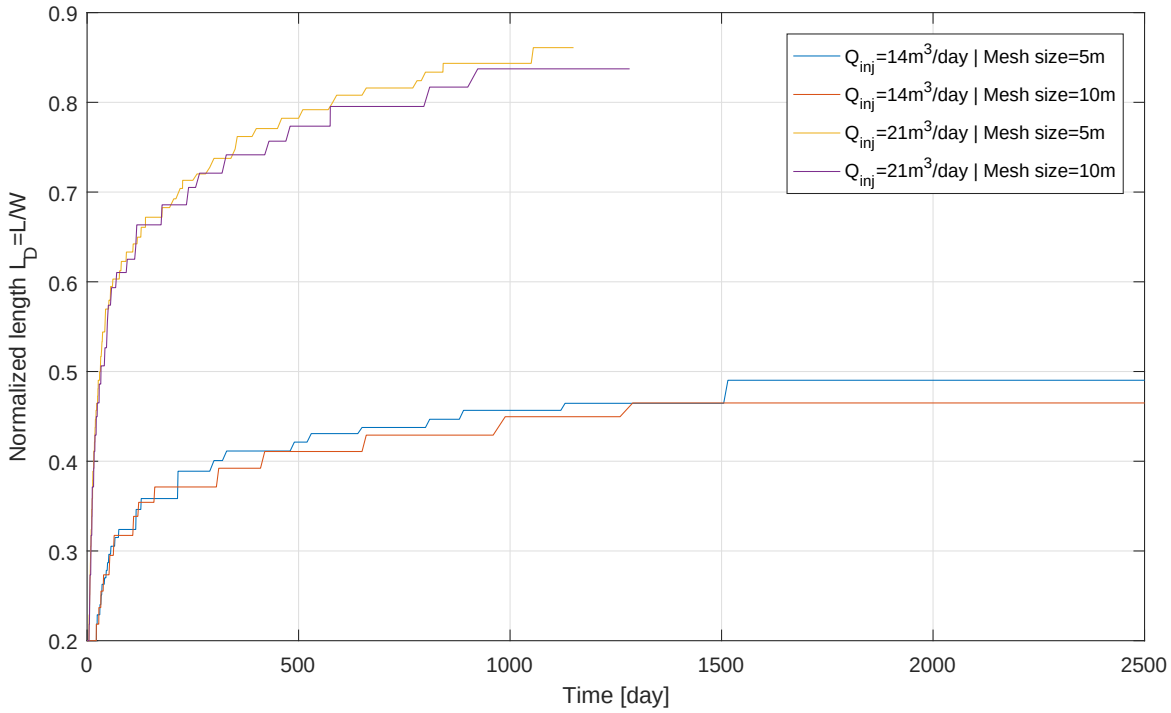

Figure 5.12: Solution for fracture length obtained on meshes with average size equal to 5 and 10 m.

6

Conclusions and Recommendations

Here, conclusions regarding the model's effectiveness, applicability and stability are presented. Further on, recommendations for the future work with the proposed method and developed code are given.

In the current thesis, the model which allows simulating the hydraulic fracturing was proposed. This model comprises a contact-enriched finite-element method for mechanics and a Discrete Fracture Model for hydraulics. Application of the proposed model was tested by producing the numerical code. Techniques adopted in this model were chosen, based on the conducted literature survey. Applicability of the proposed algorithm for a wide range of practical problems was demonstrated during the validation stage. Results obtained with the proposed model confirmed its ability to predict correctly growth of the hydraulic fracture and to capture pressure, temperature and stress changes in the domain.

6.1. Modifications to Classical DFM and FEM with Contacts

In order to enable the existing numerical solution [33] to account for growing fractures, both the hydraulical and mechanical parts were modified. Modification of the flow part comprises assigning the "virtual" fracture segments with associated finite volumes to every face shared by two neighboring cells. This operation is done only once in the beginning of the simulation. Mechanical scheme is updated upon each fracture propagation event. It is done by separation of neighboring finite elements and addition of a contact surface in-between. Proposed scheme was tested both on stationary and propagating fracture examples, showing compliance with the analytical solution. In addition, the numerical model is capable of capturing flow regimes that are not accounted for in the simplified analytical solution.

For fracture propagation, Irwin's criterion [50] for linear elastic failure of mode I $K_{\mathrm{I}} \leq K_{\mathrm{Ic}}$ is adopted. The Stress Intensity Factor is calculated by means of the displacement extrapolation technique where K-values based on a fracture opening, are extrapolated to the crack tip. Adoption of such technique enables fracture to propagate with a stable rate, independent of the average mesh size. Fracture length had the same rate of growth both for fine and coarse meshes (see figure 4.20). Results of all tested examples are in compliance with analytical solution.

Erdogan and Sih's approach for determination of the fracture propagation direction was employed [31]. Enabling the fracture to grow into direction of the maximum tensional hoop stress $\sigma_{\theta\theta}$ gave excellent results for fracture propagating straight. The model was tested on a set of random meshes without prescribed horizontal path and obtained fracture trajectories close to horizontal. It demonstrates applicability of the proposed method for a wide range of problems where no fracture turning is expected. Employment of the same criterion for turning fracture

scenarios resulted in fractures reorientation and alignment with far-field stresses. It indicates that the proposed numerical scheme is sensitive to the stress field, which is a positive indication for further research. However, trajectories of turning fractures obtained on meshes with different average sizes vary. In order to use the proposed algorithm for quantitative analysis of turning fractures, additional work on the selection of proper direction has to be done.

In order to activate more than 1 fracture segment per one time step, decision on fracture propagation/closure is taken on every Newton iteration. This is done by verifying the failure criteria and mechanical status of the last open segment. Implementation of this algorithm on each iteration permits to have as many segments open in one time step as necessary for the solution to converge. Study of the model sensitivity to time step size resulted in similar fracture growth rates in all the simulations (see figure 4.23). This example demonstrates stability of the proposed approach for problems with single propagating hydraulic fracture.

The proposed fracture opening algorithm supposes that only one segment next to the crack tip is opened per iteration. This algorithm is convenient for slow hydraulic fracturing process, typical for waterflooding operations, wastewater disposal and any other processes where single continuous fracture is developing. Stability of the numerical scheme for a single growing fracture was demonstrated in numerous test cases, both for straight and turning fractures. In order to broaden the range of applicability for tasks where multiple fractures grow, some future work is suggested.

Model sensitivity to such parameters as fluid compressibility and fracture toughness was studied as well. Increase in the compressibility led to a delay in the fracture growth, which perfectly matches physics of the process. Increase in fracture toughness K_{Ic} led to later fracture growth initiation as well as shorter final crack. Both obtained results match analytical solution.

The "virtual" fracture segment is an artificial element, that was introduced into numerical scheme in order to model fluid flow through fractured media. The effect of its volume and conductivity on the fracture pressure and length development was studied. Increase in its volume together with proper upscaling of its conductivity and transmissibility do not cause any noted effect on the solution for fracture pressure and length.

Several simulations were performed where two fluid phases were present in the domain. Reservoir simulator performed impeccably, resulting in saturation profile of water front similar to the one predicted by Welge's solution (see figures 4.7, 4.8 and 4.10). Mechanical part, in its turn, managed to capture both primary and secondary fracture growth, and fracture closure due to expansion of the flooded zone. These examples demonstrate model's sensitivity to long-term pressure variations and its ability to effectively close the fracture. One testing case was devoted to injection of cold fluid into a hot reservoir. Cooling of the reservoir by injected water led to the rock shrinkage. Resulting tensional stresses around the crack facilitated its further propagation. Apart from the primary fracture growth, numerical algorithm is capable of detecting the secondary fracturing mechanism, which causes development of thermal cracks perpendicular to the primary fracture face. Obtained results confirmed the model's ability to capture thermo-elastic effect.

The proposed model was tested on the real-life application, namely waterflooding operation. Segment of the inverted nine-spot injection pattern was simulated with different injection and production rates. In some cases, simulation resulted in no induced fractures, while in others hydraulic fracture has grown. Fracture growth rate and its final length show dependence on the injection rate. Time of the water breakthrough for different scenarios was compared. Employment of the model for this specific application could be beneficial for the waterflood design optimization and correlation with field data during operations.

Apart from the discussed application, the proposed method has great potential in the range of different problems, where single continuous straight fracture is considered. Such tasks in-

clude hydraulic fracturing due to wastewater disposal, geothermal reservoir development and any other applications where slow injection of fluid into porous media is considered. In order to widen the range of applicability as well as to improve efficiency of the model, I suggest that further work should be performed.

6.2. Future Work

The proposed fracture opening algorithm allows opening only one fracture segment next to the crack tip. It suits large number of engineering applications, mentioned earlier. Still, there are technological activities which cause simultaneous development of multiple hydraulic fractures as well as separation of one fracture into several. Such behavior is common for "fast" fractures, caused by high injection rates, where fluid losses into formation are insignificant. Typical activity is hydrofracking, where the whole network of fractures is developing. Another phenomenon, where multiple fracture growth is considered is rock shrinkage due to cooling around the primary crack. It was shown in the subsection 4.3.1 that under certain conditions, secondary cracks tend to develop from the primary crack in direction perpendicular to it. Intersection of the hydraulic fractures with the natural ones is another important process where fracture splitting may take place [12].

To enable a simultaneous growth of multiple fractures, a split of one fracture into a few or intersection with natural cracks, the proposed fracture opening algorithm should be modified. A suggested way of doing this is opening multiple segments upon meeting failure criteria at every specific location. As in the developed approach, it can be performed on every Newton iteration. Fracture propagation criteria should also be reconsidered. Estimation of Stress Intensity Factor can be complicated for multiple fracture case. Alternatively, local critical stress criteria could be employed. One of them was proposed by Erdogan and Sih [31].

Another group of tasks, where this model can be extended is applications with turning fractures. The developed algorithm is capable of capturing fracture reorientation. However, fracture trajectories obtained on different meshes have significant offset. The reason behind is the algorithm for direction selection. It is based on the value of the normal stress acting on the crack tip neighboring segments. The stress field around the tip is disturbed and not representative. One of the possible ways of improving the turning mechanism is recovery of the smooth stress field around the crack tip. That could be done by calculating principal stresses in the elements in close proximity to the crack and applying a spline function to smooth the field. The segment closest to the direction of maximum tensional stress should be opened. Another way of improvement is implementation of Sih's approach [93]. In the scope of this method, fracture propagates in the direction with minimum strain energy density. Additional calculations of strain energy density S and its first and second derivatives are necessary.

Efficiency of the proposed model could be improved by modification of the flow problem discretization. As mentioned earlier, finite volumes are assigned to every "virtual" fracture segment. This considerably increases number of variables and size of the final system of equations. In order to reduce the CPU load, finite volumes may be added dynamically upon opening of new fracture segments, similar to how contact surfaces are added into mechanical scheme. However, Discrete Fracture Model is very sensitive to volume changes and may destabilize upon increase of the system volume. The generation of new volumes for propagating fracture should be implemented in a conservative manner.

Bibliography

[1] H.H. Abass, Saeed Hedayati, and D.L. Meadows. Nonplanar fracture propagation from a horizontal wellbore: Experimental study. volume Pi, pages 589–604, 1992. URL https://www.scopus.com/inward/record.uri?eid=2-s2.0-0027072659&partnerID=40&md5=adbcf02fd6037dab49306af18cae67f6. cited By 41.

[2] M. H. Aliabadi and D. P. Rooke. *Numerical Fracture Mechanics*, volume 8. Kluwer Academic Publishers, 1991. ISBN 1-85312-057-X.

[3] VA Baikov, AY Davletbaev, TS Usmanov, AR Asmandiyarov, and Z Stepanova. Special well-tests to fractured water injection wells. *Neftegazovoe Delo*, (1):65–75, 2011.

[4] VA Baikov, RM Zhdanov, TI Mullagaliev, and TS Usmanov. Selecting the optimal system design for the fields with low-permeability reservoirs. *Electronic scientific journal Oil and Gas Business*, 1:84–98, 2011.

[5] G.I. Barenblatt. The mathematical theory of equilibrium cracks in brittle fracture. *Advances in Applied Mechanics*, 7(C):55–129, 1962. doi: 10.1016/S0065-2156(08)70121-2. URL https://www.scopus.com/inward/record.uri?eid=2-s2.0-77649193465&doi=10.1016%2fS0065-2156%2808%2970121-2&partnerID=40&md5=212a71b2cbbd51a725e284fc0cb67aee. cited By 2410.

[6] David Thomas Barr. *Thermal cracking in nonporous geothermal reservoirs*. PhD thesis, Massachusetts Institute of Technology, 1980.

[7] R.S. Barsoum. On the use of isoparametric finite elements in linear fracture mechanics. *International Journal for Numerical Methods in Engineering*, 10(1):25–37, 1976. doi: 10.1002/nme.1620100103. URL https://www.scopus.com/inward/record.uri?eid=2-s2.0-0016892878&doi=10.1002%2fnme.1620100103&partnerID=40&md5=faf24cb9a1b029cdcb3d47071bde5723. cited By 1004.

[8] C. Barton, D. Moos, and K. Tezuka. Geomechanical wellbore imaging: Implications for reservoir fracture permeability. *AAPG Bulletin*, 93(11):1551–1569, 2009. doi: 10.1306/06180909030. URL https://www.scopus.com/inward/record.uri?eid=2-s2.0-73449089443&doi=10.1306%2f06180909030&partnerID=40&md5=43322539895fbc6d59efe3bde39ebe88. cited By 16.

[9] Zdenvek P Bavzant, Hideomi Ohtsubo, and Kazuo Aoh. Stability and post-critical growth of a system of cooling or shrinkage cracks. *International Journal of Fracture*, 15(5):443–456, 1979.

[10] S.E. Benzley. Representation of singularities with isoparametric finite elements. *International Journal for Numerical Methods in Engineering*, 8(3):537–545, 1974. doi: 10.1002/nme.1620080310. URL https://www.scopus.com/inward/record.uri?eid=2-s2.0-0015985921&doi=10.1002%2fnme.1620080310&partnerID=40&md5=c3cc05f67d226c89d29b0ac7f0689b8e. cited By 205.

[11] M.A. Biot. Mechanics of deformation and acoustic propagation in porous media. *Journal of Applied Physics*, 33(4):1482–1498, 1962. doi: 10.1063/1.1728759. URL https://www.scopus.com/inward/record.uri?eid=2-s2.0-36849137954&doi=10.1063%2f1.1728759&partnerID=40&md5=c2922faf9e43f3ceefab5c3a8fc5eac8. cited By 2124.

[12] Thomas L Blanton et al. An experimental study of interaction between hydraulically induced and pre-existing fractures. In *SPE unconventional gas recovery symposium*. Society of Petroleum Engineers, 1982.

[13] R.I. Borja. *Plasticity: Modeling & Computation*. SpringerLink : Bücher. Springer Berlin Heidelberg, 2013. ISBN 9783642385476. URL https://books.google.nl/books?id=sWBEAAAAQBAJ.

[14] Donald W Brown, David V Duchane, Grant Heiken, and Vivi Thomas Hriscu. *Mining the earth's heat: hot dry rock geothermal energy*. Springer Science & Business Media, 2012.

[15] P. C. Carman. *Flow of Gases Through Porous Media*. Academic Press Inc, New York City, 1956.

[16] Simone Cesca, Francesco Grigoli, Sebastian Heimann, Alvaro González, Elisa Buforn, Samira Maghsoudi, Estefania Blanch, and Torsten Dahm. The 2013 september–october seismic sequence offshore spain: a case of seismicity triggered by gas injection? *Geophysical Journal International*, 198(2):941–953, 2014.

[17] S.K. Chan, I.S. Tuba, and W.K. Wilson. On the finite element method in linear fracture mechanics. *Engineering Fracture Mechanics*, 2(1):1–17, 1970. doi: 10.1016/0013-7944(70)90026-3. URL https://www.scopus.com/inward/record.uri?eid=2-s2.0-0014809580&doi=10.1016%2f0013-7944%2870%2990026-3&partnerID=40&md5=575efa7e34a93526122e28313f2d918d. cited By 377.

[18] G.P. Cherepanov. Crack propagation in continuous media. pmm vol. 31, no. 3, 1967, pp. 476-488. *Journal of Applied Mathematics and Mechanics*, 31(3):503–512, 1967. URL https://www.scopus.com/inward/record.uri?eid=2-s2.0-49949147914&partnerID=40&md5=6a9ff899c1f29e9c89f1b55bde2091f5. cited By 176.

[19] O. Coussy. *Poromechanics*. John Wiley & Sons, Ltd, John Wiley & Sons Ltd, The Atrium, Southern Gate, Chichester, West Sussex PO19 8SQ, England, 1 edition, 2004. ISBN 0-470-84920-7.

[20] Steven L Crouch, Antony M Starfield, and FJ Rizzo. Boundary element methods in solid mechanics. *Journal of Applied Mechanics*, 50:704, 1983.

[21] Abbas Ali Daneshy. Study of inclined hydraulic fractures. *Soc Pet Eng J*, 13(2):61–68, 1973. URL https://www.scopus.com/inward/record.uri?eid=2-s2.0-0015614134&partnerID=40&md5=16c51bd9da5c56b0578040baa01ec8c1. cited By 62.

[22] C. David, T.-F. Wong, W. Zhu, and J. Zhang. Laboratory measurement of compaction-induced permeability change in porous rocks: Implications for the generation and maintenance of pore pressure excess in the crust. *Pure and Applied Geophysics PAGEOPH*, 143(1-3):425–456, 1994. doi: 10.1007/BF00874337. URL https://www.scopus.com/inward/record.uri?eid=2-s2.0-19044399706&doi=10.1007%2fBF00874337&partnerID=40&md5=aed4b2255e7d7daee242e06d37930a8f. cited By 251.

[23] C.J. De Pater, J. Desroches, J. Groenenboom, and L. Weijers. Physical and numerical modeling of hydraulic fracture closure. *SPE Production and Facilities*, 11(2):122–128, 1996. URL https://www.scopus.com/inward/record.uri?eid=2-s2.0-0030150254&partnerID=40&md5=3494e5fb5dc3d55ecb0b99a3af40a12c. cited By 12.

[24] BJ Dikken, H Niko, et al. Waterflood-induced fractures: a simulation study of their propagation and effects on waterflood sweep efficiency. In *Offshore Europe*. Society of Petroleum Engineers, 1987.

[25] J. Dolbow and T. Belytschko. A finite element method for crack growth without remeshing. *International journal for numerical methods in engineering*, 46(1):131–150, 1999.

[26] John Dolbow, Nicolas Moës, and Ted Belytschko. An extended finite element method for modeling crack growth with frictional contact. *Computer methods in applied Mechanics and engineering*, 190(51):6825–6846, 2001.

[27] D.S. Dugdale. Yielding of steel sheets containing slits. *Journal of the Mechanics and Physics of Solids*, 8(2):100–104, 1960. URL https://www.scopus.com/inward/record.uri?eid=2-s2.0-50549180512&partnerID=40&md5=e3b18580f16888f058a1d7e0df813a7d. cited By 4086.

[28] J. M. C. Duhamel. *Memoir on the genral method related to heat transfer in solid bodies immersed in a medium whose termperature varies with time.* J. Ecole Polytech., Paris, 1833.

[29] Birgitte Eikemo, Knut-Andreas Lie, Geir Terje Eigestad, and Helge K Dahle. Discontinuous galerkin methods for advective transport in single-continuum models of fractured media. *Advances in water resources*, 32(4):493–506, 2009.

[30] W. El Rabaa. Experimental study of hydraulic fracture geometry initiated from horizontal wells. *SPE Reprint Series*, (47):166–173, 1998. URL https://www.scopus.com/inward/record.uri?eid=2-s2.0-0031697502&partnerID=40&md5=7dc02ffb5df325a7ba99a5a1ad0f7faa. cited By 2.

[31] F. Erdogan and G. C. Sih. On the crack extension in plates under plane loading and transverse shear. *Journal of Basic Engineering*, pages 519–525, 1963.

[32] TT Garipov, DV Voskov, HA Tchelepi, et al. Rigorous coupling of geomechanics and thermal-compositional flow for sagd and es-sagd operations. In *SPE Canada Heavy Oil Technical Conference*. Society of Petroleum Engineers, 2015.

[33] T.T. Garipov, M. Karimi-Fard, and H.A. Tchelepi. Discrete fracture model for coupled flow and geomechanics. *Computational Geosciences*, 20(1):149–160, 2016. doi: 10.1007/s10596-015-9554-z. URL https://www.scopus.com/inward/record.uri?eid=2-s2.0-84962283316&doi=10.1007%2fs10596-015-9554-z&partnerID=40&md5=b108e35af82b7dcdf6607a9c5d9a612c. cited By 12.

[34] TT Garipov, JA White, A Lapene, HA Tchelepi, et al. Thermo-hydro-mechanical model for source rock thermal maturation. In *50th US Rock Mechanics/Geomechanics Symposium*. American Rock Mechanics Association, 2016.

[35] J. Garzon, P. O'Hara, C.A. Duarte, and W.G. Buttlar. Improvements of explicit crack surface representation and update within the generalized finite element method with application to three-dimensional crack coalescence. *International Journal for Numerical Methods in Engineering*, 97(4):231–273, 2014. doi: 10.1002/nme.4573. URL

https://www.scopus.com/inward/record.uri?eid=2-s2.0-84890859180&doi=10.1002%2fnme.4573&partnerID=40&md5=c705ab56b194df6e1e73f34f5355b0d5. cited By 9.

[36] J Geertsma, F De Klerk, et al. A rapid method of predicting width and extent of hydraulically induced fractures. *Journal of Petroleum Technology*, 21(12):1–571, 1969.

[37] C. Geuzaine and J.-F. Remacle. Gmsh: A 3-d finite element mesh generator with built-in pre- and post-processing facilities. *International Journal for Numerical Methods in Engineering*, 79(11):1309–1331, 2009. doi: 10.1002/nme.2579. URL https://www.scopus.com/inward/record.uri?eid=2-s2.0-67650149648&doi=10.1002%2fnme.2579&partnerID=40&md5=29572f02f8cfee8b87a37e2fd2af844a. cited By 1350.

[38] S Granet, P Fabrie, P Lemonnier, and Michel Quintard. A two-phase flow simulation of a fractured reservoir using a new fissure element method. *Journal of Petroleum Science and Engineering*, 32(1):35–52, 2001.

[39] A. A. Griffith. The phenomena of rupture and flow in solids. *Philosophical Transactions of the Royal Society of London A: Mathematical, Physical and Engineering Sciences*, 221(582-593):163–198, 1921. ISSN 0264-3952. doi: 10.1098/rsta.1921.0006.

[40] G.V. Guinea, J. Planas, and M. Elices. Ki evaluation by the displacement extrapolation technique. *Engineering Fracture Mechanics*, 66(3):243–255, 2000. URL https://www.scopus.com/inward/record.uri?eid=2-s2.0-0000575148&partnerID=40&md5=d53e7483efa0cd14a9179baa596eaa74. cited By 67.

[41] J. Hagoort. *Waterflood-induced hydraulic fracturing*. PhD thesis, Delft Technical University, Delft, The Netherlands, 7 1981. URL http://resolver.tudelft.nl/uuid:93b1fede-e03e-48d7-99c9-1c709d69397c.

[42] S.D. Hallam and N.C. Last. Geometry of hydraulic fractures from modestly deviated wellbores. *JPT, Journal of Petroleum Technology*, 43(6):742–748, 1991. URL https://www.scopus.com/inward/record.uri?eid=2-s2.0-0026169744&partnerID=40&md5=b97c29db01b27eda09e0670177497add. cited By 29.

[43] Anita Hansbo and Peter Hansbo. An unfitted finite element method, based on nitsche's method, for elliptic interface problems. *Computer methods in applied mechanics and engineering*, 191(47):5537–5552, 2002.

[44] Markus O Häring, Ulrich Schanz, Florentin Ladner, and Ben C Dyer. Characterisation of the basel 1 enhanced geothermal system. *Geothermics*, 37(5):469–495, 2008.

[45] R.D. Henshell and K.G. Shaw. Crack tip finite elements are unnecessary. *International Journal for Numerical Methods in Engineering*, 9(3):495–507, 1975. doi: 10.1002/nme.1620090302. URL https://www.scopus.com/inward/record.uri?eid=2-s2.0-0016459125&doi=10.1002%2fnme.1620090302&partnerID=40&md5=2f5c4f2d82191c852687c801bf29d615. cited By 699.

[46] Hussein Hoteit and Abbas Firoozabadi. Multicomponent fluid flow by discontinuous galerkin and mixed methods in unfractured and fractured media. *Water Resources Research*, 41(11), 2005.

[47] Hussein Hoteit and Abbas Firoozabadi. An efficient numerical model for incompressible two-phase flow in fractured media. *Advances in Water Resources*, 31(6):891–905, 2008.

[48] Thomas JR Hughes. *The finite element method: linear static and dynamic finite element analysis*. Courier Corporation, 2012.

[49] B. Hustedt, Y. Qiu, D. Zwarts, and P.J. Van Den Hoek. Modeling water-injection-induced fractures in reservoir simulation. pages 1323–1331, 2005. URL https://www.scopus.com/inward/record.uri?eid=2-s2.0-33644796081&partnerID=40&md5=c8fcb4d6d7fb038e6861cd84afd2e66d. cited By 8.

[50] G. R. Irwin. Analysis of Stresses and Strains Near the End of a Crack Traversing a Plate. *J. Appl. Mech.*, 1957.

[51] J. C. Jaeger, N. G. W. Cook, and R. W. Zimmerman. *Fundamentals of Rock Mechanics*. Blackwell Publishing, Ltd, 350 Main Street, Malden, MA 02148-5020, USA, 4 edition, 2007. ISBN 978-0-632-05759-7.

[52] Charles R Jenkins, Peter J Cook, Jonathan Ennis-King, James Undershultz, Chris Boreham, Tess Dance, Patrice de Caritat, David M Etheridge, Barry M Freifeld, Allison Hortle, et al. Safe storage and effective monitoring of co2 in depleted gas fields. *Proceedings of the National Academy of Sciences*, 109(2):E35–E41, 2012.

[53] Ruben Juanes, Javier Samper, and Jorge Molinero. A general and efficient formulation of fractures and boundary conditions in the finite element method. *International Journal for Numerical Methods in Engineering*, 54(12):1751–1774, 2002.

[54] L.M. Kachanov. *Introduction to Continuum Damage Mechanics*. Marinive Nijhoff, 1986.

[55] M Karimi-Fard and A Firoozabadi. Numerical simulation of water injection in fractured media using the discrete fractured model and the galerkin method. speree 6 (2): 117–126. Technical report, SPE-83633-PA. DOI: 10.2118/83633-PA, 2003.

[56] M. Karimi-Fard, L.J. Durlofsky, and K. Aziz. An efficient discrete-fracture model applicable for general-purpose reservoir simulators. *SPE Journal*, 9(2):227–236, 2004. URL https://www.scopus.com/inward/record.uri?eid=2-s2.0-4344671105&partnerID=40&md5=77a4db2607df711f219442d1dea2d111. cited By 235.

[57] Mohammad Karimi-Fard, Luis J Durlofsky, K Aziz, et al. An efficient discrete fracture model applicable for general purpose reservoir simulators. In *SPE Reservoir Simulation Symposium*. Society of Petroleum Engineers, 2003.

[58] Katie M Keranen, Matthew Weingarten, Geoffrey A Abers, Barbara A Bekins, and Shemin Ge. Sharp increase in central oklahoma seismicity since 2008 induced by massive wastewater injection. *Science*, 345(6195):448–451, 2014.

[59] S Khristianovic and Y Zheltov. Formation of vertical fractures by means of highly viscous fluids. In *Proc. 4th world petroleum congress, Rome*, volume 2, pages 579–586, 1955.

[60] Jong-Gyun Kim and Milind D Deo. Finite element, discrete-fracture model for multiphase flow in porous media. *AIChE Journal*, 46(6):1120–1130, 2000.

[61] George Everette King et al. Hydraulic fracturing 101: what every representative, environmentalist, regulator, reporter, investor, university researcher, neighbor and engineer should know about estimating frac risk and improving frac performance in unconventional gas and oil wells. 2012.

[62] V.V. Kokurina. Influence of unstable fractures of injection well breaks on hydrodynamical investigation in wells (in russian). *Sci-Tech Bulletin Karotazhnik (Well Logger)*, (1):83–99, 2010.

[63] E. Koning. *Waterflooding under fracturing conditions*. PhD thesis, Delft Technical University, Delft, The Netherlands, 9 1988. URL http://resolver.tudelft.nl/uuid:c0bd1703-8cc5-46e0-a724-142a879298bd.

[64] Mikael Izrael Kremenetskiy, Andrey Ivanovich Ipatov, Valentina Kokurina, et al. Well-test interpretation in case of behind-the-casing crossflow. 2008.

[65] SI Kudryashov, SI Bachin, IS Afanasyev, AR Latypov, AV Sveshnikov, TS Usmanov, AG Pasynkov, and AN Nikitin. Hydrofracturing as a way of low-permeable reservoirs development. *Oil industry*, (7):80–83, 2006.

[66] S.A. Laham. *Stress Intensity Factor and Limit Load Handbook*. EPD/GEN/REP. British Energy Generation Limited, 1998. URL https://books.google.nl/books?id=dhegPgAACAAJ.

[67] Larry W Lake. Enhanced oil recovery. 1989.

[68] Fushen Liu and Ronaldo I Borja. Stabilized low-order finite elements for frictional contact with the extended finite element method. *Computer Methods in Applied Mechanics and Engineering*, 199(37):2456–2471, 2010.

[69] Vincent Martin, Jérôme Jaffré, and Jean E Roberts. Modeling fractures and barriers as interfaces for flow in porous media. *SIAM Journal on Scientific Computing*, 26(5):1667–1691, 2005.

[70] Shawn C Maxwell, Charles Waltman, Norman R Warpinski, Michael J Mayerhofer, Neda Boroumand, et al. Imaging seismic deformation induced by hydraulic fracture complexity. *SPE Reservoir Evaluation & Engineering*, 12(01):48–52, 2009.

[71] C Miehe, F Welschinger, and M Hofacker. Thermodynamically consistent phase-field models of fracture: Variational principles and multi-field fe implementations. *International Journal for Numerical Methods in Engineering*, 83(10):1273–1311, 2010.

[72] Christian Miehe, Martina Hofacker, and Fabian Welschinger. A phase field model for rate-independent crack propagation: Robust algorithmic implementation based on operator splits. *Computer Methods in Applied Mechanics and Engineering*, 199(45):2765–2778, 2010.

[73] Inga Moeck, Grzegorz Kwiatek, and Günter Zimmermann. Slip tendency analysis, fault reactivation potential and induced seismicity in a deep geothermal reservoir. *Journal of Structural Geology*, 31(10):1174–1182, 2009.

[74] Nicolas Moës, Claude Stolz, P-E Bernard, and Nicolas Chevaugeon. A level set based model for damage growth: the thick level set approach. *International Journal for Numerical Methods in Engineering*, 86(3):358–380, 2011.

[75] JEP Monteagudo and Abbas Firoozabadi. Control-volume method for numerical simulation of two-phase immiscible flow in two-and three-dimensional discrete-fractured media. *Water resources research*, 40(7), 2004.

[76] M. Muskat. *The flow of homogeneous fluids through porous media*. J. W. Edwards, Inc, Ann Arbor, Michigan, USA, 1 edition, 1946.

[77] J. Noorishad, C.F. Tsang, and P.A. Witherspoon. Coupled thermal-hydraulic-mechanical phenomena in saturated fractured porous rocks: Numerical approach. *Journal of Geophysical Research*, 89(B12):10365–10373, 1984. URL https://www.scopus.com/inward/record.uri?eid=2-s2.0-0021521632&partnerID=40&md5=68552e6b4ee498eace533428e0727e55. cited By 92.

[78] Jan Martin Nordbotten. Finite volume hydromechanical simulation in porous media. *Water resources research*, 50(5):4379–4394, 2014.

[79] RP Nordgren et al. Propagation of a vertical hydraulic fracture. *Society of Petroleum Engineers Journal*, 12(04):306–314, 1972.

[80] A Obermann, T Kraft, E Larose, and S Wiemer. Potential of ambient seismic noise techniques to monitor the st. gallen geothermal site (switzerland). *Journal of Geophysical Research: Solid Earth*, 120(6):4301–4316, 2015.

[81] E. Orowan. *Notch Brittleness and the Strength of Metals*. Institution of Engineers and Shipbuilders in Scotland, 1945. URL https://books.google.nl/books?id=o-sEHAAACAAJ.

[82] Chris Pearson. The relationship between microseismicity and high pore pressures during hydraulic stimulation experiments in low permeability granitic rocks. *Journal of Geophysical Research: Solid Earth*, 86(B9):7855–7864, 1981.

[83] T.K. Perkins and J.A. Gonzalez. Effect of thermoelastic stresses on injection well fracturing. *Society of Petroleum Engineers journal*, 25(1):78–88, 1985. URL https://www.scopus.com/inward/record.uri?eid=2-s2.0-0022011127&partnerID=40&md5=8844bef940e9226055fabc056ee68899. cited By 94.

[84] TK Perkins, LR Kern, et al. Widths of hydraulic fractures. *Journal of Petroleum Technology*, 13(09):937–949, 1961.

[85] G. Pluvinage. *Mécanique élastoplastique de la rupture : Critères d'amorçage*. Cepadues-Editions, 111, rue Nicolas-Vauquelin - 31100 Toulouse, France, 1989. ISBN 978-2854282207.

[86] G. Pluvinage. *Elastoplastic Mechanics of Failure. Translation from French by V. T. Sapunova. In Russian*. Izdatel'stvo Mir, Moscow, 1993. ISBN 5-03-002508-1.

[87] Michael A Puso and Tod A Laursen. A mortar segment-to-segment frictional contact method for large deformations. *Computer methods in applied mechanics and engineering*, 193(45):4891–4913, 2004.

[88] J. R. Rice. A path independent integral and the approximate analysis of strain concentration by notches and cracks. *Journal of Applied Mechanics*, pages 379–386, 1968.

[89] D.P. Rooke, D.J. Cartwright, and Great Britain. Ministry of Defence. Procurement Executive. *Compendium of Stress Intensity Factors*. Stationery Office, 1976. ISBN 9780117713369. URL https://books.google.nl/books?id=Jy4IAQAAIAAJ.

[90] Antonin Settari, Michael P Cleary, et al. Development and testing of a pseudo-three-dimensional model of hydraulic fracture geometry. *SPE Production Engineering*, 1(06):449–466, 1986.

[91] R.R. Settgast, P. Fu, S.D.C. Walsh, J.A. White, C. Annavarapu, and F.J. Ryerson. A fully coupled method for massively parallel simulation of hydraulically driven fractures in 3-dimensions. *International Journal for Numerical and Analytical Methods in Geomechanics*, 41(5):627–653, 2017. doi: 10.1002/nag.2557. URL https://www.scopus.com/inward/record.uri?eid=2-s2.0-84988377949&doi=10.1002%2fnag.2557&partnerID=40&md5=eedcfad36f09b91da9549ae6c4b5f321. cited By 0.

[92] C.F. Shih, H.G. de Lorenzi, and M.D. German. Crack extension modeling with singular quadratic isoparametric elements. *International Journal of Fracture*, 12(4):647–651, 1976. doi: 10.1007/BF00034654. URL https://www.scopus.com/inward/record.uri?eid=2-s2.0-0000254972&doi=10.1007%2fBF00034654&partnerID=40&md5=78aee0473588e05183af377df9a36d73. cited By 185.

[93] G.C. Sih. Strain-energy-density factor applied to mixed mode crack problems. *International Journal of Fracture*, 10(3):305–321, 1974. doi: 10.1007/BF00035493. URL https://www.scopus.com/inward/record.uri?eid=2-s2.0-0016101548&doi=10.1007%2fBF00035493&partnerID=40&md5=0b794d4e4259865bce380cbdf7c64472. cited By 1305.

[94] J Ci Simo and TA Laursen. An augmented lagrangian treatment of contact problems involving friction. *Computers & Structures*, 42(1):97–116, 1992.

[95] J.C. Simo and T.A. Laursen. An augmented lagrangian treatment of contact problems involving friction. *Computers and Structures*, 42(1):97–116, 1992. doi: 10.1016/0045-7949(92)90540-G. URL https://www.scopus.com/inward/record.uri?eid=2-s2.0-0026626125&doi=10.1016%2f0045-7949%2892%2990540-G&partnerID=40&md5=bcd78fc77b6d53a759c08c1466bc1434. cited By 522.

[96] Juan C Simo, Peter Wriggers, and Robert L Taylor. A perturbed lagrangian formulation for the finite element solution of contact problems. *Computer methods in applied mechanics and engineering*, 50(2):163–180, 1985.

[97] Jefferson W Tester, Brian J Anderson, Anthony S Batchelor, David D Blackwell, Ronald DiPippo, E Drake, John Garnish, B Livesay, Michal C Moore, Kenneth Nichols, et al. The future of geothermal energy: Impact of enhanced geothermal systems (egs) on the united states in the 21st century. *Massachusetts Institute of Technology*, 209, 2006.

[98] M. Trimonova, N. Dubinya, et al. The main tendencies of water-induced hydraulic fracture propagation. In *SPE Russian Petroleum Technology Conference*. Society of Petroleum Engineers, 2015.

[99] TS Usmanov, IZ Mullagalin, IS Afanas' ev, RK Mukhametshin, IF Khatmullin, KV Ababkov, and AG Pasynkov. Analiz vliyaniya grp na nefteotdachu plastov na mestorozhdeniyakh oao "yuganskneftegaz"(analysis of the influence of hydraulic fracturing for oil recovery in the fields of "yuganskneftegaz" jsc). *Tekhnologii TEK*, (5):24, 2005.

[100] D.B. Van Dam, C.J. De Pater, and R. Romijn. Analysis of hydraulic fracture closure in laboratory experiments. *SPE Production and Facilities*, 15(3):151–158, 2000. URL https://www.scopus.com/inward/record.uri?eid=2-s2.0-0034238065&partnerID=40&md5=19b272641ba6b1663253349be70f85d0. cited By 11.

[101] PJ van de Hoek, G Sommerauer, L Nnabuihe, D Munro, et al. Large-scale produced water re-injection under fracturing conditions in oman. In *Abu Dhabi International Petroleum Exhibition and Conference*. Society of Petroleum Engineers, 2000.

[102] Paul J van den Hoek et al. Dimensions and degree of containment of waterflood-induced fractures from pressure transient analysis. *SPE Reservoir Evaluation & Engineering*, 8(05): 377–387, 2005.

[103] P.J. Van den Hoek. A simple and accurate description of nonlinear fluid leakoff, in high-permeability fracturing. *SPE Journal*, 7(1):14–23, 2002. URL https://www.scopus.com/inward/record.uri?eid=2-s2.0-0036494595&partnerID=40&md5=99e4d7ff589c9fd051f185f7f91111ee. cited By 15.

[104] P.J. Van Den Hoek. Methodology to compute mathieu functions for arbitrary large parameter q and its application to pressure transient analysis. 2016. URL https://www.scopus.com/inward/record.uri?eid=2-s2.0-84994498907&partnerID=40&md5=55293313b973307a565d4eaf6d884cd9. cited By 0.

[105] P.J. Van Den Hoek, T. Matsuura, M. De Kroon, and G. Gheissary. Simulation of produced water reinjection under fracturing conditions. *SPE Production and Facilities*, 14 (3):166–176, 1999. URL https://www.scopus.com/inward/record.uri?eid=2-s2.0-0032880161&partnerID=40&md5=cc6ca70769893ab8395dda6586bcafd3. cited By 23.

[106] James P Verdon, J-Michael Kendall, Anna L Stork, R Andy Chadwick, Don J White, and Rob C Bissell. Comparison of geomechanical deformation induced by megatonne-scale co2 storage at sleipner, weyburn, and in salah. *Proceedings of the National Academy of Sciences*, 110(30):E2762–E2771, 2013.

[107] Denis Voskov. An extended natural variable formulation for compositional simulation based on tie-line parameterization. *Transport in porous media*, 92(3):541–557, 2012.

[108] Denis V Voskov and Hamdi A Tchelepi. Comparison of nonlinear formulations for two-phase multi-component eos based simulation. *Journal of Petroleum Science and Engineering*, 82:101–111, 2012.

[109] Denis Viktorovich Voskov, Hamdi A Tchelepi, Rami Younis, et al. General nonlinear solution strategies for multiphase multicomponent eos based simulation. In *SPE Reservoir Simulation Symposium*. Society of Petroleum Engineers, 2009.

[110] Nathaniel R Warner, Cidney A Christie, Robert B Jackson, and Avner Vengosh. Impacts of shale gas wastewater disposal on water quality in western pennsylvania. *Environmental science & technology*, 47(20):11849–11857, 2013.

[111] Norman Raymond Warpinski, Michael J Mayerhofer, Michael C Vincent, Craig L Cipolla, EP Lolon, et al. Stimulating unconventional reservoirs: maximizing network growth while optimizing fracture conductivity. *Journal of Canadian Petroleum Technology*, 48(10):39–51, 2009.

[112] NR Warpinski, PT Branagan, RE Peterson, JE Fix, JE Uhl, BP Engler, R Wilmer, et al. Microseismic and deformation imaging of hydraulic fracture growth and geometry in the c sand interval, gri/doe m-site project. In *SPE Annual Technical Conference and Exhibition*. Society of Petroleum Engineers, 1997.

[113] A. A. Wells. Application of fracture mechanics at and beyond general yielding. *British Welding Journal*, pages 563–570, 1963.

[114] GN Wells and LJ Sluys. A new method for modelling cohesive cracks using finite elements. *International Journal for Numerical Methods in Engineering*, 50(12):2667–2682, 2001.

[115] P. Wriggers and G. Zavarise. *Computational Contact Mechanics*. John Wiley and Sons, Ltd, 2004. ISBN 9780470091357. doi: 10.1002/0470091355.ecm033. URL http://dx.doi.org/10.1002/0470091355.ecm033.

[116] Rustem Zaydullin, Denis Voskov, Hamdi A Tchelepi, et al. Nonlinear formulation based on an equation-of-state free method for compositional flow simulation. *SPE Journal*, 18(02): 264–273, 2012.

[117] Rustem Zaydullin, Denis V Voskov, Scott C James, Heath Henley, and Angelo Lucia. Fully compositional and thermal reservoir simulation. *Computers & Chemical Engineering*, 63: 51–65, 2014.

[118] Junjing Zhang, Anton Kamenov, D Zhu, and AD Hill. Laboratory measurement of hydraulic fracture conductivities in the barnett shale. In *IPTC 2013: International Petroleum Technology Conference*, 2013.

[119] Yipeng Zhang, Mark Person, John Rupp, Kevin Ellett, Michael A Celia, Carl W Gable, Brenda Bowen, James Evans, Karl Bandilla, Peter Mozley, et al. Hydrogeologic controls on induced seismicity in crystalline basement rocks due to fluid injection into basal reservoirs. *Groundwater*, 51(4):525–538, 2013.

[120] Yifan Zhou, Hamdi A Tchelepi, Bradley T Mallison, et al. Automatic differentiation framework for compositional simulation on unstructured grids with multi-point discretization schemes. In *SPE Reservoir Simulation Symposium*. Society of Petroleum Engineers, 2011.

[121] Olek C Zienkiewicz and Robert L Taylor. *The finite element method for solid and structural mechanics*. Butterworth-heinemann, 2005.

[122] Mark D Zoback and Steven M Gorelick. Earthquake triggering and large-scale geologic storage of carbon dioxide. *Proceedings of the National Academy of Sciences*, 109(26): 10164–10168, 2012.